

# Multi-Pass Commissioning of CBETA and Inverse Compton Scattering Sources as an Alternative to the UKFEL Project

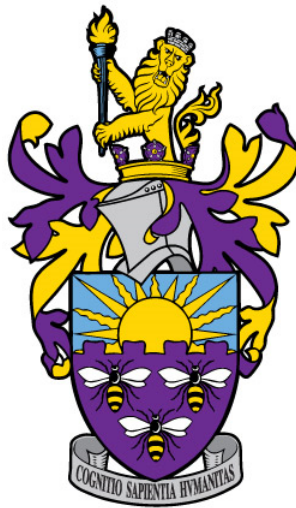
Joe Crone

1st Year PhD Report

Supervised by Dr H. Owen & Dr B. Muratori

The Cockcroft Institute & University of Manchester, Faculty of Science & Engineering

August 16, 2019



## Abstract

This report examines where the energy recovery linac project CBETA lies in the present state of the field. The application of inverse Compton scattering sources (ICS) to ERL's is evaluated with respect to other forms of accelerator. The regimes of inverse Compton scattering and calculations of spectral output parameters, such as the bandwidth, are explained. The beam dynamics of CBETA are scrutinised through a series of investigations, these are particularly focused on the splitter/recombiner path length correction systems and the FFAG recirculation line through use of the beam dynamics code Bmad. An inverse Compton scattering source is designed for CBETA to produce narrow-band X-rays in the range of 33 - 427 keV. This includes the design and simulation of a bypass, where the ICS is situated, to be incorporated into the CBETA ERL within the ZA/ZB FFAG straight section. A  $\gamma$ -ray ICS design is proposed on DIANA, a proposed ERL for nuclear physics applications. Additionally, there is a breakdown of the future work to be carried out in this PhD project including details of the CBETA commissioning work to be undertaken and the further ICS studies such as those on storage rings. Finally a Gantt chart is provided to give a rough time-scale of the future work as well as a series of thesis chapter titles to outline the project.

# 1 Introduction

The remit of this work is to investigate an energy recovery linac (ERL) based inverse Compton scattering source (ICS) as a potential alternative to the UK free electron laser project (UKFEL). Inverse Compton scattering sources have the potential to operate as next generation light sources through providing monochromatic, narrow-band and short pulse X-rays and  $\gamma$ -rays at high brilliance and flux. Multi-pass common transport ERLs, where the trajectories at each nominal energy of the beam are confined to the same recirculation loop, potentially can supply linac quality beams at a series of discrete energies without the need for multiple, costly conventional return loops.

The project is centered around the Cornell Brookhaven National Laboratory Energy Recovery Linac Test Accelerator (CBETA), a 4-pass 150 MeV ERL with proposed average current of 40 mA [1], through use of a superconducting RF (SRF) linac, novel FFAG return loop and a splitter/recombiner path length correction system. This test accelerator has the potential to be the first demonstration of both multi-pass energy recovery and fixed field alternating gradient (FFAG) common transport in an ERL [2]. The project is a collaboration between Brookhaven National Laboratory (BNL) and Cornell University to demonstrate ERL technology, which is of interest for the proposed eRHIC [3] electron-ion collider (EIC).

This report starts by covering the theory behind CBETA: how an ERL operates and how FFAG optics can be used for common transport in an ERL. There is then a brief review of current and legacy ERL projects, which covers accelerators from the invention of the ERL to present day, this review also contains details of the first inverse Compton scattering sources (ICS) demonstrations on ERLs. A more in depth look at the CBETA project is presented with a thorough explanation of working principles of the CBETA machine. This includes topics such as the FFAG cell, the return loop, the RF system, the path length correction system and details of single and multi-pass operation.

The theory surrounding inverse Compton scattering such as the regimes of inverse Compton scattering, which impacts the output spectra from the source, and the output spectral calculations are presented and explained. A design for an X-ray ICS on CBETA is shown with simulated output spectra from CAIN, a MonteCarlo code for simulating electromagnetic interactions [4], as well as a study into incorporating the ICS into the CBETA lattice via bypassing the ZA and ZB straight sections. A design for a  $\gamma$ -ray ICS is also presented, this is for the proposed Daresbury Industrial Accelerator for Nuclear Applications (DIANA) [5]. Both the CBETA X-ray ICS and the DIANA  $\gamma$ -ray ICS are compared with similar state of the art sources, such as the cERL ICS [6] and the ELI-NP linac ICS [7]. There is then a review of current and legacy X-ray and  $\gamma$ -ray inverse Compton scattering sources based on ERLs, storage rings and linacs to show the advantages and disadvantages of each form of accelerator in terms of ICS.

Finally, there is a breakdown and description of the future work to be carried out in this PhD such as the further studies into inverse Compton scattering on storage rings, the further design work for X-ray and  $\gamma$ -ray ICS as well as details of a long term attachment at Cornell University to participate in commissioning and data analysis. A Gantt chart is provided to give a rough time-scale for the project and display the scheduling of the work. Some chapter titles are included to outline the direction and future work involved in the PhD project.

## 2 Energy Recovery Linac Theory

Energy recovery linacs and recirculating linacs (RL) are an extension of the linac concept in which the beam is recirculated from the end of the linac back to the start of the linac. Here it can be re-accelerated as in a recirculating linac or decelerated with the energy of the beam recovered through the linac as in an ERL. Whether the beam is accelerated again or is decelerated depends on the phase of the RF cavity that the beam coincides with upon re-entry into the linac. If this is in phase with the RF the beam coincides with a peak in the electric field and is accelerated again, if the beam is  $180^\circ$  out of phase the beam coincides with a trough and is decelerated. When the beam is decelerated by the RF cavity the energy of the beam is transferred to the electromagnetic field in the cavity, this energy is therefore recovered.

Figure 1 shows a schematic of the S-DALINAC ERL operating in a single pass configuration, this is used as an example to describe the operation of an ERL.

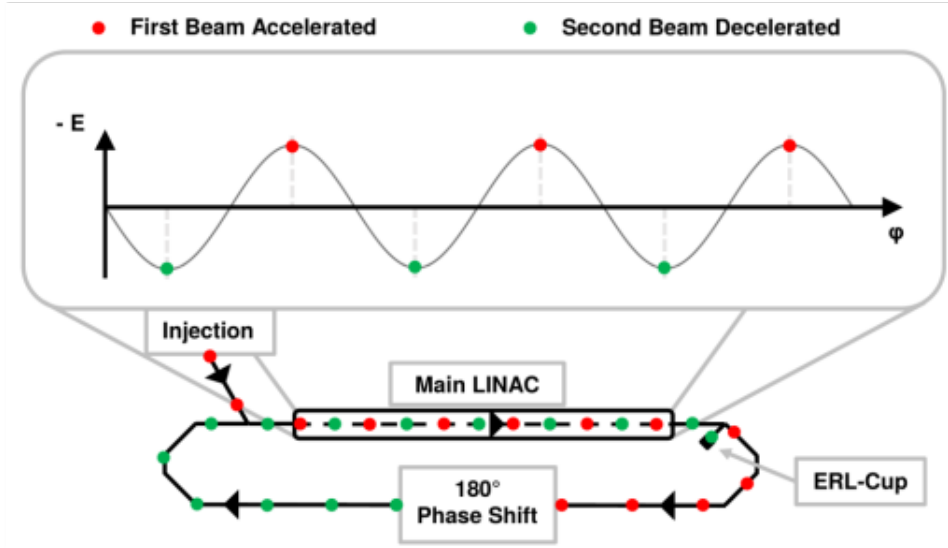


Figure 1: The S-DALINAC ERL operating in single pass energy recovery mode [8]. Top: Plot of the electric field against phase for an RF cavity in the linac. Here the red points are in phase with the electric field and therefore accelerated whilst the green points are  $180^\circ$  out of phase and are decelerated. Bottom: A diagram of the single pass ERL operation. In this part of the diagram the red points denote when the beam is in the accelerating phase and the green points decelerating phase. The  $180^\circ$  phase shift is courtesy of a path-length adjustment system which allows to change the beam's orbit by a full RF wavelength of 10 cm and thus shift the phase of the re-injected beam by up to  $360^\circ$  [8].

To elaborate upon the diagram shown in Figure 1 the beam is injected into the S-DALINAC ERL at 7.6 MeV, it then passes the main linac where it is accelerated to 38 MeV [8] as it is in phase with the RF cavity (red point). The beam is then recirculated to the path length correction system where it undergoes a phase change of  $180^\circ$  (red to green point). Therefore when the beam re-enters the linac it is in a decelerating phase (green point). The energy is recovered by the RF cavities. The beam is then decelerated back to the injector energy of 7.6 MeV and dumped.

## 2.1 Same-cell Energy Recovery

The most common form of energy recovery used in energy recovery linacs is same-cell energy recovery i.e energy recovery in which both accelerating and decelerating beams traverse the same accelerating cavity [9]. In other words, the cavity that accelerated the beam is the same cavity into which the energy is recovered.

An alternative to this is possible in a machine like the Continuous Electron Beam Accelerator Facility (CEBAF) as shown in Figure 2.

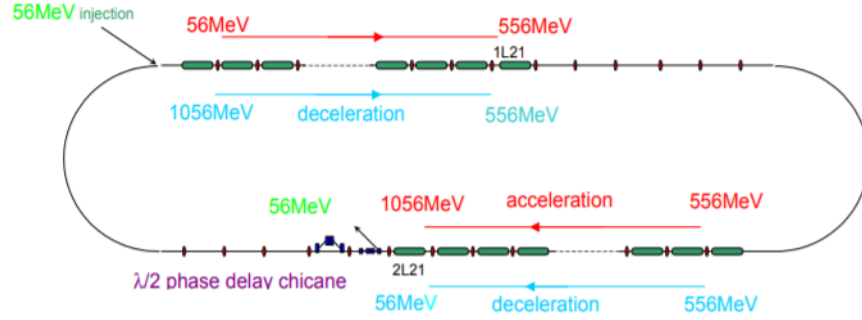


Figure 2: The CEBAF recirculating linac up as set up for the first energy recovery experiment [10]. CEBAF is a machine that uses two separate linac systems to accelerate the beam per pass, the North Linac (top) and the South linac (bottom). Since this is set up for energy recovery a  $180^\circ$  phase delay chicane has been implemented downstream of the South Linac. The phase delay chicane changes the phase of the beam from an accelerating phase to a decelerating phase.

In the single pass energy recovery operation of CEBAF beam is injected into the North Linac at 56 MeV where it is accelerated to 556 MeV [10]. The beam is then recirculated to the South Linac where it is accelerated again to a maximum energy of 1056 MeV. Downstream of the south linac the beam enters the phase delay chicane. The chicane was designed to create a path length differential of exactly one RF wavelength so that upon re-entry into the North Linac, the beam is  $180^\circ$  out of phase with the cavities and will subsequently be decelerated to 556 MeV [10]. This then passes the south linac again where the beam is decelerated to the injection energy and dumped.

In the CEBAF example as described above the 556 MeV to 1056 MeV acceleration in the south linac is recovered in the north linac. Therefore, this is not technically same-cell energy recovery. Operating in this way it could be argued that CEBAF is a multi-pass superconducting RF ERL as there are multiple linac passes in which energy is recovered. However, within this report this is not taken to be true as this report adopts the view that multi-pass energy recovery is defined as multiple instances of energy recovery by the same linac. Therefore either multiple instances of energy recovery from a single linac from differing cell, as in CEBAF, or same-cell energy recovery is permissible as multi-pass energy recovery.

## 2.2 Multi-pass ERLs and Recirculating Linacs

A multi-pass machine, such as the 3-pass S-DALINAC [11] or 4-pass CBETA ERL [1], operates in much the same way as a single pass ERL. The exception here is that after the first pass the beam is re-accelerated, as opposed to a single pass ERL where the beam is decelerated, energy recovered then dumped. This recirculation then acceleration, where the beam is returned to the linac in accelerating phase, occurs for each pass until the highest possible energy for the ERL is achieved. Then there is a  $180^\circ$  phase shift so the beam is now in decelerating phase. This beam is then recirculated in each pass again but is decelerated for each pass of the linac. After the last pass of the linac, where the beam is restored to the injection energy, the beam is dumped.

This differs from a recirculating linac as in a recirculating linac the beam is only passed through the linac in an accelerating phase. Therefore it still experiences a discrete increase in energy per linac pass however the beam is never decelerated by the linac. In this case no energy recovery can take place. This also means that the beam must be dumped at the accelerated energy as in a conventional linac. An example of a recirculating linac is the Jefferson Lab Free Electron laser (FEL), this drove a free electron laser with a 42 MeV beam [12].

## 2.3 Normal Conducting and Superconducting Energy Recovery Linacs

A typical normal conducting cavity that would be used in an ERL is one like the MAMI C normal conducting copper cavity used on the MAMI microtron [13] at Mainz, Germany. This is a 4.9 GHz RF cavity which dissipates 14 kW/m for an accelerating gradient of 1 MV/m [14] in the continuous wave mode. There is also a limitation of the current from normal conducting cavities as there is limited higher order mode (HOM) damping capabilities [15]. This is as for high current operation of ERLs there is the need to damp HOMs as these cause beam break up instabilities [16] which limits the amount of current in an ERL.

In comparison, the SRF cavity on CBETA [1] a multi-pass superconducting ERL is a 1.3 GHz L-band cavity. These cavities dissipate 27 W/m with an accelerating gradient of 16 MV/m [17]. CBETA currently has

the capability to extract 400 W of HOM power from the linac [17], much more than is possible in a normal conducting RF cavity.

Therefore, the higher accelerating gradient allows an ERL to be more compact as the linac can be made smaller for the same total acceleration. Lower power dissipation would suggest that an SRF ERL is more energy efficient, however this is almost completely negated by the efficiency of cryogenic systems. The fact that HOM damping is more readily incorporated into superconducting RF systems also makes SRF advantageous as this allows a higher beam current, which is desired in an ERL.

## 2.4 Energy Recovery Linac Benefits

The first major benefit of an ERL is that the beam is recirculated and subsequently there is the opportunity to re-accelerate the beam. This means that in order to accelerate a beam to high energy a more compact linac can be used but the beam is required to be passed through the linac multiple times before it reaches this desired energy. Discrete acceleration steps, as provided in an ERL, also has the advantage of providing a beam at a range of different energies which can be beneficial to a multi-user facility. However, this is also possible with a recirculating linac.

Another benefit of using an ERL is that the energy of the beam is recovered after acceleration in the deceleration passes. This means there is less power usage by the accelerator in comparison to a conventional linac or recirculating linac of the same beam energy. Also, by recovering energy and decelerating the beam it is dumped at an energy around the injection energy. This is useful as it removes the necessity of a high power beam dump. Avoiding dumping the electron beam at a high energy is beneficial as when the beam is dumped on the order of a few MeV this drastically reduces the number of neutrons produced, as can be seen from Figure 3.

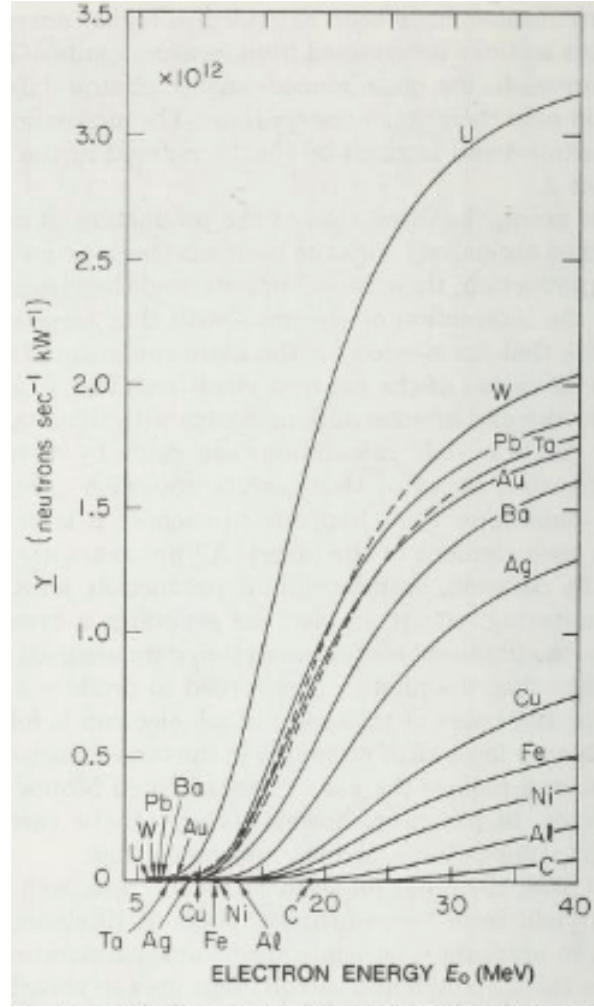


Figure 3: A plot of the neutrons produced per second per kilowatt of electron beam power against the electron energy of the beam [18]. The plot shows a this for a range of beam dump materials. Below around 10 MeV the production yield is close to zero i.e that for some materials this is below the neutron production threshold.

Beam quality is another benefit of ERLs, this is as the emittance of an ERL is dominantly governed by the emittance of the injector. The beam is circulated on the order of 10 turns maximum, this means that the beam emittance does not have time to equilibrate as in storage rings. Also the fact that the beam is used only for a few re-circulations means that some collective effects such as intra-beam scattering don't have long enough to effect the beam. Therefore, an energy recovery linac is still capable of providing a beam that is of the same quality as that from a conventional linac after a few re-circulations. However, in some cases low emittance storage rings or non-equilibrium storage rings [19] could also offer comparable beam quality with recirculation.

### 3 Fixed Field Alternating Gradient Theory

A fixed-field alternating gradient (FFAG) accelerator uses constant field magnets as in a cyclotron, whilst also using alternating gradient (AG) or 'strong' focusing as used in alternating gradient synchrotron's. Therefore FFAG optics are a distinct form of accelerator optics that offer advantages such as rapid acceleration and wide momentum acceptance, as explained in this section. The first demonstrated FFAG was the Midwestern Universities Research Association (MURA mark I) FFAG [20].

Fixed field magnets are magnets which are not pulsed like in a synchrotron where the current is ramped to produce a particular magnetic field at the required time. Instead, the magnets are set at a constant field strength which also enables the use of permanent magnets as these produce a constant magnetic field without a power supply. One particular advantage of this is that since the magnets don't require pulsing there is no ramping time for the magnet to achieve its nominal field and therefore the acceleration is only limited by the frequency modulation of the RF cavities.

Strong focusing relies upon an alternating series of focusing and defocusing lenses which leads to an overall focusing because the focusing lenses are, on average, traversed at larger distance from the axis than the defocusing ones [21]. The 'lenses' used here are quadrupoles which are focusing in one plane and defocusing in the orthogonal plane. These are described as lenses as often they can be approximated as such when using the thin lens approximation  $l_q \rightarrow 0, kl_q = \text{constant}$  in which the quadrupole effect on the beam mirrors the effect of lenses on light. One of the first examples of such an alternating gradient machine is the Proton Synchrotron at CERN, which achieved a record 28 GeV in 1960 through this method [22]. Alternating gradient focusing allowed more-compact higher energy machines to be built as by alternating between large positive and large negative field strength values at suitable azimuthal intervals, one can obtain focusing forces an order of magnitude stronger [23] than previously achieved through weak focusing. Magnets and machines could therefore be reduced in size to provide the same focusing or the accelerated beam could be increased in energy within the same footprint.

### 3.1 Radial Sector and Spiral Sector FFAGs

There are two main configurations of FFAG; the spiral sector FFAG and the radial sector FFAG. A radial sector FFAG is an FFAG in which successive bending magnets of the same field strength but opposing polarity are used in order to create alternating focusing in a series of fixed field magnets. In a radial sector FFAG bending magnets of opposing polarity are used consecutively. Alternating gradient focusing is achieved by correctly choosing the drift space between these. Whereas a spiral sector machine uses bending magnets of all of the same polarity i.e all bending in the negative or positive direction of the horizontal plane. Alternating gradient focusing is then achieved in spiral sector FFAG from edge focusing on one side of the magnet. Then if a beam does not travel through the magnet at a right angle to the face, a kick is produced [24]. A series of these kicks from the edge fields creates the strong focusing in this form of FFAG. Figure 4 shows both of these FFAG configurations diagrammatically.

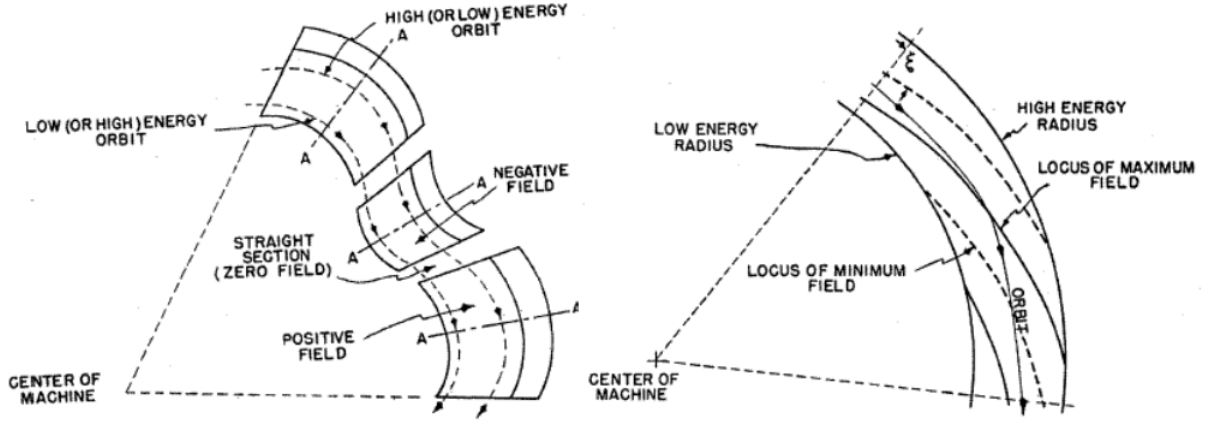


Figure 4: Left: A radial sector FFAG configuration. Right: A spiral sector FFAG configuration. [25] Here it is possible to see that the radial sector configuration uses a series of bending magnets with the same magnitude of field strength but opposing sign consecutively. This differs from the spiral sector FFAG as here the magnetic field consists of a radially increasing azimuthally independent field on which is superimposed a radially increasing azimuthally periodic field [25].

The spiral sector configuration has the advantage of space consideration over a radial sector FFAG. This is as the radial sector FFAG requires opposing polarity dipole magnets, therefore the beam is being bent in one direction then the opposite, which means that the overall path length and consequently size of the machine is much larger than in the spiral sector FFAG with constant bending direction. However, for a spiral sector FFAG there is also the disadvantage that edge fields need to be created from the magnets for the AG focusing which means that these magnets are more complex to produce. Typically combined function magnets, with both a dipole and quadrupole component, are used in the production of spiral sector FFAGs.

### 3.2 Scaling and Non-scaling FFAGs

As well as there being two configurations for the magnets used in an FFAG (spiral and radial sector) there are also two main configurations for how the orbits of the FFAGs are set up. These are the scaling and non-scaling

configurations. The difference between the two is that the beatatron tune, the number of beatatron oscillations per recirculation, is kept constant in a scaling FFAG whereas this condition is not met in a non-scaling FFAG.

In order to create a scaling FFAG two conditions must be met. The first condition is that the dipole field must be arranged in such a way that the increase in gradient with momentum results in the beam experiencing the same focusing independent of radius [26]. Mathematically this condition is

$$\left. \frac{\partial k}{\partial p} \right|_{\theta=const} = 0, \quad (1)$$

where  $p$  is the reference momentum,  $\theta$  is the bending angle and  $k$  is the field index as given by

$$k = -\frac{\rho}{B_y} \frac{\partial B_y}{\partial x}, \quad (2)$$

with  $\rho$  the bending radius,  $B_y$  the vertical magnetic field and  $\frac{\partial B_y}{\partial x}$  the vertical magnetic field gradient in the horizontal  $x$  direction. The second condition is that the shape of the particle orbit remains constant as the size of the orbit scales with energy [26]. Therefore this condition can be wrote as

$$\left. \frac{\partial}{\partial p} \left( \frac{\rho_0}{\rho} \right) \right|_{\theta=const} = 0, \quad (3)$$

where  $\rho_0$  is the reference bending radius. The effect of the two conditions (1) and (3) are shown in Figure 5.

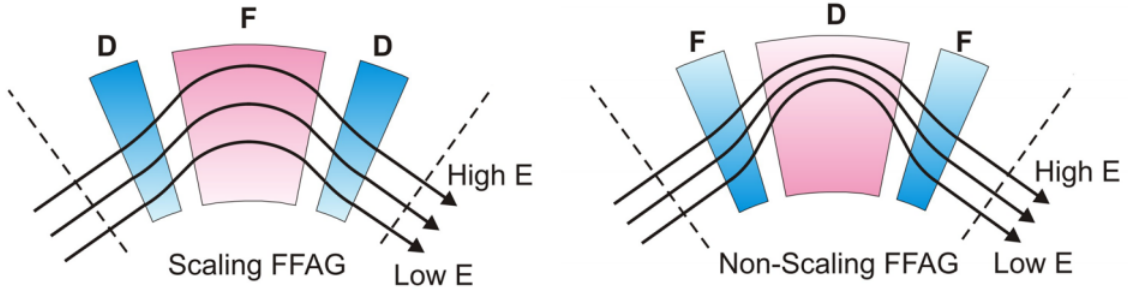


Figure 5: Left: Three trajectories of differing energy passing through a scaling FFAG as the beam passes through an FFAG cell with defocusing (D) and focusing (F) bending magnets. Right: Three differing energy trajectories passing through a non-scaling FFAG cell [27]. These diagrams show that in a scaling FFAG the bending angle of the trajectory through the dipole doesn't change with respect to the energy of the particles and also that the shape of the path is preserved at each energy.

However, since the scaling conditions are broken the non-scaling FFAG does not have constant tune  $\nu_x + \nu_y \neq const$  with  $\nu_{x,y}$  the horizontal and vertical tune. This means that it is possible that integer or sub integer ( $\nu_x + \nu_y = 1/2$ , integer +  $1/3$  etc) tune lines could be crossed and therefore resonances are possible. Figure 6 shows that not only is the tune non-constant in EMMA, it also crosses third order tunes.



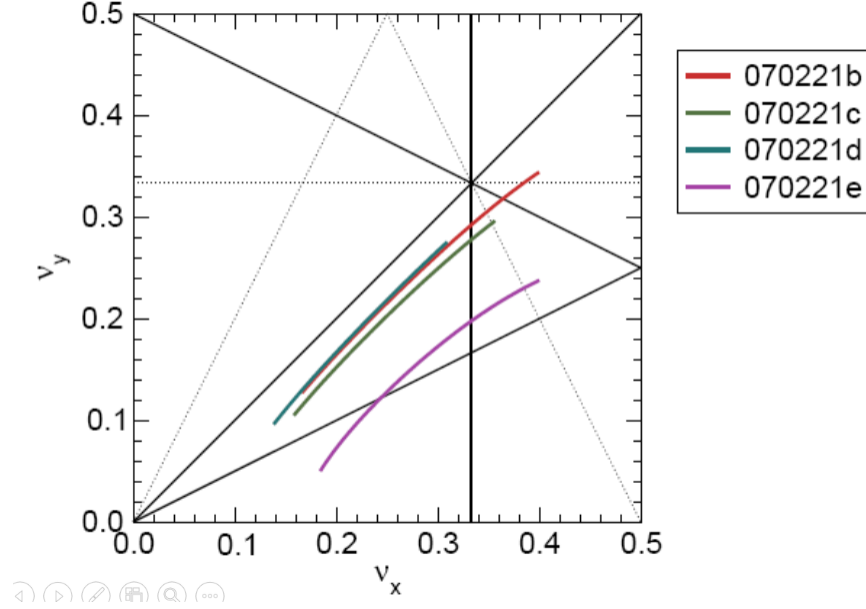


Figure 6: A tune plane diagram (horizontal tune  $\nu_x$  against vertical tune  $\nu_y$ ) for the configurations of the EMMA lattice listed in the key [28]. Here the black lines plotted are third order tune lines, the dotted lines are resonance tune lines when skew terms are taken into account.

Scaling FFAGs were demonstrated throughout the early development of the FFAG concept and have been used to build both electron and proton machines, such as the first proton FFAG synchrotron at KEK, Japan [29]. The first demonstration of a non-scaling FFAG was the Electron Machine with Many Applications (EMMA) built at Daresbury Laboratory using a single pass ERL injector named Accelerators and Lasers in Combined Experiments (ALICE) [30]. EMMA demonstrated non-scaling FFAG operation at 10.5 MeV with serpentine acceleration up to a beam energy of 20.5 MeV [31].

### 3.3 FFAGs for Common Transport

One of the most crucial benefits of the FFAG concept is the large momentum and energy acceptance that is possible with FFAG optics. This is in comparison to an ordinary synchrotron with alternating gradient focusing. The synchrotron cannot transport a beam with large momentum spread because the sizable dispersion function causes a significant shift in the closed orbit of the off-momentum particle and the beam hits a vacuum chamber [32]. However, a large momentum acceptance can be achieved with both a scaling and non-scaling FFAG. The effect on the beam position of momentum change for EMMA is shown in the plot in Figure 7. This shows that only a small change in beam position is incurred for a large momentum change.

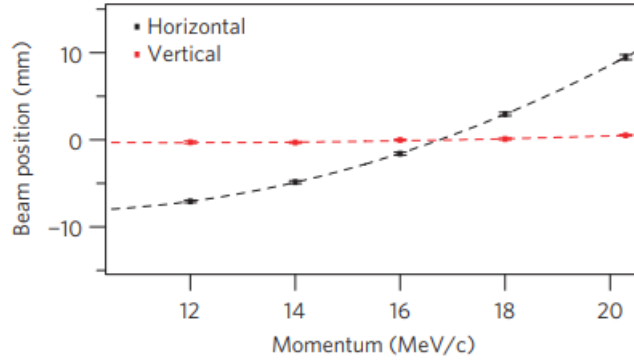


Figure 7: A plot of the horizontal (black) and vertical (red) beam positions against momentum for the EMMA FFAG. [31]. This shows that for the acceleration of 10 MeV the vertical beam position changes by less than 1 mm and for the horizontal beam position this is less than 20 mm.

The reason FFAGs have large momentum acceptances is because the closed orbit shift due to momentum spread is very small. In the case of the scaling FFAG equation (3), the scaling condition, shows that this must be a requirement for scaling FFAGs. A smaller closed orbit shift means a smaller dispersion function and therefore the beam is not lost so readily. Non-scaling FFAG's however break the scaling conditions but these still have very small dispersion functions. Therefore a large momentum acceptance is still possible with ns-FFAG.

FFAG optics ultimately have the advantage of this large momentum acceptance. This is why they are used for common transport, they allow the transport of a range of different energy beams to be transported in the same lattice with relatively small, tolerable orbit excursions as illustrated by Figure 7. A potential advantage of this is that it reduces the need for multiple transport lines which would be required if standard optics were used. Therefore complexity and total magnet cost could be reduced through the use of FFAG transport. Consequently, FFAG optics have potential use in ERLs where multiple discrete energy beams need to be recirculated such as in the CBETA design [17] and for ion/proton therapy gantry design [33] in which varying energy is required and also a reduction in the mass of the gantry is preferred.

## 4 Review of Energy Recovery Linacs

The principle of an energy recovery linac was invented by Mary Tigner, the defining insight is that an RF accelerating system could be used to transfer energy from an already accelerated beam into a newly injected beam through the electric field in the cavity. As shown in Figure 8, in this original concept the beam is turned back upon itself and re-enters the accelerator where it gives back its energy to the accelerating field, provided that the path length through the magnet system has been chosen correctly [34].

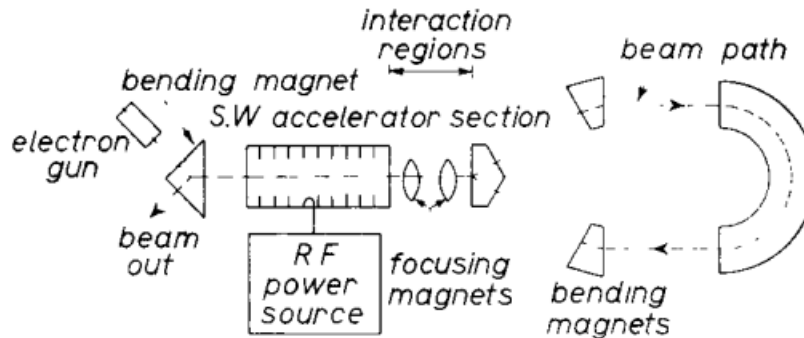


Figure 8: A schematic of the first ERL design [34]. Here the electron is accelerated through an RF cavity then bent through a dipole with a total path length designed to give a phase change of  $180^\circ$ . This beam (travelling to the left) is then interacted with a secondary beam that has just been accelerated (travelling to the right). The bent and interacted beam is then passed through the RF system where it is decelerated, as it is out of phase with the RF system, then dumped.

In other words, in an ERL the path length of the recirculation is chosen such that the beam synchronizes with the decelerating phase of the RF cavity; the energy from that beam is transferred to the field. The operation of ERLs is further explained in Section 2.

The first successful demonstration of same-cell energy recovery was during the July 1986 run of the Stanford SCA/FEL [35], over 20 years after the invention of the ERL. A diagram of the Stanford SCA, a single pass ERL, is presented in Figure 9.

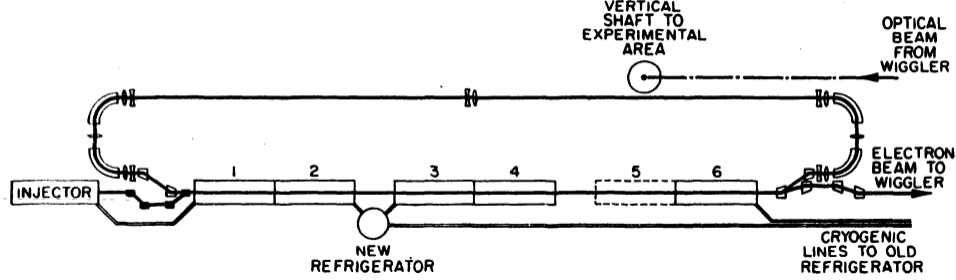


Figure 9: The Stanford SCA single pass energy recovery linac in a configuration that includes a wiggler to be used as a light source [35]. In this image RF cavity 5 is shown in a dotted line as it was non-operational for this particular experiment. The path length of the return loop in this ERL is designed to create a  $180^\circ$  phase shift and set the beam to decelerate on the second linac pass. The path length correction on this machine was limited to changing the current in the dipole magnets [35].

In this first demonstration of an energy recovery linac the energy used to accelerate the 49 MeV beam was recovered in the same RF cavities that initially accelerated the beam i.e same-cell energy recovery. Figure 10 shows the first demonstration of energy recovery from the experimental RF cavity power trace.

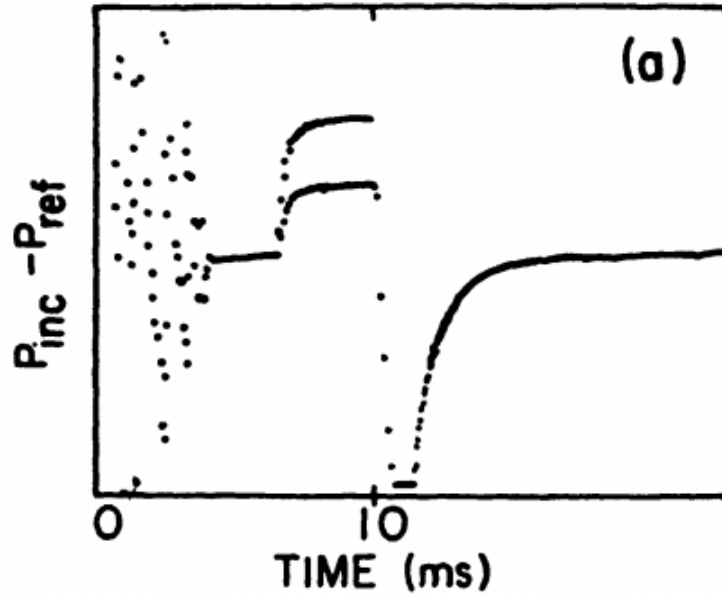


Figure 10: A plot of net power supplied (incoming RF power minus reflected power,  $P_{inc} - P_{ref}$ ) against time, otherwise known as an RF power trace, for the Stanford SCA [35]. There is a notable dip in the RF power supplied at around 10 ms. This dip occurs as energy is recovered so temporarily there is less power supplied to the RF cavity. This dip is the evidence of energy recovery.

The Stanford SCA/FEL was a single pass ERL, however energy recovery can be repeated on multiple decelerating passes. This is a multi-pass ERL, which as explained in Section 2 can be used to provide beams of multiple discrete energies which could be used for a range of applications within a single machine. Currently,

multi-pass ERLs have only been constructed for normal conducting RF systems which have been used mainly for free electron laser (FEL) applications. However, as suggested in Section 2.3 these are limited in terms of current and maximum energy.

One of the first machines created that demonstrated energy recovery and the applications of multi-pass ERL's is the Novosibirsk Free Electron Laser (FEL) facility. It is claimed that the Novosibirsk ERL is the first and only multi-turn ERL in the world [36]. As seen from Figure 11, the Novosibirsk ERL is an unusual bi-planar ERL which has recirculation loops in both the horizontal and vertical planes.

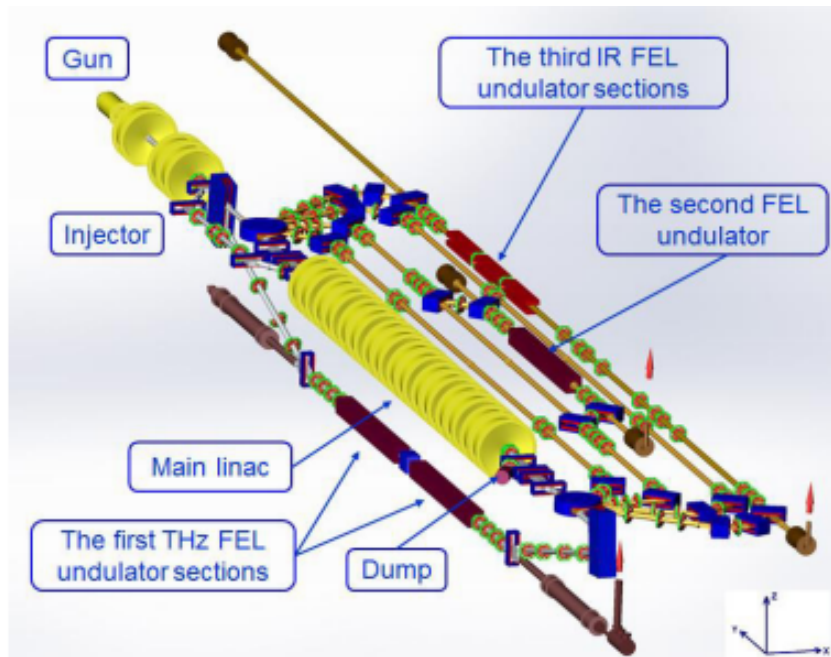


Figure 11: The Novosibirsk 4-pass ERL [36] facility which includes 3 FELs (the most recent upgrade). The Novosibirsk ERL is a normal conducting ERL mounted on the ceiling. It is a bi-planar machine with the first FEL, producing THz radiation, constructed on a vertical return loop. In the horizontal plane there are three recirculation lines, two of which incorporate FELs. The Novosibirsk ERL has the possibility to operate as a single pass ERL through the first FEL, on this pass through use of a spreader and recombiner system the configuration can be changed to 4-pass operation. The maximum beam energy, which traverses the third FEL, is 42 MeV with 11 MeV on the first pass and 20 MeV through the second FEL.

In 2009, the Novosibirsk ERL FEL facility demonstrated energy recovery of a beam with large energy spread [37] after use of the electron beam in a free electron laser. The FEL caused a large energy spread however, energy recovery was still successfully performed on the beam. This shows that it is possible to construct a multi-user light source facility based on a multi-pass ERL.

With the present Novosibirsk upgrade [36], this facility now has the capability of a 4-pass ERL with three individual FELs. Two of these FELs are the worlds most powerful (in terms of average power) sources of coherent, narrow-band (less than 1% energy spread) radiation in their wavelength ranges [36]. Table 1 shows the parameters of these FELs.

Parameter	FEL 1	FEL 2	FEL 3
Beam Energy (MeV)	11	20	42
Radiation Type	THz	IR	IR
Wavelength Range ( $\mu\text{m}$ )	80 - 240	40 - 80	5 - 20
Average Power (kW)	0.5	0.5	0.1
Peak Power (MW)	1	1	-
Pulse Length (ps)	100	50	-
Bandwidth	<1%	<1%	<1%

Table 1: The parameters of the three free electron lasers constructed at the Novosibirsk ERL FEL facility. The parameters here are collated from [38] and [39], however as the third FEL is still in commissioning certain parameters, denoted by -, are unavailable in the literature currently.

As a normal conducting RF ERL the Novosibirsk facility is a low energy, high-current machine with a maximum energy of 42 MeV [40], in line with the first pass energy of CBETA, an SRF machine. This maximum energy is ultimately the limiting factor on the FEL radiation produced. The maximum bunch charge at the Novosibirsk ERL is 1.5 nC with a repetition rate of 22.5 MHz [36], resulting in an average beam current of 33.75 mA. However, this is soon to be upgraded through a new RF gun/injector to increase the beam current up to 100 mA [41].

The highest energy recirculating linac facility is Continuous Electron Beam Accelerator Facility (CEBAF). CEBAF was originally built as a 5-pass recirculating linac machine with two separate linacs; a north linac and a south linac, as shown in Figure 12.

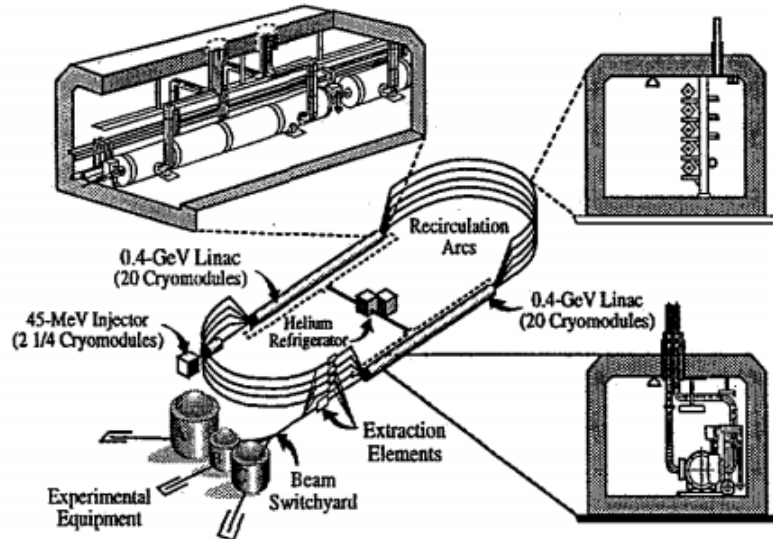


Figure 12: The CEBAF initial construction in 1995 [42]. This is designed to achieve a top energy of 4 GeV as a 5-pass machine with four  $180^\circ$  recirculation arcs. The beam is injected at 45 MeV and accelerated by +400 MeV per pass of each linac.

This original configuration of the CEBAF superconducting recirculating linac was designed to operate at a top energy of 4.045 GeV with an average beam current of  $100 \mu\text{A}$  [42]. To achieve this energy the beam is injected at 45 MeV and passes each linac a total of 5 times where it is accelerated +400 MeV per pass by the 3 MV/m linacs and recirculated by the isochronous, constant traversal time, recirculating arcs [42]. Table 2 collates the main parameters for each of the upgrades and experimental configurations of CEBAF. CEBAF was initially designed as a laboratory devoted to the exploration of matter that interacts through the strong force [43] i.e as a test-bed for Quantum Chromodynamics.

In 2003 a single pass energy recovery experiment was performed on CEBAF. This utilised energy recovery that was not same-cell, as described in Section 2.1. In this demonstration the beam was injected at 56 MeV into

the north linac where the beam was accelerated to 556 MeV and then recirculated via the isochronous arcs to the south linac where it was accelerated again by the south linac from 556 MeV to 1056 MeV [10]. The beam then passed through a  $\lambda_{RF}/2$  delay chicane which delayed the beam by half an RF wavelength  $\lambda_{RF}$  and therefore the beam is out of phase by  $180^\circ$  entering the cavity where it is decelerated and energy recovered. A diagram of this experimental set up is shown in Figure 2. The evidence for this demonstration of energy recovery, as for the Stanford SCA shown in Figure 10, is primarily from the RF transients of a linac cavity displayed in Figure 13.

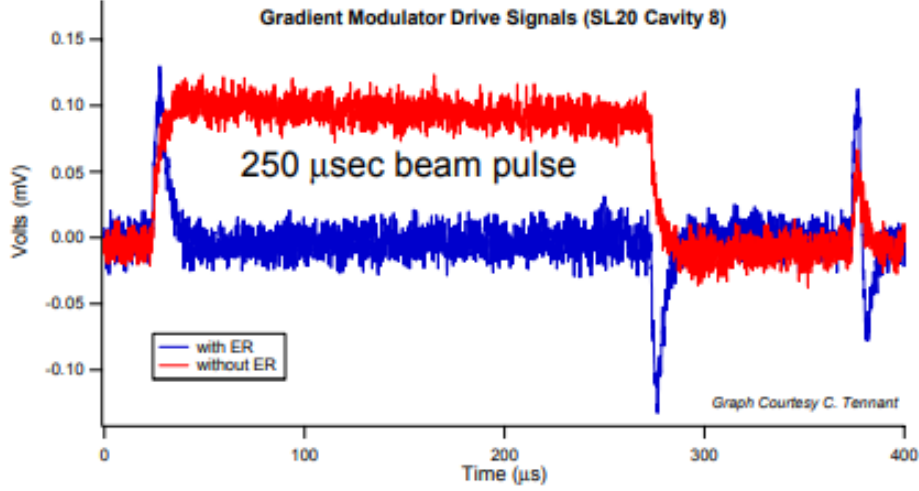


Figure 13: The RF transient plot (cavity supply voltage against time) of the last cavity of CEBAF’s south linac, cavity 8 [10]. The plot of cavity supply voltage against time is shown for the energy recovery (blue) case and the case where energy is not recovered (red). There is a notable drop in the cavity supply voltage from around  $40\ \mu\text{s}$  to  $270\ \mu\text{s}$ , for the energy recovery case in comparison to the non-recovered case this means that the cavity is being supplied energy from the beam and therefore that energy is recovered from the beam.

The CEBAF energy recovery experiment is subsequently the first demonstration of single pass energy recovery in a superconducting ERL. It is contentious that this is only single pass energy recovery as energy is recovered in two linacs. However, as discussed in Section 2.1 energy recovery is only recovered on one pass of each linac and therefore this is not true multi-pass energy recovery.

As of early 2001, CEBAF has operated routinely at around 6 GeV [44] as a 5-pass recirculating linac. This was achieved through an upgrade of the cavities to an average accelerating gradient of 7.5 MV/m, the upgrade program also allowed the beam current to be increased to  $160\ \mu\text{A}$  [45].

CEBAF has recently (2018) completed another upgrade to a top energy of 12 GeV recirculating linac. This is an upgrade from 6 GeV, which increased the energy gain by the beam per pass of both the north and south linac to +1.09 GeV whilst also adding a further recirculation arc to the south side which is required for multi-recirculation energy recovery experiments [46]. Figure 14 shows this most recent configuration.

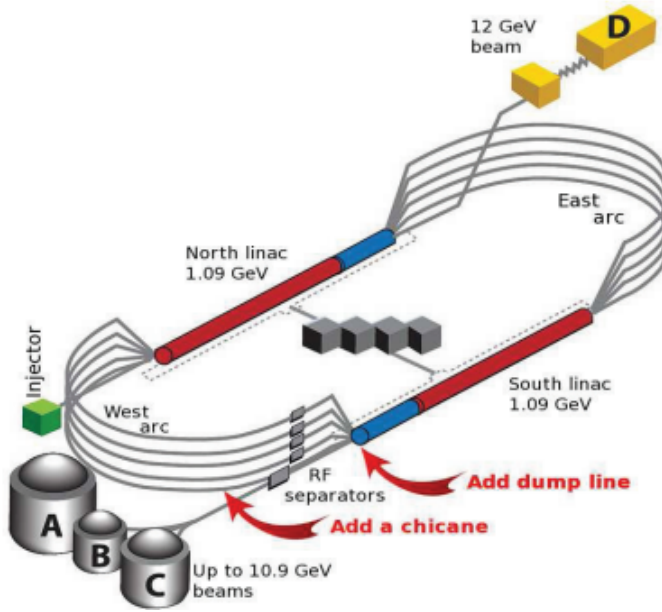


Figure 14: The 2018 upgraded CEBAF machine [46]. The CEBAF RL has now been upgraded to a total of 10 recirculation arcs. The blue sections of the linac show the upgraded and extended linac sections which upgrade the acceleration per pass of the linac to +1.09 GeV. On the left hand side of the figure, near the experimental halls A, B, C a beam dump and a new recirculation arc with a path length adjustment chicane has been installed.

The main purpose of this upgrade is to conduct energy recovery experiments on CEBAF and to demonstrate multi-pass energy recovery on a superconducting RF machine. This will not be same-cell energy recovery. The current experimental program is outlined by F. Meot et al as: 1-pass ER at 500 MV/linac (a repeat of the 2003 ERL experiment [10]), 3-pass ER and 5-pass ER, at low MV/linac to avoid synchrotron effects [46]. There will also be experimental efforts to operate CEBAF at high average current, aiming for the milliampere range.

Year	Total Pass No.	Mode (ERL or RL)	Beam Energy (GeV)	Current ( $\mu\text{A}$ )
1995	5	RL	4.045	100
2003	1	ERL	1.056	-
2001	5	RL	5.71	150
2018*	5	ERL	12	100

Table 2: A table of collated parameters from the various upgrades of the CEBAF recirculating linac and the energy recovery experiments performed. The \* here denotes the planned operation of the 2018 upgrade of CEBAF. However, this is still in the commissioning phase. [42], [10], [44], [45], [46].

A main motivation of CEBAF as a multi-pass ERL and for many other ERL projects is the application of ERLs in electron-ion colliders (EIC). The CEBAF project is of interest to the two competing EIC projects in the USA, the Jefferson Lab Electron Ion Collider (JLEIC) [47] and the Electron Relativistic Heavy Ion Collider (eRHIC) [3] at Brookhaven National Laboratory, as ERLs are postulated for electron cooling, a process used to increase the luminosity of electron-ion colliders.

Electron cooling is a process in which a beam of electrons is used to thermalise an ion beam through Coulomb scattering. Coulomb scattering leads to energy exchange between the two kinds of particles and, if the electron beam is monochromatic enough and the particle trajectories are parallel, the electron beam will play the role of "cooler" absorbing the excess energy of the "hot gas" of heavy particles [48]. The electrons can then easily be removed from the beam in a bending section. The effect of this process is to reduce the beam emittance and momentum spread [49] of the ion beam which therefore causes an increase in EIC luminosity. Electron cooling is most efficient when the injected ion beam has small emittance and momentum spread [50]. Therefore, as linac and ERLs have typically better beam quality; smaller emittance (as it is governed solely by the injector) and a small momentum spread, these are two pertinent qualities for electron cooling. In summary, the efficiency of electron cooling applied to stored ion beams depends very much on the quality of the electron beam [51]. As



ERLs can achieve high repetition rate and subsequently an increased electron cooling rate, the development of ERLs are vital to electron-ion collider development.

The accelerator of prime interest in this project is CBETA. This is the first proposed SRF multi-pass energy recovery linac with non-scaling FFAG (ns-FFAG) racetrack [2]. Therefore, the CBETA project is unique in two ways: a potential first demonstration of multi-pass same-cell energy recovery in a SRF machine and a first demonstration of common transport, in which each of the discrete energies of the ERL is recirculated in the same transport line, as explained in Section 3.3. CBETA has a 4th pass top design energy of 150 MeV and is designed to cause the beam to gain energy by +36 MeV per linac pass with a targeted average current of 40 mA [1]. The single pass of CBETA has recently been completed and experiments into single pass same-cell energy recovery are being performed at the time of writing. The CBETA project is explained in much greater detail in Section 5.

The main rival to CBETA's target of obtaining a first experimental demonstration of multi-pass energy recovery using superconducting RF is the S-DALINAC ERL at TU, Darmstadt. Recently, S-DALINAC was extended from a twice to a thrice recirculating linac to increase the maximum achievable energy to the design energy of 130 MeV [52]. Figure 15 shows the upgraded S-DALINAC ERL.

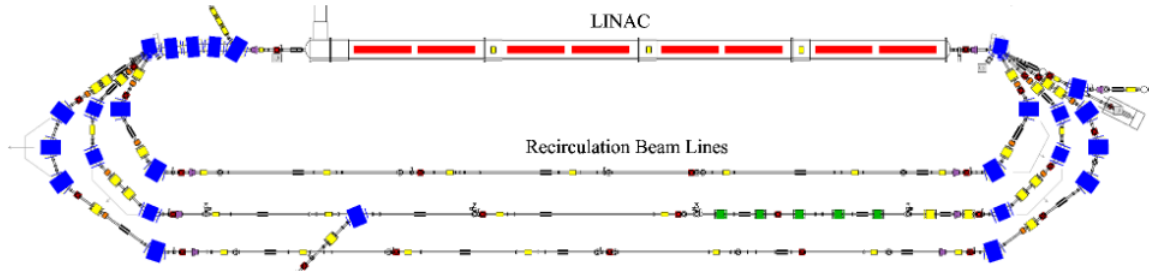


Figure 15: The 3-pass recirculating SRF linac S-DALINAC [52]. This shows the upgrade of S-DALINAC in which the central recirculation line has been added. This includes adequate path length correction systems so that S-DALINAC can operate as a 2-pass ERL. The path length is corrected by a series of bellows and quadrupoles in the arcs.

With a beam current of 130 MeV this ERL operates in a similar energy range to CBETA. However, both S-DALINAC and CBETA have only been operated so far at low current:  $1.2 \mu\text{A}$  for S-DALINAC [53] and  $5 \mu\text{A}$  for CBETA.

The new recirculation linac at S-DALINAC features a path length adjustment system capable of changing the phase of the beam by a full  $180^\circ$  of RF phase and, thus, allowing a shift in the timing of the electron bunches to the decelerating phase [54]. Therefore, this makes 2nd pass energy recovery experiments possible. The outer recirculation line, as shown on Figure 15 can't operate in energy recovery mode however is routinely used as part of a 3-pass recirculating linac for nuclear physics experiments. First pass energy recovery operation was completed in August 2017 with an efficiency of  $92^{+3.7}_{-13.9}\%$  [53]; beam dynamics simulation and RF cavity work are required before 2nd pass energy recovery can be successfully demonstrated.

Since S-DALINAC's third recirculation pass is already built and work is continuing toward 2-pass ER, this accelerator currently looks the more likely candidate to demonstrate multi-pass energy recovery in a superconducting RF machine first. The milestone for CBETA to achieve multi-pass ER isn't until December 2019 [17].

The first and only ERL to be built in the UK was the Accelerators and Lasers in Combined Experiments (ALICE) ERL. This was a single pass SRF ERL facility with a maximum beam energy of 35 MeV. The path length correction in ALICE involved a set of bellows used to mover the whole arc longitudinally [55]. This 'trombone' style scheme can be used to change the phase of the beam by a full  $180^\circ$ . ALICE was designed as an energy recovery linac prototype [56] for now the defunct 4GLS project (An ERL multi-FEL project) [57]. However, this instead became an injector into EMMA [31], the world's first ns-FFAG, and a test accelerator for next generation light sources such as FEL and inverse Compton scattering sources.

The inverse Compton scattering source on ALICE was the first published trial of inverse Compton scattering on an ERL. This used a customised table-top chirped pulse amplification (CPA) multi 10 TW laser system [58]. The beam and laser were collided head-on to produce 21.5 keV X-rays with a flux of  $9 \times 10^4$  ph/s [58]. This was much less than the  $9 \times 10^7$  ph/s flux simulated for the head-on case [59]. Possible justifications for the discrepancy are that the experiment was carried out over the duration of only 2 days and no extra focusing modifications of



the ALICE lattice were made. This would therefore mean that the beam and pulse sizes were not optimal for the ICS interaction. The X-ray pulses made through the Daresbury ICS were designed to be proof of principle THz/X-ray pulses for use in pump-probe studies of dynamics [58]. Subsequently, these pulses were very short at around 150 fs [58].

The most prominent ERL inverse Compton source is the ICS constructed on cERL at KEK, Japan. This used a custom focus and a dedicated bow-tie laser recirculation cavity to improve the flux of the source. The configuration of cERL as an inverse Compton source and a diagram of the laser recirculation cavity for the inverse Compton interaction are shown in Figure 16.

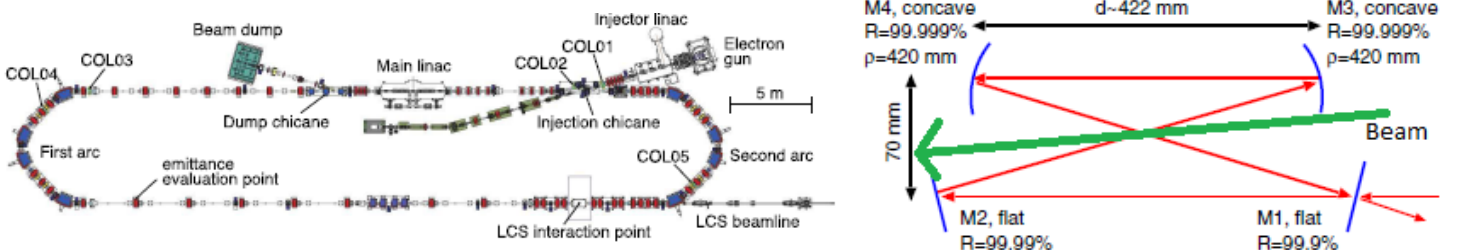


Figure 16: Left: The single pass cERL machine. This current configuration is built in order to incorporate an ICS interaction point in the recirculation loop, this is where the laser recirculation cavity is implemented. Right: The bow-tie laser cavity which recirculates an Nd:YAG laser through the 4 mirror configuration at a repetition rate of 162.5 MHz. The focussed electron beam is interacted with the recirculated laser at the centre of this cavity to produce the inverse Compton scattered X-rays. [6]

cERL is a single pass ERL which operates at a maximum energy of 20 MeV, for this particular experiment it was operated at an average beam current of  $58 \mu\text{A}$  [6].

The fact that a focusing system was used to reduce the transverse size of the electron beam in the interaction and that a laser recirculation cavity was used to improve the repetition rate of the inverse Compton interaction shows that this was designed as a usable source of ICS X-rays for experimentation. This experiment created 6.95 keV X-rays at a flux of  $2.6 \pm 0.1 \times 10^7 \text{ ph/s}$  [6], the highest flux of an ERL inverse Compton source demonstration.

However, both the ALICE ICS and cERL ICS are still low flux demonstrations. This is in comparison to well established ICS sources such as the Lyncean Technologies Compact Light Source (CLS) which is a commercial storage ring ICS designed to produce  $3 \times 10^{11} \text{ ph/s}$  [60]. The original first demonstration on ALICE was just a proof of principle experiment in which there was no laser recirculation cavity, thereby the flux was limited by the repetition rate of the laser in the kHz range. In cERL a laser recirculation cavity was utilised and therefore this is the first ICS designed to establish if inverse Compton scattering sources is a viable X-ray production method for users. However, cERL demonstrated ICS with a very low current due to a small 0.355 pC [6] bunch charge, hence the low flux. Furthermore, the ERL parameters aren't optimised towards inverse Compton scattering experiments which are enhanced, from a beam dynamics perspective, through small emittance and high current. To summarise, there hasn't yet been an experiment based on ICS on an ERL designed specifically for an ICS based light source.

## 5 CBETA

The Cornell University Brookhaven National Laboratory Energy Recovery Linac Test Accelerator (CBETA) is a 4-pass superconducting RF energy recovery linac [2]. The project is unique in two ways: it could potentially be the first demonstration of multi-pass (multiple passes of the same linac) same-cell energy recovery within a superconducting RF machine and the first common transport ERL, where the nominal energies of each pass are transported in the same return loop. The project aims to recirculate a 40 mA electron beam [1] through 8 passes of the linac (4 accelerating, 4 decelerating) at the nominal energies 6 MeV (injection/8th pass), 42 MeV (1st/7th pass), 78 MeV (2nd/6th pass), 114 MeV (3rd/5th pass) and 150 MeV (4th pass). A diagram of CBETA is shown in Figure 17.

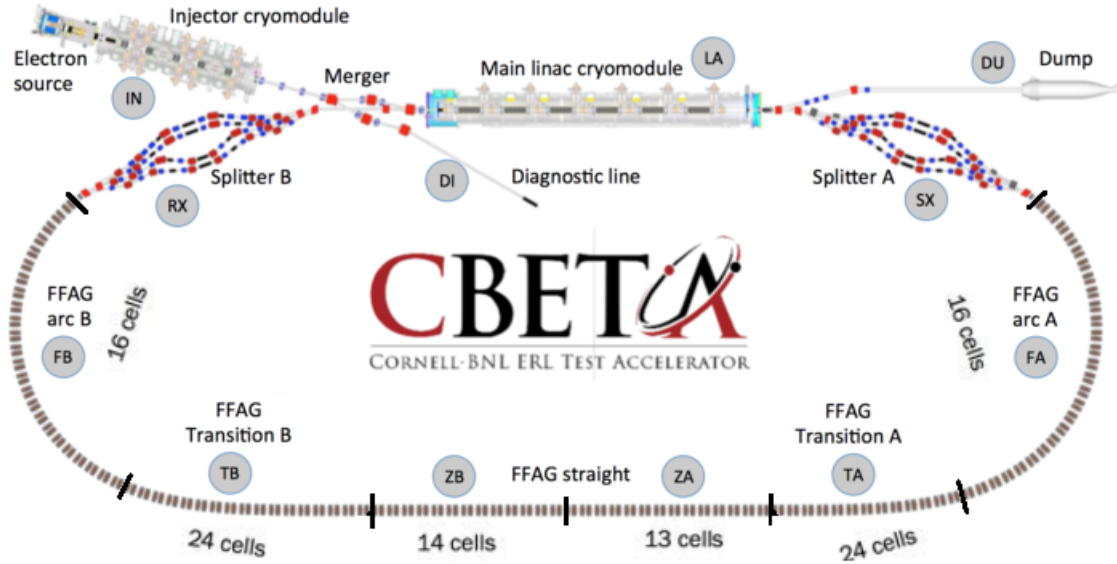


Figure 17: A diagram of the CBETA ERL [17]. In CBETA the beam is injected (IN) at an energy of 6 MeV this is then merged into the 10 m main linac cryomodule (LA) with an accelerating gradient of nominally 6 MV/m up to 16 MV/m. The beam then traverses the splitter where the beam travels down one of four conventional transport lines configured for the 42, 78, 114, and 150 MeV energies where the  $R_{56}$  and path length is corrected by a system of bellows allowing for up to  $\pm 10^\circ$  of RF phase adjustment. The beam then enters the return loop, this is constructed from repeating modular sections of magnets named cells, as described in Section 5.1. In the return loop the beam passes through the FFAG transport arc (FA), which is designed to have a large energy acceptance so each of the nominal energies (42, 78, 114, 150 MeV) can be transported through it. The transition section (TA) corrects the trajectory of each energy, which through the FFAG arc (FA) is oscillating and transversely offset from the reference orbit, close to the reference orbit. The FFAG straight (ZA, ZB) continues to transport the nominal energies close to the reference trajectories. The TB transition and FB arc mirror the functions of TA and FA. The recombiner (RX) then can provide an additional  $\pm 10^\circ$  of RF phase adjustment before the beam is passed into the linac (LA) again for either re-acceleration or deceleration

The CBETA project is of interest not only because it could be the first multi-pass same-cell SRF ERL and demonstration of common transport ERL. It demonstrates a combination of techniques that were pioneered at the Cockcroft Institute and Daresbury laboratory; non-scaling FFAG and energy recovery linacs. Local projects such as the EMMA ns-FFAG ring [30], the worlds first non-scaling FFAG, and ALICE [56], the UK's first energy recovery linac are cited as influences on the design and motivation for CBETA. Therefore, there is considerable interest in this project.

The CBETA ERL is aimed as a project in order to demonstrate the technology required for electron cooling by multi-pass ERL's for the proposed eRHIC [3] and JLEIC [47] electron-ion collider project which have both considered using ERLs as potential electron coolers. CBETA has also been proposed for an electron beam source for inverse Compton source experiments [61]. A table of parameters for the CBETA project are shown below in Table 3.

CBETA Parameter	Value
Beam Energies $E_e$ (MeV)	42, 78, 114, 150
No. Turns	4
No. Linac Passes	8
RF Frequency $f_{RF}$ (GHz)	1.3
Bunch Frequency $f_{bunch}$ (MHz)	325
Accelerating Gradient $E_{acc}$ (MV/m)	6-16.2
Normalised Transverse Emittance $\varepsilon_n$	1
rms Bunch Length $\sigma_z$ (mm)	0.9
Bunch Charge $Q$ (pC)	1-123
Average Beam Current $I$ (mA)	40

Table 3: A table of the main parameters for the 4-pass CBETA ERL [17].

Simulations of the CBETA lattice are shown within this section. These simulations use the Bmad [62] beam dynamics code and the Tao [63] program created by D. Sagan et al. Together these form a Fortran beam dynamics code, based around the functionality of the MAD codes, but tailored for the requirements of the Cornell Laboratory for Accelerator Based Sciences (CLASSE). The full 4-pass CBETA lattice in was created in Bmad by Dr. J. Scott Berg [64]. The simulations presented for CBETA in this report have been conducted using Bmad and Tao with altered versions of the CBETA lattice.

## 5.1 FFAG Cell

The FFAG arc cells are based upon the design of a non-scaling spiral style FFAG. This is as they are created from a focusing quadrupole and a combined function magnet which has a dipole and defocusing quadrupole component. The structure of a single FFAG cell is shown in Figure 18.

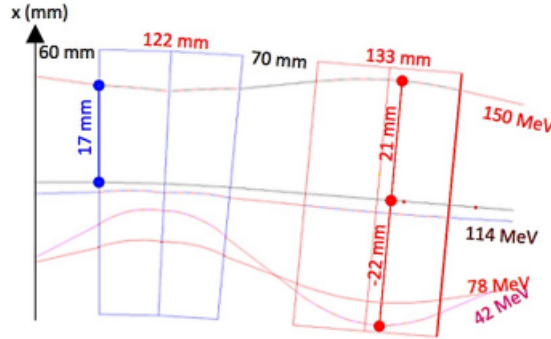


Figure 18: A diagram of the FFAG cell with the focusing magnet QF in blue and the combined function defocusing magnet in red.  $x$  the transverse position against  $s$  the longitudinal direction orbit plots are shown for each of the four nominal energies 42, 78, 114, 150 MeV with labelled  $x$  offsets for each energy. [65]

A table of parameters for this FFAG arc cell is shown in Table 4.

<b>FFAG Arc Cell Parameter</b>	<b>Value</b>
Bend Angle ( $^{\circ}$ )	5
Arc Cell Length (mm)	402
Focusing Magnet Length (mm)	133
Combined Function Magnet Length (mm)	122
Integrated Focusing Magnet Strength (T)	-1.528
Integrated Combined Function Magnet Strength (T)	1.351
Integrated Field on Axis, Defocusing (Tm)	-0.037

Table 4: The parameters of the CBETA FFAG arc cells FA and FB. This is the standard FFAG cell that all of the subsequent cells such as those in the transition section (TA and TB) and in the straight section (ZA and ZB) are variations of. The integrated magnet strength and magnet lengths are standard throughout the FFAG return loop.

In the straight sections ZA and ZB the standard FFAG cell is modified by removing the dipole component of the combined function magnet. By varying the drift lengths between cells compared to those used for the FA and FB arc cells the same tune per cell can be retained, This is as the path length of the electrons through these cells changes with energy as the paths are no longer curved.

The transition cells differ from the arc cells as for these the integrated field on axis i.e the dipole component is adjusted for each cell. This is done by offsetting the BD magnet and therefore changing the dipole component of the magnet. The drift lengths between cells is also adapted to retain the same tune per cell. A much more detailed explanation of the creation of the transition cells is shown in [17].

## 5.2 FFAG Return Loop

The FFAG return loop is the common transport section in which the nominal energy beams all travel through the same optics i.e the FFAG beamline. This is therefore traversed by the 42, 78, 114 and 150 MeV passes of the ERL. For reference, in Figure 17 this consists of the FA and FB arcs, the TA and TB transition sections as well as the ZA, ZB straight. The structure of this is: FA, TA, ZA, ZB, TB, FB. The purpose of this section is to recirculate the beam from splitter to recombiner in a single beam line. The lattice functions are shown in Figure 19.

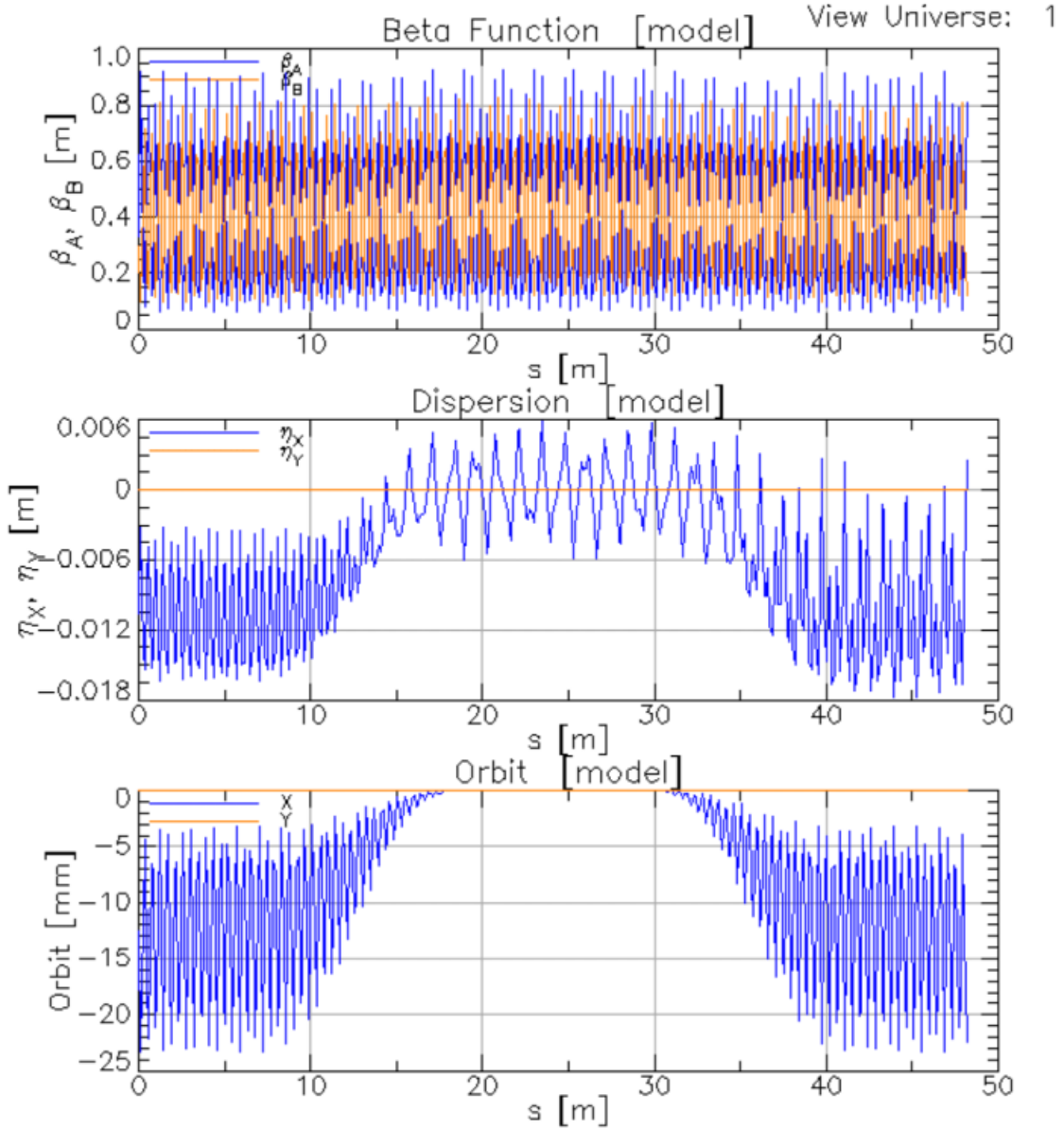


Figure 19: The single pass FFAG return loop lattice functions as simulated in Bmad. This is comprised of the FFAG arcs FA and FB, the transition sections TA and TB and the FFAG straight ZA and ZB. Top: A plot of the  $\beta$  functions throughout the return loop. These are periodic all throughout the return loop in all of the sections (arc, transition etc.). The section does not change the  $\beta$  functions. Middle: Dispersion plot of the single pass return loop. The dispersion in the FA arc is periodic, as this progresses through the transition and straight this periodicity is lost. Comparing the FA arc ( $\approx 0-9$  m) with the FB arc ( $\approx 40-49$  m) we can see that the dispersion is aperiodic in FB i.e the same structure of the dispersion function is not recovered throughout the return loop. Bottom: Orbit plot of the return loop. The  $x$  orbit offset in the arcs (FA, FB) centres at around  $-13$  mm. The orbit is oscillatory around this point. The transition sections TA ( $\approx 9-17$  m) and TB ( $\approx 31-40$  m) dampen this oscillation and also reduce the orbit offset to zero i.e the reference orbit through the ZA, ZB FFAG straight.

The FA and FB arcs are designed to supply  $60^\circ$  degrees of bend per arc [17]. However, each nominal energy passes through the arc. Due to the arc being composed of permanent magnets the radius of curvature differs for each energy as shown by the momentum  $p$  dependence on the radius of curvature  $\rho$  as given by

$$\frac{1}{\rho} = \frac{Bq}{p} \quad (4)$$

where  $B$  is the magnetic flux density which is fixed here because permanent magnets are used and  $q$  is the particle charge which here is the elementary charge constant  $e$  as CBETA uses electron beams. This explains the orbit excursions from the reference orbit as seen in Figure 19 for the recirculation arcs FA and FB. Comparing this, the single pass orbit in the return loop with Figure 20 the fourth pass orbit in the return loop it is possible to see that the orbit offsets in the arcs have changed from around -13 mm to +22 mm.

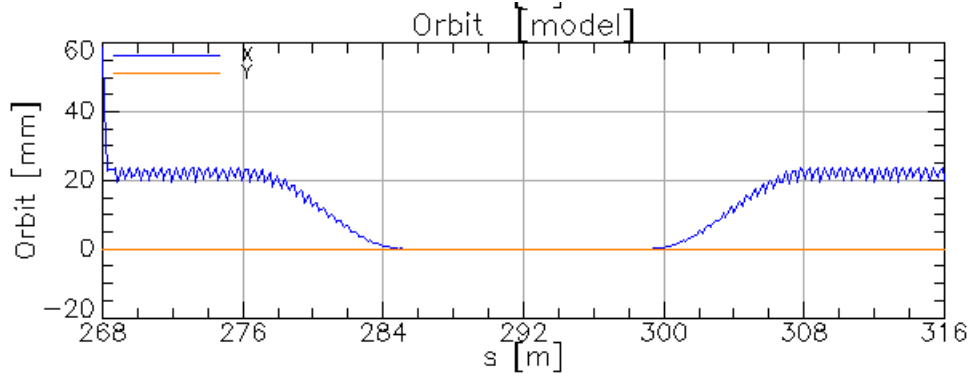


Figure 20: The 150 MeV 4th pass CBETA orbit plot. The  $x$  offset from the reference orbit is around 22 mm in the FA arc ( $\approx 268$ -277 m) and FB arc ( $\approx 307$ -316 m). The transition sections TA and TB ( $\approx 277$ -285 m, 299-307 m) which bring the orbit onto the reference orbit for the FFAG straights ZA and ZB.

The transition sections TA and TB in the return loop are designed to bring the orbits in the arc at and near the design energies onto the axis of the straight [17] and also provide  $40^\circ$  of bend. The cell parameters are adiabatically varied in this section in order to accomplish the return to the reference orbit. The transition section is designed such that the emittance growth through the transition is minimised hence the transition is adiabatic. The construction of this is based upon minimising the normalised action, which when compared to the normalised emittance shows the emittance growth in the transition section [17]. This is an optimisation process which is shown in full in [17]. It is this particular optimisation that gives an adiabatic transition like that visible in the orbit and dispersion plots of Figure 19.

In the ZA, ZB straight sections the arc cell is adapted from the arce cell shown in section 5.1 through altering the defocusing magnet so that it has zero magnetic field on its axis [17]. The defocusing and focusing magnets, as in the arc, will have the same integrated field (with opposing signs) and length. Therefore, the only free parameter is the drift lengths which are adapted to match the tunes of the straight cells in the ZA, ZB straight with those in the FA, FB arc. The results of the straight cell design are seen in the minimised orbit offset in  $x$  and the continuation in periodicity of the  $\beta$  functions. Both of these properties can be seen in Figure 19.

### 5.3 RF System

The main linac cryomodule (MLC) for the CBETA project is a 6 cavity Superconducting RF linac operating at 1.3 GHz (L-band) with 7-cell Niobium cavities [17]. The linac in CBETA operates in continuous wave (CW) mode. This is where the linac accelerates the beam continuously so the duty cycle is 100% and therefore linac is said to operate in continuous wave (CW) mode [66]. The total length of the MLC is 9.80 m with each 7-cell cavity 0.81 m in length [17]. Therefore, the fill factor for CBETA is 0.496. The CBETA MLC is shown below in Figure 21.





Figure 21: The Main Linac cryomodule of the CBETA project. This contains the six 7-cell Niobium SRF cavities operating at 1.3 GHz. The fill factor is 0.496 since the cryomodule also includes the necessary vacuum hardware, liquid helium cryogenics system (operating at 1.8 K) and the higher order mode absorbers.

The accelerating gradient of the CBETA MLC is nominally 6 MV/m which means the energy gain by an electron through the linac is 36 MeV/pass. However, the linac has the capability of providing a 16.2 MV/m accelerating gradient which corresponds to 78 MeV/pass of the linac. The reason the MLC is operated with  $E_{acc} = 6$  MV/m is due to the FFAG optics and their design, not the limitations of the RF system.

The CBETA MLC contains higher-order mode (HOM) absorbers. These are located between the 7-cell cavities in the MLC. These aim to have a broad-band absorbing material covering a whole range of frequencies from 1 to  $> 40$  GHz. These are cylindrical in shape and designed to ensure 400 W of HOM power can be extracted [17]. The purpose of these is to mitigate the effect of beam breakup instability. This is an instability caused by the higher-order modes which invoke a kick (typically dipole or quadrupole) to the beam. This isn't covered in any detail in this report but, as shown by G. H. Hoffstaetter et al [16], this can limit the current in an ERL.

#### 5.4 Splitter/Recombiner System and Path Length Correction

The splitter/recombiner sections, SX, RX in Figure 17, of CBETA are composed of 4 separate conventional transport lines for each of the 4 individual beam energies. Two septa magnets (common dipoles) at the start and end of the splitter sections are used in order to split the beam from the linac or the end of the return loop into the requisite energy line. These lines are designed to control the  $R_{56}$  of the beam, conduct path length correction and match the lattice functions correctly into the return loop. A diagram of the CBETA SX section is shown in Figure 22.

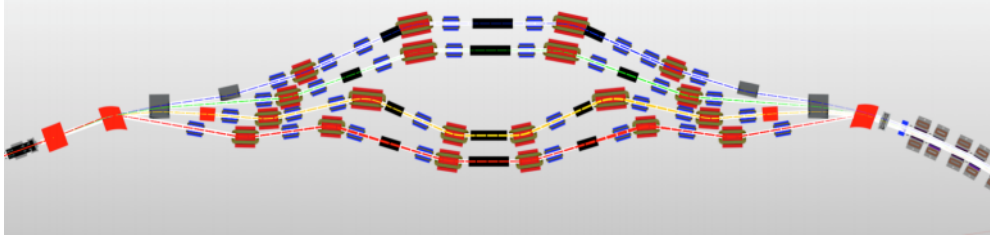


Figure 22: The SX splitter lines [17], from bottom to top S1 (42 MeV)- S4 (150 MeV). The common septa magnets (red) at the start (left) and end (right) of SX are used to input the beam from the linac and output the beam from SX into the common transport arc. The dipoles (orange) are used to bend the beam in the chicane-style lines whereas the quadrupoles (blue) are used for matching the lattice functions and  $R_{56}$  adjustment. Path length correction is controlled by the bellows (black) which can extend up to 13 mm per beam line.

In order to achieve these optics requirements, each line would need at least seven independent quadrupole magnets to satisfy the six optics parameters  $\beta_{x,y}$ ,  $\alpha_{x,y}$ ,  $\eta_{x,px}$  and single  $R_{56}$  parameter [17]. CBETA uses 8 quadrupoles per splitter beam line as this gives additional flexibility. Plots of the lattice functions  $\beta_{x,y}$  and  $\eta_{x,y}$  and orbit for the S1 (42 MeV) splitter, the bottom most splitter in Figure 22, are shown in Figure 23.



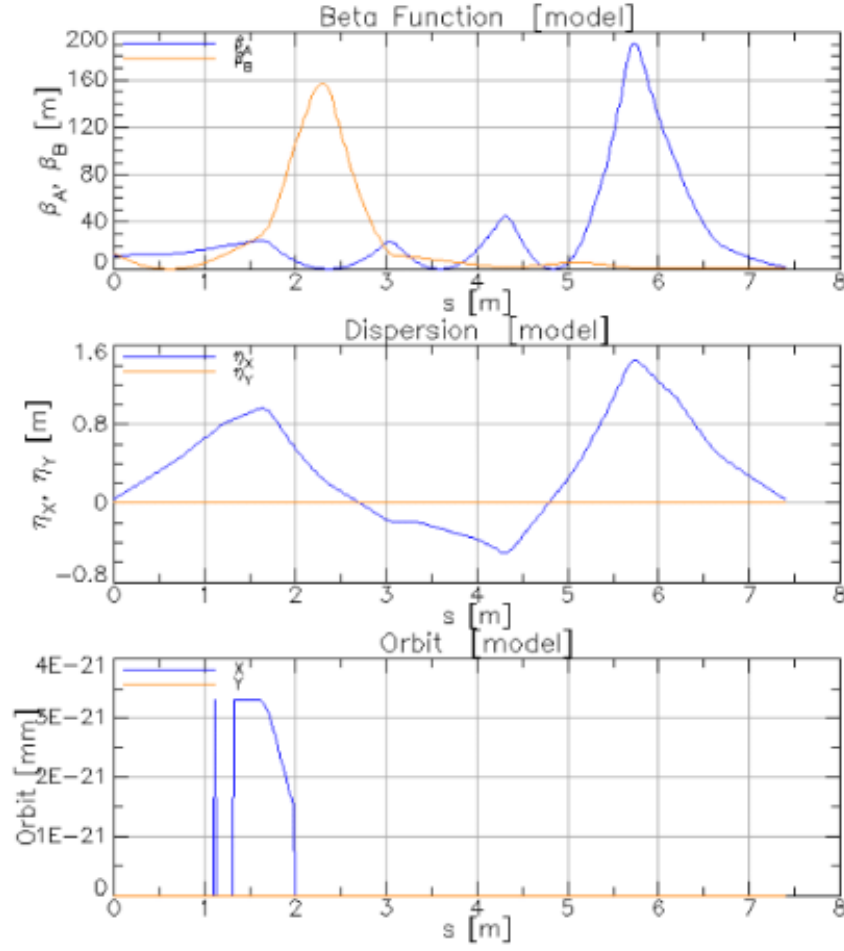


Figure 23: The lattice functions of the S1 splitter in the 4-pass configuration plotted by Tao from the CBETA 4-pass Bmad simulated lattice. Top: The  $\beta_{A,B}$  functions (for the A and B modes) through the S1 splitter. The  $\beta$  functions here peak at large values of  $\beta_y^{max} \approx 160$  m and  $\beta_x^{max} \approx 185$  m but then are minimised upon entry to the FFAG arc to prevent a large transverse beam size. Middle: The dispersion functions  $\eta_{x,y}$  through the S1 splitter line. The dispersion function  $\eta_x$  grows large as it passes through the splitter system up to  $\eta_x^{max} = 1.5$  m. The dispersion  $\eta_x$  is also positive and negative through this transport. The dispersion is also incompletely suppressed upon entry into the FFAG arc. Bottom: The orbit of the electron beam in the S1 splitter. This shows only some computational noise in the simulation, otherwise the orbit follows the reference orbit perfectly.

The path lengths of the splitter lines are adjusted through use of a series of bellows which expand to increase the path length. These bellows provide  $\pm 10^\circ$  of RF phase path length adjustment per splitter line [17]. This corresponds to 12.8 mm path length variability and therefore 25.6 mm ( $\pm 20^\circ$ ) per recirculation as there are two splitter sections per recirculation (RX and SX). RX is sometimes termed the recombiner.

However, in order to change from accelerating to decelerating the beam there would need to be a path length change for the beam that corresponds to  $180^\circ$  of RF phase. This is not possible with the path length adjustment scheme as the bellows only allow  $\pm 20^\circ$  of RF phase change per full recirculation (RX+SX). Instead CBETA operates with the length of the splitter path set so the total path length is either an integer RF wavelength and therefore accelerating or an integer +  $1/2$  RF wavelength total path length and therefore decelerating. For example, in 4-pass operation the S1 (42 MeV), S2 (78 MeV), S3 (114 MeV) splitter systems are configured so the total path length of these passes is an integer number of RF wavelengths. However, S4 the splitter traversed by the 150 MeV beam is configured so the total path length is an integer plus  $1/2$  of the linac RF wavelength [17]. Because of this the beam path length is altered to arrive with the decelerating phase of the linac. As every subsequent path length of the remaining passes is of integer RF wavelengths each pass also coincides with the decelerating phase of the linac. This enables full deceleration of the beam.

A notable downside to this is that CBETA can't run at any particular configuration from the control room. For example, to be operating in 4-pass mode and then to change to operate in 2-pass mode requires physical alteration of the S2 splitter line so it has a total path length for the 2nd pass of integer + 1/2 RF wavelengths. Splitters adjusted so the total path length on that pass is integer + 1/2 RF wavelengths are termed decelerating configurations, when this is integer RF wavelengths it is an accelerating configuration.

## 5.5 Single Pass Operation

As of the time of writing CBETA has been commissioned and performed both recirculating and energy recovery experiments for the single pass configuration. Results have recently been published for the first recirculation around the FFAG loop [67], as shown in Figure 24. However, the results of the single pass energy recovery experiment are yet to be published.

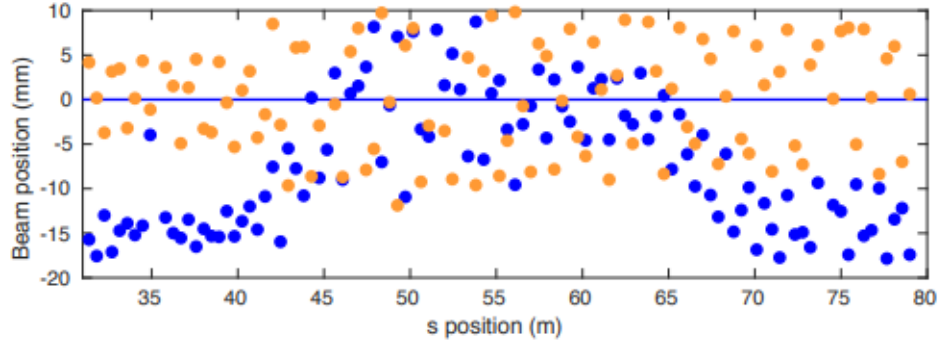


Figure 24: The first successful pass of the CBETA FFAG return loop [67]. This is a plot of the transverse  $x$  position of the beam against the longitudinal  $s$  position of the beam. The BPM positions from the actual machine (yellow) and virtual machine, a simulation of the 1-pass lattice and EPICS control system, (blue) are plotted. This shows that the beam was detected at the BPM in the TB transition section and therefore successfully traversed the FFAG return loop.

The CBETA machine is currently in shutdown whilst the 4-pass configuration is built, this includes the building of the S2-S4 splitter lines and R2-4 recombiner lines.

The single pass configuration, as can be seen from Figure 17, consists of the beam being injected at 6 MeV it is then passed through the linac in which it is accelerated to 42 MeV. The beam then traverses the S1 splitter line in a decelerating configuration and then enters the first FFAG arc (FA) where it is transported with an orbit deviation from the reference orbit to the transition section (TA) which corrects the orbit to the reference orbit. The beam then passes through the straight sections (ZA, ZB) to the second transition section (TB) where the orbit is matched into the final arc (FB). It is then passed into the R1 recombiner/splitter line which is also in a decelerating configuration. Due to both R1 and S1 being in decelerating configurations the beam is now 180° out of phase with the RF system and is therefore decelerated to 6 MeV in the linac. The energy from the 42 MeV beam is then recovered in the same RF cavities used to accelerate it. This beam is then sent to the beam dump. Another beam is then injected after energy recovery of the previous bunch and is then accelerated, the process can be repeated.

Figure 25 shows the lattice functions and orbit for the single pass configuration of the CBETA lattice as simulated in Bmad.

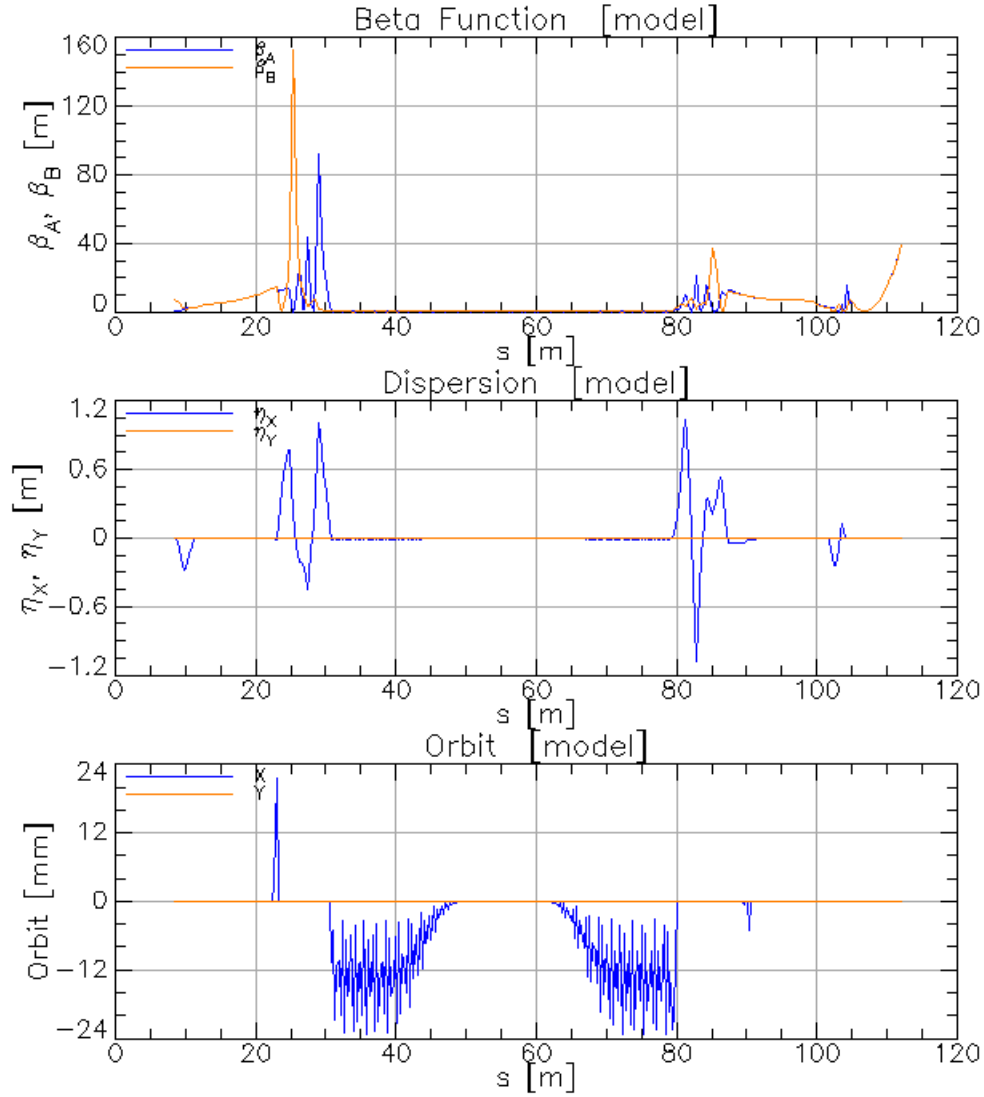


Figure 25: Simulated Bmad lattice function plots for the single pass operation of CBETA. Top: The  $\beta$  function plots for the single pass lattice. It can be seen that after the linac 10-20m there is a slow rise to  $\beta_B = 15$  m. The beam then enters the S1 splitter in which there are large peaks up to  $\beta_B \approx 160$  m. Within the FFAG return loop the  $\beta$  functions are small at a maximum of 0.4 m [17]. Again, peaks are visible in the R1 splitter/recombiner with  $\beta_B^{max} \approx 40$  m. The  $\beta$  function are then at a steady value of  $\beta < 10$  m whilst decelerated in the linac and are then passed to the dump. Middle: The dispersion functions  $\eta_{x,y}$  follow a similar pattern to the  $\beta$  functions. The dispersion is small throughout the lattice except in the splitter regions S1 and R1. Bottom: The orbit plot for the single pass CBETA lattice. This shows the characteristic behaviour of the FFAG arcs, as seen in the 30-40 m section the beam is offset with respect to the reference orbit and also oscillates around this  $\approx 12$  mm offset. From 40 m onward the beam enters the transition section (TA) in which the oscillatory behaviour is damped and the  $x$  trajectory is returned to the reference trajectory. This is mirrored through the TB transition and FB arc after the ZA, ZB FFAG straight.

There are several characteristic features of the  $\beta$  function,  $\eta_{x,y}$  and orbit plots shown in Figure 25. The  $\beta$  functions and dispersion  $\eta_x$  are typically peaked in the splitters and therefore even in multi-pass plots of lattice functions these stand out. The orbit plot meanwhile shows the orbit offset typical of the FFAG arcs and their oscillatory behaviour. The purpose of the transition sections is clear in Figure 25, they damp the oscillations in the arc and match the orbit to the reference orbit.

## 5.6 4-pass Operation

The 4-pass operation of CBETA is the optimum operational mode for CBETA, the design operation. This involves 8 passes of the linac by the beam making use of each splitter line and the 4 unique orbits in the FFAG return loop. The linac is traversed a total of 8 times with  $\pm 36$  MeV energy gain by the electron beam per pass.

In 4-pass operation the beam is injected at 6 MeV, passes through the linac exiting with an energy of 42 MeV. The beam is then recirculated through the return loop and passed into the linac with an accelerating phase as S1 and R1 are in accelerating configurations. The same beam is accelerated again on the 2nd linac pass to 78 MeV. It again traverses the return loop and S2, R2 which are in accelerating phase then it is passed into the linac again. This is repeated on the third pass where the beam exits the linac with 114 MeV. The beam is accelerated to 150 MeV on the subsequent pass of the linac however now S4 and R4 are designed in a decelerating configuration. This means after passing the splitter S4 and recombiner R4 and traversing the return loop the beam is  $180^\circ$  out of phase with the accelerating phase of the RF cavities and is decelerated.

The beam exits the linac at 114 MeV. However it's phase has changed by  $180^\circ$ . Since the accelerating configurations of the splitters and recombiners (S1-3, R1-3) mean the return loop is of integer RF wavelengths this won't change the phase of the beam - it will remain in the decelerating phase. Therefore, the beam is recirculated a further 3 times and is decelerated by 36 MeV per linac pass. Upon the final pass of the linac the beam is energy recovered once more from 42 MeV to 6 MeV. It is now directed into the dump line.

The plots of the lattice functions and orbit for the 4-pass operation of CBETA are shown in Figure 26. These plots are made in Tao from the 4-pass CBETA lattice constructed in Bmad.

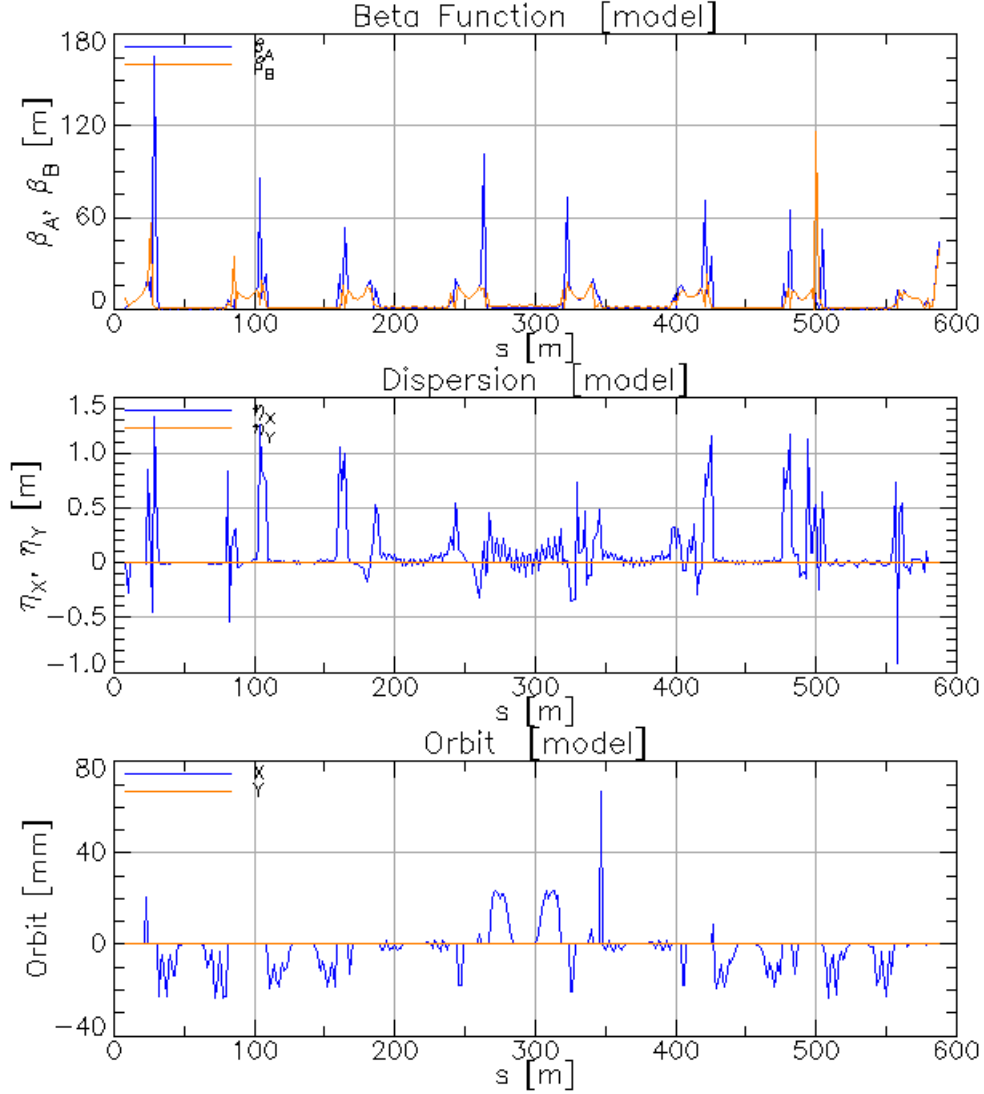


Figure 26: Bmad simulated CBETA 4-pass lattice function plots. The plots can be navigated by looking at the peaked sections. For example in the top  $\beta_{A,B}$  function plot there is a tall spike which is the S1 section then a flat section - the return loop - then another peak which is R1, a short slightly elevated section ( $\approx 97$ -108 m) which is the 2nd pass through the linac then S2 the large peaked section etc. This can be corresponded with the dispersion plot where peaks are also the splitter/recombiners S1-4, R1-4 (left to right). Top:  $\beta$  function plots of the 4-pass lattice. The splitter peaks are largest for the S1 splitter line (first peak and  $\approx 500$  m peak) and the  $\beta$  functions in the return loop increase in size at higher energy. For example, the  $\beta$  function oscillations are visible for the 4th pass return loop ( $\approx 270$ -320 m) compared to those on the 1st pass ( $\approx 20$ -70 m). Middle: Dispersion plots of the 4-pass lattice. The dispersion  $\eta_x$  is clearly spiked at the splitter/recombiner sections. The dispersion  $\eta_x$  increases in the return loop with the energy of the pass. For example, the maximum dispersion on the 4th pass return loop ( $\approx 270$ -320 m) is around 0.3 m compared to the 1st pass return loop ( $\approx 20$ -70 m) which is much smaller. Bottom: The  $x$  and  $y$  orbits offsets (from the reference orbit) of the beam. The return arcs here are the two symmetrical peaks that are either positive or negative. The straight is the section with no orbit excursion as the transition sections bring the beam to the reference orbit. The peaks for the 1st pass arcs have the largest negative orbit excursion. The orbit excursion reduced for passes 2 and 3 of the return arcs. The third pass is almost on the reference orbit. The 4th pass is the only positive  $x$  orbit excursion. This shows how the position of the beam in the FFAG arc changes with energy.

## 6 Inverse Compton Scattering Theory

### 6.1 Inverse Compton Scattering

Inverse Compton scattering is the process in which a photon, typically from a laser, is scattered to higher energy by a relativistic particle. This occurs as the photon is doubly Doppler shifted in its interaction with the relativistic particle, typically electrons. The process, unlike in Thomson scattering, is inelastic and therefore there is some recoil of the relativistic particle. Within this report only inverse Compton scattering from electrons is considered. The diagrams below in Figures 27 and 28 show inverse Compton scattering in both the head-on and crossing angle collision geometry.

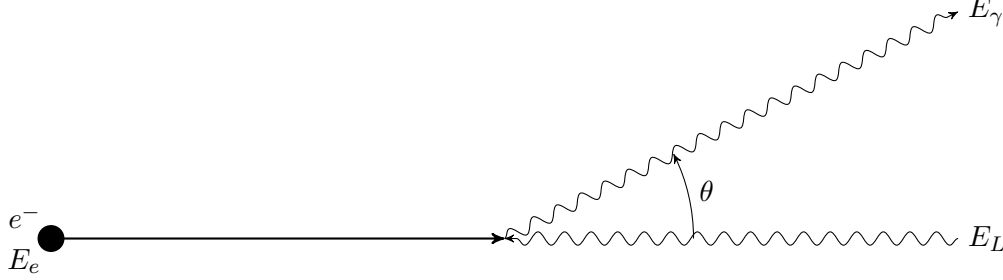


Figure 27: A diagram of inverse Compton scattering in the head-on collision geometry. The incoming electron  $e^-$  with relativistic energy  $E_e$  is interacted with an incoming head-on (crossing angle  $\phi = 0$ ) photon with an energy  $E_L$ . The incoming photon is double Doppler shifted through this interaction and is output at an observation angle  $\theta$  with an increased energy  $E_\gamma$ .

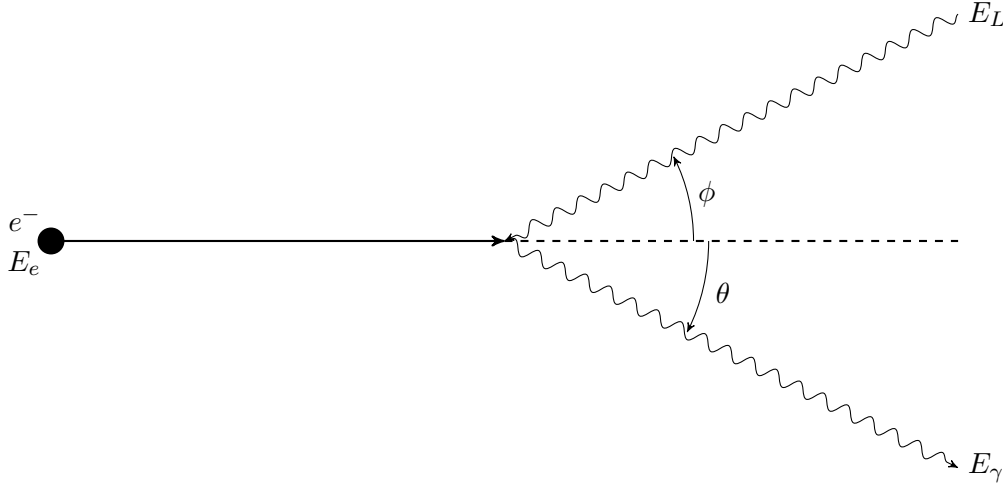


Figure 28: A diagram of the crossing angle collision geometry for inverse Compton scattering with a relativistic electron. Here an incoming electron  $e^-$  with relativistic energy  $E_e$  is interacted with an incident photon at a crossing angle  $\phi$  with some energy  $E_L$ . The incoming photon is inverse Compton scattered from the relativistic electron, resulting in a double Doppler boost which increases the energy of the electron to  $E_\gamma$ . This higher energy photon  $E_\gamma$  is then scattered at some observation angle  $\theta$ .

In the inverse Compton scattering interaction we assume an incoming photon of frequency  $f$  is incident upon a relativistic electron ( $\gamma > 1$ ) in the crossing angle geometry, as shown in Figure 28. With the electron moving relativistically we must perform a Lorentz transformation of the photon frequency  $f$  into the photon frequency in the electron reference frame  $f'$ . This is given by the usual Doppler shift formula

$$\frac{f'}{f} = \gamma (1 + \beta \cos \phi), \quad (5)$$

where  $\beta$  is the Lorentz speed factor for the electron and  $\phi$  is the crossing angle. For the ultra-relativistic case ( $\beta \approx 1$ ) with a small incident crossing angle  $\phi$ , this reduces to

$$f' \approx 2\gamma f. \quad (6)$$

Another Doppler shift is then required to return the Doppler boosted photon frequency to the laboratory frame. Therefore the relationship between the incident photon frequency  $f_i$  and the output photon frequency  $f_f$  becomes

$$f_f \approx 2\gamma^2 (1 + \beta \cos \phi) f_i. \quad (7)$$

Again, we can apply the approximation that  $\phi$  is small and the electron beam is ultra-relativistic ( $\beta \approx 1$ ). The equation can also be recast in the form of energy using the quantisation of energy  $E = hf$  through use of Planck's constant  $h$  which gives the relation

$$E_\gamma \approx 4\gamma^2 E_L, \quad (8)$$

where  $E_\gamma$  is the scattered output photon energy and  $E_L$  is the incident photon energy. This equation has not taken the recoil of the electron into account and also, as the observation angle is taken to be in the same direction as the beam, has not predicted the angular variation of the output photon. It is therefore an incomplete analysis of the scattering and is valid for the peak energy produced from relativistic Thomson scattering. It is used to show how the double Doppler shift  $4\gamma^2$  term arises. A more rigorous analysis of this scattering process yields

$$E_\gamma \approx \frac{4\gamma^2 E_L}{1 + (\gamma\theta)^2 + X}, \quad (9)$$

where  $\theta$  is the observation angle of the scattered photon and  $X$  is the recoil parameter, a parameter designed to take into account the recoil of the electron from the inelastic collision. The recoil parameter  $X$  is given by

$$X = \frac{4\gamma E_L}{m_e c^2}, \quad (10)$$

where  $m_e$  is the mass of the electron and  $c$  is the speed of light. Notice that (10) has a  $\gamma$  term and not a  $\gamma^2$  term as this is only Doppler shifted a single time from the electron rest frame to the lab frame when the recoil occurs.

Some of the inverse Compton scattering sources that are investigated or that have their designs presented here use re-circulating laser cavities. These are devices that are designed to circulate and use the same laser pulse for multiple interactions with different electron bunches. Typically these consist of an arrangement of mirrors designed in such a geometry that the laser pulse is recirculated. Energy losses occur due to the imperfect reflectivity of the mirrors and the output flux of the scattered photons. An interaction point where the laser pulse interacts with the electron beam is constructed at some point within the laser path in these cavities. An example of a laser recirculation cavity, the bow-tie geometry cavity used at the cERL ICS [6], is shown in Figure 29.

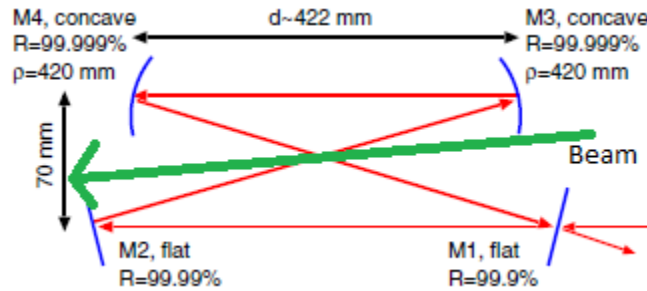


Figure 29: The cERL ICS bow-tie laser recirculation cavity [6]. The laser pulse is in-putted through the lowest reflectivity mirror and recirculated between the 4 mirror system in a bow-tie shaped path using two flat and two concave mirrors. The beam is interacted with the laser in the central path crossing of this cavity where the laser waist size is minimal.

The cavity geometry shown in Figure 29 is the geometry adopted for the laser recirculation cavity used in all of the inverse Compton scattering source design undertaken here. The benefit of laser recirculation cavities is twofold: it allows an increase in repetition rate of collisions from the kHz range in which the laser system operates to the 100's MHz to GHz, the laser waist can also be reduced further which can increase the flux of

scattered photons. A full investigation or explanation of laser cavities is not included in this report, this will be the subject of future work and investigation.

In order to achieve a quasi-monochromatic source from inverse Compton scattering the source can be collimated to select the peak of the spectrum. The high-flux, peak energy part of the spectrum is selected in a narrow bandwidth to provide this quasi-narrowband source. Using cERL as an example, the impact of collimation on the inverse Compton scattering spectrum is shown in Figure 30.

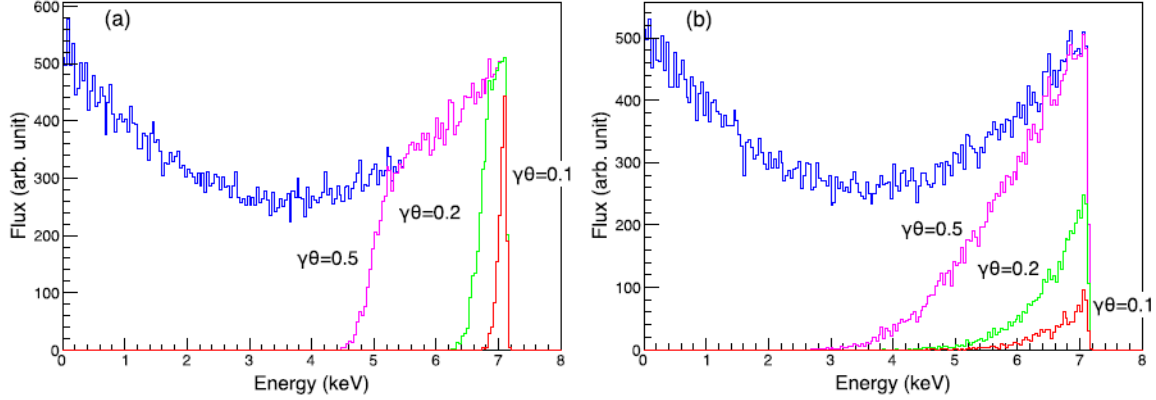


Figure 30: The simulated spectrum of the cERL X-ray inverse Compton scattering source [6]. These are produced through simulating a 1064 nm Nd:YAG laser inverse Compton scattered from a 20 MeV electron beam. Left: The cERL source with a normalised emittance  $\varepsilon_n = 1$  mm mrad. Right: The cERL source with a normalised emittance  $\varepsilon_n = 5$  mm mrad. The sources are collimated with  $\Psi = \gamma\theta = 0.1$  (red), 0.2 (green), 0.5 (purple) where  $\theta$  is the observation angle and  $\Psi$  the collimation angle. This shows the shape of the spectra when collimated. Comparing the left ( $\varepsilon_n = 1$  mm mrad) plot with the right ( $\varepsilon_n = 5$  mm mrad) plot shows the necessity of a small emittance on a well collimated quasi-monoenergetic source.

Sources can be designed to provide quasi-monoenergetic radiation within a small bandwidth with small divergence and angular spread. This typically requires strong collimation, small emittance and small laser and beam energy spread.

## 6.2 Inverse Compton Scattering Regimes

Within the inverse Compton scattering process there are two main regimes, the recoil regime and the non-linear regime, in which effects arise that alter the output spectrum of the scattered photons. These effects range from a reduction in the flux of the inverse Compton source, to increased bandwidth and reduced peak energy.

As previously mentioned, the definition between relativistic Thomson scattering and inverse Compton scattering is that inverse Compton scattering models this interaction as an inelastic collision and therefore there is electron recoil. To characterise this the recoil parameter  $X$ , as defined in (10), was introduced. The use of the recoil parameter can be extended to categorise whether a source is Thomson-like i.e the recoil is negligible or whether the recoil significantly affects the output spectrum. The criterion for a source to be Thomson-like is

$$X \ll 1. \quad (11)$$

This can also be stated as  $\gamma hf \ll m_e c^2$  where  $h$  is Planck's constant and  $f$  is the frequency of the incident radiation. When this criterion is exceeded and no longer applies the inverse Compton scattering source is termed to be in the recoil regime. We can see from the recoil parameter (10) that the source can exceed the criterion from either having a high beam energy and consequently a large Lorentz factor  $\gamma$  or through a high incoming photon energy  $E_L$  such as that provided by a free electron laser or other light source.

The effects of the recoil regime are that the energy of the scattered photon is reduced in comparison to the Thomson picture and therefore the whole spectrum is shifted to lower energy in relation to the Thomson picture. The cross section is also reduced from the Thomson cross section  $\sigma_T$ . These effects are shown explicitly in Section 6.3.

The non-linear regime is defined based on the field strength of the normalised vector potential of the laser  $a_0$ . This is a parameter first defined and used in laser plasma wakefield acceleration (LPWA). The normalised laser vector potential  $\mathbf{a}$  is given by



$$\mathbf{a} = \frac{e\mathbf{A}}{m_e c^2}, \quad (12)$$

where  $e$  is the elementary charge constant and  $\mathbf{A}$  is the vector potential. The associated field strength parameters  $a_0$  is given by

$$a_0 = \frac{eE_0\lambda}{2\pi m_e c^2} \approx 0.85 \times 10^{-9} \lambda[\mu m] \sqrt{I[W/cm^2]}, \quad (13)$$

where  $\lambda$  is the wavelength of the incident photon,  $E_0$  is the maximum field strength of the incident laser electric field and  $I$  is the intensity of the incident laser pulse. If this associated field strength  $a_0$  is much less than unity then the inverse Compton source is termed linear i.e

$$a_0 \ll 1. \quad (14)$$

The criterion (14) along with the definition of  $a_0$  (13) shows that when the laser reaches a certain field strength or intensity the electric field of the laser pulse starts to affect the output spectrum of the inverse Compton interaction. Whereas below this criterion the effect of the electric field of the laser was negligible.

The non-linear regime affects the output photon spectrum in a multitude of ways such as the ponderomotive broadening of the spectrum, causing an increase in bandwidth and decrease in spectral energy density, harmonic generation which can lead to higher energy radiation production and multi-photon inverse Compton scattering ( $a_0 > 1$ ) which allows the creation of very high energy output photons beyond the double Doppler boosted energy. These effects are explained in much greater detail in Section 6.4.

### 6.3 Recoil Regime

As aforementioned in Section 6.2, the recoil regime is entered for sources at high photon or, more commonly, high beam energies. The two notable affect of a non-negligible recoil parameter  $X$  on the source is to shift the energy of the source slightly from what would be expected in Thomson scattering. The recoil parameter also affects the cross section; a higher recoil parameter gives a small Compton cross section  $\sigma_c$ .

The reduction in energy across the spectrum can be seen from the peak energy equation (9)

$$E_\gamma \approx \frac{4\gamma^2 E_L}{1 + (\gamma\theta)^2 + X},$$

the  $1/X$  contribution is clearly the origin of the shift. A good example of this effect can be seen in Figure 31, this shows a plot of the simulated Thomson scattering spectrum and simulated inverse Compton scattering spectrum for the ELI-NP-GBS  $\gamma$ -ray ICS [7].

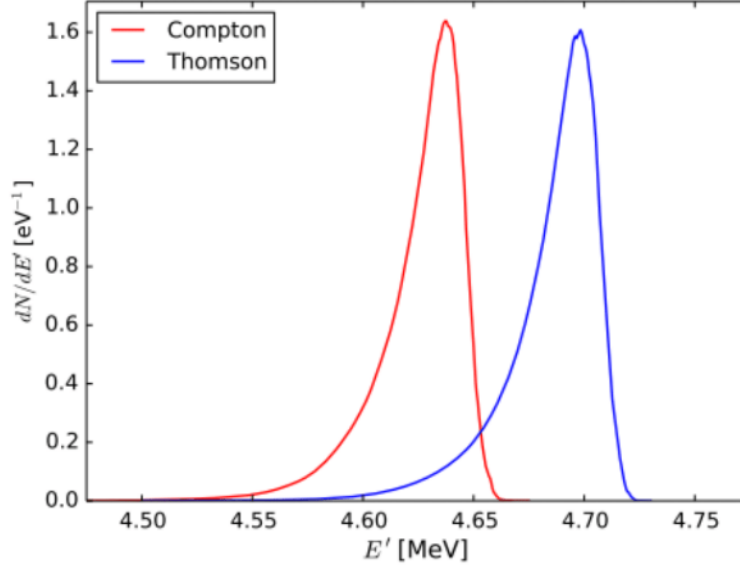


Figure 31: A plot of the normalised counts per unit energy (eV) against the scattered photon energy for the ELI-NP ICS [68]. This plot was simulated using 10,000 particles. This shows the effect of recoil which is taken into account for the inverse Compton scattering (red) case compared to the Thomson scattering (blue) case where recoil isn't taken into account. The parameters of the ELI-NP machine in this case are  $E_e = 360$  MeV,  $\lambda = 523$  nm giving a recoil parameter of  $X = 0.013$ . Therefore, the figure shows the change in spectra for a relatively modest recoil.

The other effect of the recoil regime is the variation it causes in the Compton cross section  $\sigma_c$ , this typically becomes lower than the Thomson cross section  $\sigma_T$  given by

$$\sigma_T = \frac{e^4}{6\pi\epsilon_0 m_e^2 c^4} = 6.65 \times 10^{-29} \text{ m}^2 = 0.665 \text{ barns}, \quad (15)$$

with  $e$  the elementary charge constant and  $\epsilon_0$  the permittivity of free space. The analytical formula for the Compton cross section as shown by L. Serafini et al [69] is

$$\sigma_c = \sigma_T \frac{3}{4X} \left[ \left( 1 - \frac{4}{X} - \frac{8}{X^2} \right) \log(1+X) + \frac{1}{2} + \frac{8}{X} - \frac{1}{2(1+X)^2} \right], \quad (16)$$

where  $\sigma_T$  is the Thomson cross section as in (15) and  $X$  is the recoil parameter. The actual effect of recoil on the cross section is difficult to perceive from the full analytical formula (16) therefore limits can be taken to clarify this. When the recoil parameter is small i.e  $X \rightarrow 0$  the cross section becomes

$$\lim_{X \rightarrow 0} \sigma_c = \sigma_T (1 - X). \quad (17)$$

Similarly, when recoil becomes very large  $X \rightarrow \infty$  the cross section becomes

$$\lim_{X \rightarrow \infty} \sigma_c = \sigma_T \left( \frac{3}{4X} \left[ \log X + \frac{1}{2} \right] \right). \quad (18)$$

As can be observed from (17) the recoil parameter, when small, causes a slight reduction in the cross section and therefore the flux produced from the ICS. The effect on the cross section increases as the recoil parameter increases in size as evident from (18). To summarise, a complete treatment of recoil is required to properly account for the inverse Compton scattered wavelength and obtain the correct energy for the scattered photons [68]. Equations (17) and (18) also show that including recoil is necessary to obtain the correct values for the flux and therefore this is required for a proper treatment of other spectral parameters such as the spectral brilliance and spectral energy density.

## 6.4 Non-linear Regime

Previously it was stated in Section 6.2 that the process of inverse Compton scattering becomes non-linear when the criterion  $a_0 \ll 1$  is exceeded. This leads to the non-linear effects of ponderomotive spectral broadening, harmonic generation and multi-photon inverse Compton scattering which are explained in this section.

Multi-photon inverse Compton scattering is a process in which two photons from the laser pulse interact with a single electron to produce a single photon with energy higher than the typical factor of  $4\gamma^2$  increase from equation (9). A diagram of this process is shown in Figure 32.

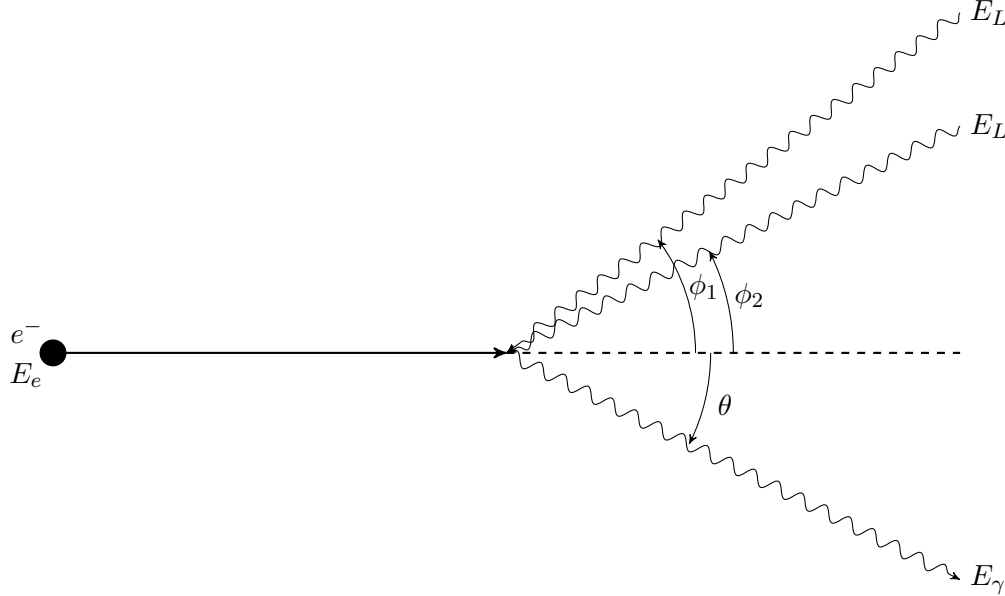


Figure 32: A diagram of a multi-photon inverse Compton scattering interaction. Here two incident photons from varying angles  $\phi_1$  and  $\phi_2$  are incident with energy  $E_L$  onto a relativistic electron of energy  $E_e$ . The two photons are double Doppler boosted and then are emitted as a single photon of increased energy  $E_\gamma$ .

However, this multi-photon process can only occur for  $a_0 > 1$ . To achieve  $a_0 = 1$  requires a very large laser power. For example, with an Nd:YAG laser,  $\lambda=1064\text{nm}$  and working backward from (13) shows that a laser intensity of  $1.38 \times 10^{22} \text{ W/m}^2$  is required to achieve  $a_0 = 1$ . Taking a conservative estimate at the beam spot size  $\sigma_L$  of  $50 \mu\text{m}$  and using an equation to relate the intensity  $I$  to the laser power  $P_L$

$$I = \frac{P_L}{4\pi^2\sigma_L^2}, \quad (19)$$

we can see that a 1.36 PW peak power laser would need to be used to reach the multi-photon inverse Compton scattering threshold. This would be a peak power of 0.68 PW for the 2nd harmonic of a Ti:Sa laser at  $\lambda = 532 \text{ nm}$ . Consequently, multi-photon inverse Compton scattering is not a process that will be observed in any planned or constructed ICS to date.

Harmonic generation is a process in which there is a contribution to the output inverse Compton scattering spectrum from the 2nd, 3rd etc. harmonic of the incident laser and therefore higher energy radiation is produced. The relative importance of these higher-order harmonics increases with  $a_0$ , from being negligible at  $a_0 < 0.5$  to rivalling the primary harmonic at  $a_0 \approx 1$  [70]. Therefore, harmonic generation can be a useful process for creating higher energy radiation, for example  $\gamma$ -rays at a lower beam energy. However, it can be disruptive as emitted ICS radiation collimated at a particular angle could include radiation produced from both the primary harmonic and secondary harmonic such that it is no longer quasi-monochromatic.

Another non-linear effect that arises when  $a_0 \ll 1$  no longer applies is ponderomotive spectral broadening. This is where the components of the electric  $\vec{E}$  and magnetic  $\vec{B}$  fields of the laser, which have a transverse component, create a transverse ponderomotive force at the point of interaction. Subsequently, there is a transverse spread in the output radiation which increases the bandwidth. When this effect is applied to the interaction of a photon and electron beam the transverse spreading can lead to the creation of multiple secondary peaks, due

to the interference between wave trains emitted from different positions within the laser pulse [71]. Figure 33 illustrates the effect of ponderomotive spectral broadening at different values of  $a_0$ .

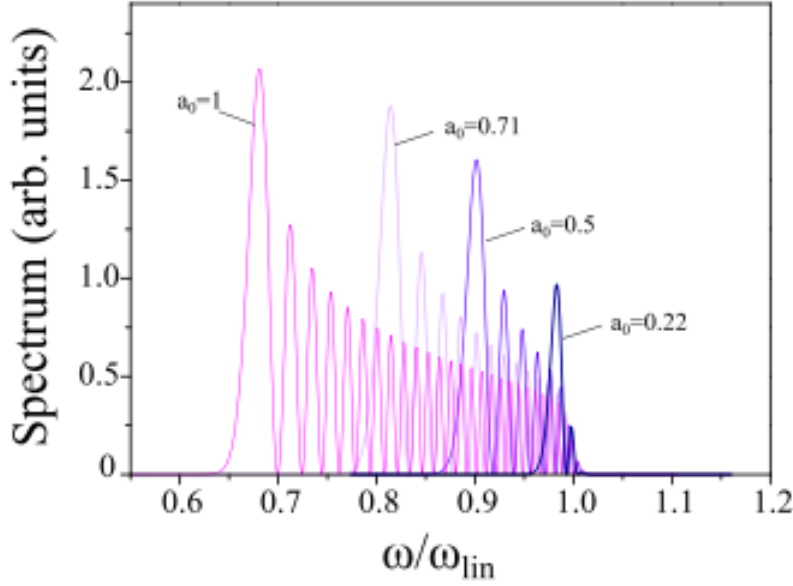


Figure 33: A plot of the spectrum i.e normalised flux of the source against the frequency divided by the peak frequency as produced by V. Petrillo et al [71]. The spectra are plotted for a series of  $a_0$  values  $a_0 = 0.22$  ( $E_{pulse} = 0.1$  J),  $a_0 = 0.5$  ( $E_{pulse} = 0.5$  J),  $a_0 = 0.71$  ( $E_{pulse} = 1$  J),  $a_0 = 1$  ( $E_{pulse} = 2$  J). The beam energy is constant at 30.6 MeV ( $\gamma = 60$ ). The plot shows the series of secondary peaks that are created in the spectrum by ponderomotive broadening. It is also clear to see that this effect increases the spectral width i.e the bandwidth of source.

## 6.5 Spectra Calculations

In addition to the calculation of the energy of the output photon from inverse Compton scattering in (9), many other spectral parameters of the source can be calculated. Within this section the spectral parameters used in the literature to describe and compare ICS, which are also used to characterise the output of the designed sources in this report, are stated and explained here.

The number of photons  $N_\gamma$  produced for a single head-on, as shown in Figure 27, inverse Compton scattering interaction between a laser pulse and electron bunch is given by

$$N_\gamma = \sigma_c L = \sigma_c \frac{N_e N_L}{2\pi\sigma_x\sigma_y}, \quad (20)$$

where  $\sigma_c$  is the Compton cross section (16),  $L$  is the luminosity of the source  $N_e$  is the number of electrons in the bunch,  $N_L$  is the number of photons in the bunch and  $\sigma_{x/y}$  is the transverse rms convoluted spot size of the laser pulse and electron bunch in the interaction i.e the inverse Compton radiation source size. The convoluted rms spot size is the parameter that defines the rms size of the crossing between the two Gaussian beams. The assumption of Gaussian beams is the reason for the  $2\pi$  factor in the denominator. The convoluted rms spot size is given by

$$\sigma_{x/y} = \sqrt{\sigma_{e,x/y}^2 + \sigma_{L,x/y}^2}, \quad (21)$$

where  $\sigma_{L,x/y}$  is the rms spot size of the laser and  $\sigma_{e,x/y}$  is the rms spot size of the beam as given by

$$\sigma_{e,x/y} = \sqrt{\frac{\beta^* \varepsilon_{n,x/y}}{\gamma}}, \quad (22)$$

with  $\beta^*$  the beta function at the point where the laser pulse and electron bunch are interacted and  $\varepsilon_{n,x/y}$  the normalised emittance of the beam in either plane.

The number of photons produced in a single shot is often termed the flux per shot where a shot is a single interaction of a laser pulse and electron beam. A quantity that is most often used is the number of photons produced from an inverse Compton source per second - the flux  $F$ . In the head-on case the flux is given by

$$F = \sigma_c f L = \sigma_c \frac{f N_e N_L}{2\pi\sigma_x\sigma_y}, \quad (23)$$

where  $f$  is the repetition rate, the rate of inverse Compton interactions.

In inverse Compton scattering sources the collision geometry is not necessarily head-on, for example a recirculating laser ICS is typically collided at some crossing angle  $\phi$  in one plane as shown in Figure 28. The luminosity in this configuration is therefore modified as the geometry of the interaction has changed. Since the luminosity is modified, the flux in this case is subsequently altered to the angular flux presented by T.Akagi et al [6]

$$F = \sigma_c \frac{f N_e N_L \cos(\phi/2)}{2\pi\sigma_y \sqrt{\sigma_x^2 \cos^2(\phi/2) + \sigma_z^2 \sin^2(\phi/2)}}, \quad (24)$$

with a crossing angle  $\phi$  and  $\sigma_z$  the longitudinal rms convolution of the electron bunch length and laser pulse length given as

$$\sigma_z = \sqrt{\sigma_{e,z}^2 + (c\tau_{pulse})^2}, \quad (25)$$

where  $\sigma_{e,z}$  is the rms electron bunch length and  $\tau_{pulse}$  is the laser pulse duration.

Within some light source calculations values are typically quoted within 0.1% bandwidth, the peak-energy mono-energetic part of the spectrum, in order to compare the quality of light sources for users whom historically have favoured this part of the spectrum. For an inverse Compton scattering source the flux inside a 0.1% bandwidth (bw) can easily be calculated using the relation by Krafft et al [72]

$$F_{0.1\%} = 1.5 \times 10^{-3} F. \quad (26)$$

The flux can also be calculated for a given observation angle  $\theta$ . This follows the prescription by L. Serafini et al [69] where the flux  $F_\Psi$  at a particular observation angle  $\theta$  is given by

$$F_\Psi = 6.25 \times 10^8 \frac{E_{pulse}[J] Q[pC] f[Hz]}{E_L[eV] \sigma_x[\mu m] \sigma_y[\mu m]} \times \frac{(1 + \sqrt[3]{X} \Psi^2/3) \Psi^2}{[1 + (1 + X/2) \Psi^2] (1 + \Psi^2)} = F \times \frac{(1 + \sqrt[3]{X} \Psi^2/3) \Psi^2}{[1 + (1 + X/2) \Psi^2] (1 + \Psi^2)}, \quad (27)$$

with  $E_{pulse}$  the energy of the laser pulse,  $Q$  the bunch charge,  $f$  the repetition rate,  $E_L$  the incident photon energy,  $\sigma_{x/y}$  the convoluted transverse spot size of the laser pulse and electron bunch,  $X$  the recoil parameter and the collimation angle  $\Psi = \gamma\theta$  with  $\theta$  the observation angle.

Another parameter that is calculated for ICS is the average spectral brilliance. This parameter is often calculated for a 0.1% bandwidth for light source comparison. The average spectral brilliance is a measure of the flux per unit phase space area. Therefore, it is used to compare the quality of a source of radiation as it is a measure of the flux per transverse size of the interaction i.e the source size. This is given by

$$B_{0.1\%}^{avg} = \frac{\gamma^2 F_{0.1\%}}{4\pi^2 \varepsilon_{n,x} \varepsilon_{n,y}}, \quad (28)$$

where  $\varepsilon_{n,x/y}$  is the normalised emittance in that plane and  $F_{0.1\%}$  is the flux in 0.1% bandwidth 26. The  $\gamma^2$  term in this equation originates as the normalised emittance is used in (28). This parameter is often used on recirculating inverse Compton sources such as those on ERLs or storage rings. However, for conventional linacs the peak brilliance is often favoured, this can be calculated using

$$B_{0.1\%}^{peak} = 1.5 \times 10^{-3} \frac{\gamma^2 N_\gamma}{4\pi^2 \varepsilon_{n,x} \varepsilon_{n,y} \tau_{pulse}}, \quad (29)$$

where  $\tau_{pulse}$  is the laser pulse duration and  $N_\gamma$  is the flux per shot. The  $1.5 \times 10^{-3}$  factor arises from the scaling to a 0.1% bandwidth as in (26). The peak brilliance is therefore the brilliance of the output spectra over the duration of a single pulse interaction.

In order to describe the mono-chromaticity of the spectral output the bandwidth  $\frac{\Delta E_x}{E_x}$  is defined. This is the energy spread within the output radiation. A study has been performed into the bandwidth in much greater detail as presented in Section 6.6. The purpose of this was to select the appropriate bandwidth equation from the literature and evaluate the options. The chosen bandwidth equation by G.Krafft et al [73] is given as

$$\frac{\Delta E_x}{E_x} = \sqrt{\left(\frac{\sigma_\theta}{E_\theta}\right)^2 + \left(\frac{\sigma_e}{E_e}\right)^2 + \left(\frac{\sigma_L}{E_L}\right)^2 + \left(\frac{\sigma_\varepsilon}{E_\varepsilon}\right)^2}, \quad (30)$$

where the first term is the collimation term (31), the second term is the beam energy spread term (32), the third term is the laser energy spread term (33) and the final term is the emittance term (34). These terms are given by

$$\frac{\sigma_\theta}{E_\theta} = \frac{1}{\sqrt{12}} \frac{\Psi^2}{1 + X + \Psi^2/2}, \quad (31)$$

$$\frac{\sigma_e}{E_e} = \frac{2 + X}{1 + X + \Psi^2} \frac{\Delta E_e}{E_e}, \quad (32)$$

$$\frac{\sigma_L}{E_L} = \frac{1 + \Psi^2}{1 + X + \Psi^2} \frac{\Delta E_L}{E_L}, \quad (33)$$

$$\frac{\sigma_\varepsilon}{E_\varepsilon} = \frac{2\gamma\epsilon_n}{\beta^*}. \quad (34)$$

Where  $X$  is the recoil parameter,  $\Psi$  is the collimation angle  $\Psi = \gamma\theta$  where  $\theta$  is the observation angle,  $\frac{\Delta E_e}{E_e}$  is the energy spread of the electron beam,  $\frac{\Delta E_L}{E_L}$  is the laser energy spread,  $\epsilon_n$  is the normalised emittance and  $\beta^*$  is the beta function at the inverse Compton scattering interaction point.

In addition, the spectral energy density  $S$  can be calculated. This parameter, along with the bandwidth, describes the shape of the spectrum. A high spectral energy density is intrinsic to a strongly peaked spectrum. The spectral energy density, following the calculation from L. Serafini et al [69], is calculated via

$$S = \frac{F}{4\sqrt{2\pi}\gamma^2 E_L \frac{\Delta E_x}{E_x}}, \quad (35)$$

where  $F$  is the flux and  $\frac{\Delta E_x}{E_x}$  is the bandwidth of the source and  $E_L$  is the incident photon energy.

## 6.6 Bandwidth Investigation

In order to calculate the bandwidth for inverse Compton sources there are many possible options in the literature. Formulae have been specified that take into account specific Compton scattering regimes, as explained in Section 6.2, namely the non-linear and recoil regimes, which build upon the simple Thomson scattering prescription. This enables the bandwidth to correctly take account of the effects these cause such as ponderomotive broadening, harmonic generation and the energy shifting from recoil.

For the purpose of of this discussion we look at three bandwidth formula as specified in equations (36), (37) and (39). These are the works of T. Akagi et al [6] (36), L. Serafini et al [69](37) and G. A. Krafft et al [73] (30) respectively.

Firstly the formula of T. Akagi et al is shown below

$$\frac{\Delta E_x}{E_x} = \sqrt{(\gamma\theta)^4 + 4\left(\frac{\Delta E_e}{E_e}\right)^2 + \left(\frac{\epsilon_n}{\sigma_e}\right)^4 + \left(\frac{\Delta\nu}{\nu}\right)^2 + \left(\frac{M^2\lambda}{4\pi\sigma_L}\right)^4}, \quad (36)$$

where the first term is a collimation term, the second a beam energy spread term, third an emittance term, fourth a laser energy term and finally a beam quality term. Here  $\theta$  is the observation angle,  $E_e$  is the electron beam energy,  $\epsilon_n$  the normalised emittance,  $\sigma_e$  is the energy spread of the beam,  $\nu$  is the incident photon frequency,  $M$  is the laser quality parameter, which determines how Gaussian the pulse is ( $M^2 = 1$  is perfectly Gaussian),  $\sigma_L$  is the spot size of the laser pulse and  $\lambda$  is the wavelength of the laser.

The bandwidth formula presented by L. Serafini et al is given by

$$\frac{\Delta E_x}{E_x} = \sqrt{\left[\frac{\Psi^2}{\sqrt{12}(1+\Psi^2)} + \frac{\tilde{P}^2}{1+\sqrt{12}\tilde{P}}\right]^2 + \left[\left(\frac{2+X}{1+X}\right)\frac{\Delta\gamma}{\gamma}\right]^2 + \left(\frac{1}{1+X}\frac{\Delta E_L}{E_L}\right)^2 + \left(\frac{M^2\lambda}{4\pi\sigma_L}\right)^4 + \left(\frac{a_0^2/2}{1+a_0^2/2}\right)^2}, \quad (37)$$

with  $\Psi = \gamma\theta$  is termed the collimation angle where  $\theta$  the observation angle,  $E_L$  is the incident photon energy and  $\tilde{P}$  is the electron normalised transverse momentum given by

$$\tilde{P} = \frac{\sqrt{2}\epsilon_n}{\sigma_x\sqrt{1+X}}, \quad (38)$$

with  $\epsilon_n$  the normalised emittance and  $\sigma_x$  the convolution of the electron bunch and laser pulse transverse spot size in the  $x$  plane. The first term here is a convolution between the collimation and emittance term, the second

term is a beam energy spread term, the third a laser energy term, the fourth a laser beam quality term and finally a non-linear ponderomotive broadening term.

Finally, there is the bandwidth formula by G.A. Krafft et al which is given by

$$\frac{\Delta E_x}{E_x} = \sqrt{\left(\frac{\sigma_\theta}{E_\theta}\right)^2 + \left(\frac{\sigma_e}{E_e}\right)^2 + \left(\frac{\sigma_L}{E_L}\right)^2 + \left(\frac{\sigma_\epsilon}{E_\epsilon}\right)^2}, \quad (39)$$

where the first term is the collimation term, the second the beam energy spread term, the third the laser energy spread term and finally the emittance term. The individual terms (31), (32), (33), (33) are defined in Section 6.5 so won't be reiterated here.

The three bandwidth derivations shown above are all composed of a collimation term, laser and beam energy spread term and collimation term. However, Serafini et al's equation (37) also includes a beam quality term and a ponderomotive broadening term, T. Akagi et al's prescription also includes a beam quality term.

The T. Akagi et al [6] bandwidth is the most simple construction. This equation is used directly in evaluating the experimental results of the cERL ICS at KEK. Therefore, we know it is directly applicable to ERL based ICS. The formula, unlike that by Krafft et al (39) also includes a beam quality term. The purpose of this term is to evaluate the shape of the incoming laser pulse and account for the effect of this on the bandwidth. However, this term is often very negligible in ICS as the laser wavelengths are typically atleast two orders of magnitude smaller than the spot size  $\sigma_L$  ( $\lambda \ll \sigma_L$ ), subsequently the contribution of this term is on the order of  $10^{-8}$  and is therefore negligible.

The derivation of the T. Akagi bandwidth is based on an earlier paper by L. Serafini et al (2012) [74], which has been superseded by the L. Serafini bandwidth [69] given in (37). Consequently, the T. Akagi approach is outdated. The formulation by T. Akagi et al also doesn't include a complete treatment of the laser and beam energy spread terms as equations (19), (20) are approximations in the paper on which this is based, Serafini et al (2012) [74].

The L. Serafini bandwidth (2017) in (37), which supersedes T. Akagi (36), has the advantage that it has been designed to be applicable to all of the regimes of inverse Compton scattering: the Thomson regime, non-linear regime and recoil regime. The recoil regime is taken into account through the factors including the recoil parameter  $X$  in front of the energy spread terms, it also is included within  $\tilde{P}$  (38). The non-linear effects are included through a ponderomotive broadening term, this term aims to model the broadening of the spectrum through the ponderomotive force of the laser.

On the other hand, the effect of the collimation term is convoluted with the effect of the emittance in this derivation (37), the reason for this is not apparent in the derivation in [69]. This joint emittance and collimation term also becomes more inaccurate with aperture growth [69]. As well as this, the effect of the collimation angle  $\Psi$  is neglected in both the laser and beam energy spread terms in comparison to (33), (32) in the Krafft et al treatment [73]. Within the original Serafini et al paper [69] there was also an error with the  $\sqrt{12}$  factor in the first term which has been corrected, the corrected version is shown here.

The most recent derivation investigated in the paper by Krafft et al [73] provides a clear and concise derivation based upon previous work on scaling laws for inverse Compton scattering. Consequently the formula (39) can be calculated directly from straightforward parameters unlike in L. Serafini et al's description (37) where these are more abstract;  $\tilde{P}$  the normalised transverse momentum for example. As previously mentioned, (39) also corrects the beam and laser energy spread terms through a treatment of the collimation angle  $\Psi$ .

Significantly, the formula by Krafft et al doesn't include a ponderomotive broadening term which means it is only valid in the linear  $a_0 \ll 1$  regime. Also, a laser beam quality term is omitted, however this is due to the term having a negligible contribution in common cases. As a result of these two caveats, the region of validity for this formula is for  $a_0 \ll 1$  i.e linearity and  $\lambda \ll \sigma_L$  the wavelength much smaller than the rms spot size of the laser. However, the region of validity for (39) encompasses all existing and planned inverse Compton scattering sources.

## 7 CBETA X-ray Inverse Compton Scattering Source

### 7.1 X-ray ICS Design

A part of this study has involved the design of a proposed re-circulating inverse Compton source on CBETA. This is designed as a narrow-band ( $< 1\%$  bandwidth) hard X-ray ( $E_\gamma > 10$  keV) source for applications such as high energy X-ray diffraction which requires a source of X-rays from 50 keV to 150 keV. Another application of such a high energy, high flux source is spectroscopy in high energy atomic physics [61].

This study involved looking at potential opportunities for an inverse Compton source on each pass of the 4-pass CBETA ERL. A set of straw-man parameters have been set for both the electron beam, based on conversations

with the CBETA team, and the Nd:YAG laser and cavity, based on the laser recirculation cavity in the cERL ICS [6]. The cERL ICS was chosen as a basis for the laser parameters as the cERL ICS is the current highest flux demonstration of an inverse Compton source on an ERL as shown in Section 9.1. Adapting the cERL and cavity and laser system has the advantage of the proven compatibility of the design with use on an ERL and therefore was seen as a good case study. The beam parameters were based on those provided in the CBETA design report [17] with the unknown parameters such as the  $\beta$  function at the interaction point  $\beta^*$  estimated. The straw-man parameters for the laser system and electron beam at an interaction point which utilises a bow-tie cavity and focused electron beam are shown below in Table 5 and 6.

Laser Parameter	Value
Wavelength ( $\mu\text{m}$ )	1.00
Average Stored Power in Cavity (kW)	81
Pulse Energy ( $\mu\text{J}$ )	62
Repetition Rate (GHz)	1.3
Spot size at IP ( $\mu\text{m}$ )	25
Stored Pulse Duration (ps)	5.7
Field Strength of the Normalised Laser Vector Potential $a_0$	$4.76 \times 10^{-4}$

Table 5: Initial parameters for the CBETA ICS laser recirculation cavity and laser system. These parameters are based on the cERL ICS laser cavity [6]. However, some are modified such as the repetition rate and the spot size to reflect the difference between the cERL and CBETA machines, and the improvement in ICS cavities.

Beam Parameter	Value
Beam Energy (MeV)	42, 78, 114, 150
RF Frequency (GHz)	1.3
Repetition Rate (GHz)	1.3
$\beta$ function at the IP $\beta^*$ (cm)	1
Normalised transverse rms emittance (mm-mrad)	0.3
Bunch Charge (pC)	32
rms Bunch Length (mm)	1.3
Recoil Parameter X ( $\times 10^3$ )	0.75, 1.40, 2.04, 2.69

Table 6: Target beam parameters for the CBETA ICS interaction point (IP), which is currently not designed. A potential design for a bypass and interaction point are shown in Section 7.5. The beam parameters at IP were motivated by discussions with the CBETA commissioning team and from the technical design report [17].

Upon further analysis of Tables 5 and 6, the repetition rate is beyond feasibility by around a factor of 4. This is as the 1.3 GHz repetition rate would cause a large laser intensity on the laser recirculation cavity mirrors and also the cavity would be smaller and therefore misalignment errors would be of a greater magnitude. A diagram of the bow-tie cavity as used for the cERL ICS is shown in Figure 34.



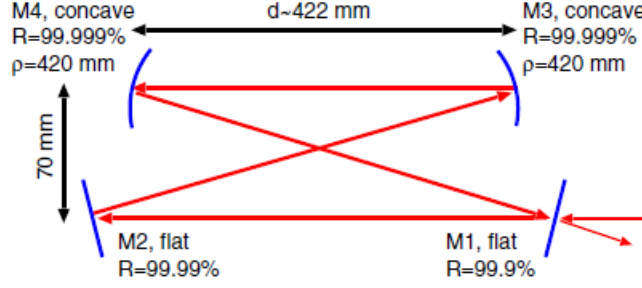


Figure 34: The bow-tie laser recirculation cavity used at the cERL ICS. This is a 4-mirror recirculation cavity in which the laser is recirculated in order to increase the repetition rate. The laser pulse electron bunch interaction occurs at the centre of the cavity.

For example, the path length  $s$  in the cavity for the cERL ICS is given by

$$s = \frac{c}{f} = \frac{3 \times 10^8}{162.5 \times 10^6} = 1.85 \text{ m}, \quad (40)$$

with  $f$  the repetition frequency and  $c$  the speed of light. Whereas, if the repetition frequency is 1.3 GHz this becomes 0.23 m. This fundamentally changes the cavity behaviour such as the spot size at the interaction point of the laser. Because of the reduction in time for a single pass of the cavity piezoelectric tuners, which vary the position of the mirrors to account for misalignments of the cavity, would not be able to operate as effectively and therefore misalignment errors are increased.

If we take the example of the cERL ICS [6] cavity with the same dimensions and increase the repetition rate to 1.3 GHz, a situation which is non-physical but illustrative, we can see the effect this has on cavity mirrors. The cavity parameters for this case are shown in Table 7.

Cavity Parameter	Value
Spot Size on Mirrors $\sigma_x/\sigma_y$ (mm)	0.7/0.6
Pulse Energy ( $\mu\text{J}$ )	62
Repetition Rate (GHz)	1.3

Table 7: Test parameters to illustrate the laser intensity on cavity mirrors for a 1.3 GHz bow-tie cavity based on the cERL ICS cavity. The spot size on mirrors and pulse energy parameters are based on those by T. Akagi et al [6].

Firstly, using the values in Table 7 we calculate the power of the laser pulse in the cavity through

$$P = E_{\text{pulse}} \times f = (62 \times 10^{-6}) \times (1.3 \times 10^9) = 80.6 \text{ kW}, \quad (41)$$

where  $P$  is the cavity power,  $E_{\text{pulse}}$  is the energy of the laser pulse and  $f$  is the repetition rate. The area  $A$  of the elliptical spot size on the mirror is calculated using the relation

$$A \approx \pi \sigma_x \sigma_y = \pi \times (0.6 \times 10^{-3}) \times (0.7 \times 10^{-3}) = 1.32 \times 10^{-6} \text{ m}^2, \quad (42)$$

where  $\sigma_{x,y}$  is the spot size on the cavity mirror in each direction. The intensity  $I$  of the laser on the mirror can be found via

$$I = \frac{P}{A} = \frac{80.6 \text{ kW}}{1.32 \times 10^{-6} \text{ m}^2} = 6.11 \times 10^{10} \text{ W/m}^2. \quad (43)$$

The intensity of the laser pulse incident on the mirror is therefore very large. The threshold for optical coating damage for mirrors used in these types of cavities is around  $10^{10}$ - $10^{11} \text{ W/m}^2$  depending on exact material specifications [75]. This also isn't taking into account the fact that the spot size on the mirror would be smaller in a smaller path length recirculation cavity. Consequently, this repetition rate exceeds the current technological limits and would have to be reduced.

## 7.2 Output Spectra

Using the calculations as defined and justified in Section 6.5 the output parameters for the CBETA X-ray ICS can be calculated based on the parameters set in Tables 5 and 6. For these output parameters the value of the average brilliance and spectral energy density is quoted in a 0.1% bandwidth (bw) as this is typical of values used to compare light sources. The spectral energy density is dependent on the bandwidth, which is omitted here as the maximum beam energy spread and laser energy spread are unknown and therefore it can't be calculated. However, the parameter can be calculated in an arbitrary 0.1% bw. The output spectral parameters are shown in Table 8

Parameter	42 MeV	78 MeV	114 MeV	150 MeV
X-ray Peak Energy (keV)	33.5	116	247	427
Flux per shot (ph)	1000	1031	1038	1041
Flux (ph/s)	$1.30 \times 10^{12}$	$1.34 \times 10^{12}$	$1.35 \times 10^{12}$	$1.35 \times 10^{12}$
Average Brilliance (ph/s mm <sup>2</sup> -mrad <sup>2</sup> 0.1% bw)	$3.71 \times 10^{12}$	$1.32 \times 10^{13}$	$2.84 \times 10^{13}$	$4.91 \times 10^{13}$
Spectral Energy Density (ph/s eV 0.1%)	$2.32 \times 10^7$	$6.94 \times 10^6$	$3.27 \times 10^6$	$1.89 \times 10^6$

Table 8: The calculated spectral output parameters for the CBETA X-ray ICS on each recirculation pass. Some values are given for a 0.1% bandwidth in order to allow for light source comparison. The bandwidth is omitted as not enough parameters to calculate this are currently defined.

As shown in Table 8, the CBETA ICS would be a multi-colour source of hard X-rays. This source also offers high flux on the order of  $10^{12}$  ph/s. This value is high enough to fulfil the requirements of users. As seen from Section 9.1 this surpasses all existing X-ray ERL ICS and has a flux competitive with storage ring ICS facilities.

## 7.3 CAIN Spectra

The output spectra of the CBETA ICS has also been simulated for the 150 MeV beam energy and therefore the highest energy X-ray case. The simulation was performed through the use of CAIN (Conglomerat d'ABEL et d'Interactions Non-Lineaires) [4]. The purpose of CAIN is to describe all possible interactions, due to both classical and quantum electrodynamics, between high-energy beams of electrons, positrons and photons and external electromagnetic fields [4]. The CAIN code includes the necessary tools and routines to simulate a single inverse Compton scattering interaction in both the recoil regime, as defined in Section 6.3, and non-linear regime, as defined in Section 6.4. Within CAIN the interaction is modelled through MonteCarlo event generation using the electromagnetic fields created by the (assumed Gaussian) laser pulses. The spectrum of inverse Compton scattering is then formed using a rejection algorithm based on the Compton scattering cross section.

The CAIN simulation of the CBETA ICS at 150 MeV beam energy involved writing a script to describe the laser and electron beams from the parameters specified in Section 7.1 and then using a LASERQED command [76] to specify the inverse Compton scattering interaction. Factors such as whether to include non-linear effects in the calculated spectrum and polarisation are controlled by this command. The simulated CAIN spectra for the CBETA X-ray ICS at 150 MeV is shown in Figure 35.

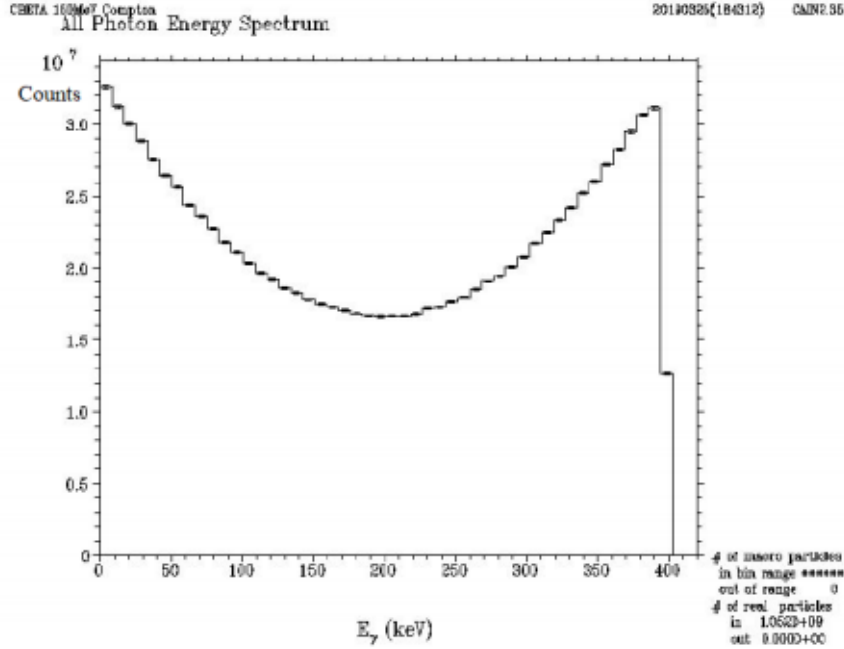


Figure 35: The CAIN spectra for an inverse Compton source at a beam energy of 150 MeV (counts against output photon energy) for a 1 second period. This spectra is based on a head-on collision geometry and uses the laser and beam parameters as specified in Tables 6 and 5. In this plot a full range ( $360^\circ$ ) of observation angle  $\theta$  is used, there is no collimation. Due to limitations of CAIN code (explained below) the repetition rate used to produce this plot is 1 MHz not the 1.3 GHz specified.

The shape of the distribution in Figure 35 is due to the variation of the photon flux and X-ray energy with observation angle  $\theta$ , as governed by the equations in Section 6.5. The dipped shape shown in this spectra is typical of the spectra of inverse Compton scattering. Typically this spectrum is collimated around the high energy peak where the radiation is monochromatic as shown in Section 6.1. This is the part of the spectrum that users desire.

The spectrum of the 150 MeV ICS in Figure 35 isn't the true spectra of the CBETA X-ray ICS as the repetition rate used was 1 MHz not the specified 1.3 GHz. The reason for this is that CAIN is not designed to simulate a recirculating source where there is multiple interactions, it is instead designed to simulate a single interaction of an electron bunch and a laser pulse. Therefore, CAIN could only be used to exactly simulate one shot of an inverse Compton source. However, a simulation of a single shot for the CBETA X-ray source where there is 1041 photons per shot, as in Table 8, is unsatisfactory as this number of photons poorly defines the spectrum.

To simulate a recirculating source in CAIN the recirculating behaviour of the laser pulse must be simulated artificially. The method of doing as such, as used by T. Akagi et al [6] is to multiply the laser power by the repetition rate and setting this at the laser power. This method increases the amount of photons in the laser pulse to the total amount for one second. In this case CAIN is producing the ICS spectra for one second. However, there are two problems with this method: increasing the laser power induces non-linear effects as  $a_0 \ll 1$  no longer applies and CAIN has a hard-coded limit on the laser power so high repetition rates can not be adequately simulated.

The first problem is easily solved, this involves setting the LASERQED command so non-linear effects are ignored. This is acceptable as we have calculated  $a_0 \approx 10^{-4}$  for this source, which means non-linear effects are negligible. The second problem however, is unavoidable as this would involve modifying CAIN to remove or extend this limit. This is ultimately what leads to the use of the 1 MHz repetition rate.

## 7.4 cERL Comparison

To get a sense of the quality and standing of the CBETA ICS it needs to be compared to another ERL ICS. For this purpose the cERL ICS is used [6]. Further X-ray ICS sources are mentioned in Section 20 and a table comparing previous X-ray sources is included. This section is a direct comparison with a similar source, taking the cERL case in detail by looking at the beam and laser parameters not just the output spectra.

The cERL ICS beam and laser Parameters are shown in Table 10 and 9. The laser used here is identical to the Nd:YAG laser proposed to the CBETA ICS.

cERL Laser Parameter	Value
Wavelength ( $\mu\text{m}$ )	1.064
Average Stored Power in the Cavity (kW)	10
Pulse Energy ( $\mu\text{J}$ )	61.5
Repetition Rate (MHz)	162.5
Spot Size at the IP ( $\sigma_x/\sigma_y$ ) ( $\mu\text{m}$ )	24/32
Stored Pulse Width (ps)	5.65
Crossing Angle ( $^\circ$ )	18

Table 9: Parameters of the cERL ICS laser recirculation cavity and laser system [6]. These parameters are identical to the CBETA ICS parameters except the repetition frequency is modified which increases the stored power, a circular laser spot of  $25 \mu\text{m}$  rms size is also used in the CBETA calculations.

cERL Beam Parameter	Value
Beam Energy (MeV)	20
RF Frequency (GHz)	1.3
Repetition Rate (MHz)	162.5
rms Beam Spot Size ( $\sigma_x/\sigma_y$ ) ( $\mu\text{m}$ )	78/16
Normalised transverse rms Emittance ( $\varepsilon_{n,x}/\varepsilon_{n,y}$ ) (mm mrad)	0.32/0.28
rms Bunch Length (mm)	0.6
Bunch Charge (pC)	0.355

Table 10: Beam parameters at the IP of the cERL ICS [6]. The repetition rate is reduced by a factor of 8 and the bunch charge smaller by a factor of  $\approx 100$  from the CBETA ICS parameters. cERL is a single pass ERL and has a top energy of 20 MeV.

The experimental results of the cERL ICS output spectra are shown below in Table 11. Parameters such as the brilliance and spectral energy density are instead calculated for this source as they were not included in the paper by T. Akagi et al [6].

Parameter	Value
X-ray Peak Energy (keV)	6.95
Flux (ph/s)	$2.6 \times 10^7$
Average Brilliance* (ph/s mm <sup>2</sup> -mrad <sup>2</sup> 0.1% bw)	$1.7 \times 10^6$
Spectral Energy Density* (ph/s eV 0.1% bw)	$2.5 \times 10^3$
Bandwidth (0.14 mrad collimation)	0.4%

Table 11: The output spectral parameters for the cERL ICS [6]. The spectral parameters denoted by \* have been calculated based on the parameters of the cERL ICS.

As evident from a comparison of Table 11 and 8, the CBETA ICS is capable of producing X-rays at much higher energy than the soft X-rays produced from the cERL ICS. cERL's peak energy is in fact smaller than that of a conventional hospital X-ray machine which is 20 keV [77]. The flux of the cERL source is also smaller than the proposed CBETA ICS by a factor of  $10^5$  ph/s. As well as this, the spectral brilliance in a 0.1% bandwidth of the CBETA ICS is a factor of  $10^7$  times higher than in cERL. Because of this the ICS in CBETA, as currently planned, would be a much higher quality light source than the cERL ICS.

## 7.5 CBETA ICS Bypass

In order to implement an inverse Compton source within CBETA, the laser recirculation cavity needs to be included within the lattice as well as a set of focusing optics. The purpose of the focusing optics are to reduce

the beam spot size at the interaction. In the CBETA ICS case this involves attempting to achieve a beta function at the inverse Compton interaction point of  $\beta^* = 1$  cm, as described in [61] and Table 6. A possible solution to this, a bypass of the straight section of the CBETA recirculating loop, is investigated here. The bypass is designed to start at the ZA section of the CBETA return loop to bypass the straight FFAG transport sections ZA, ZB and then be returned to the CBETA return loop at the end of the ZB straight section. This is shown diagrammatically in Figure 36.

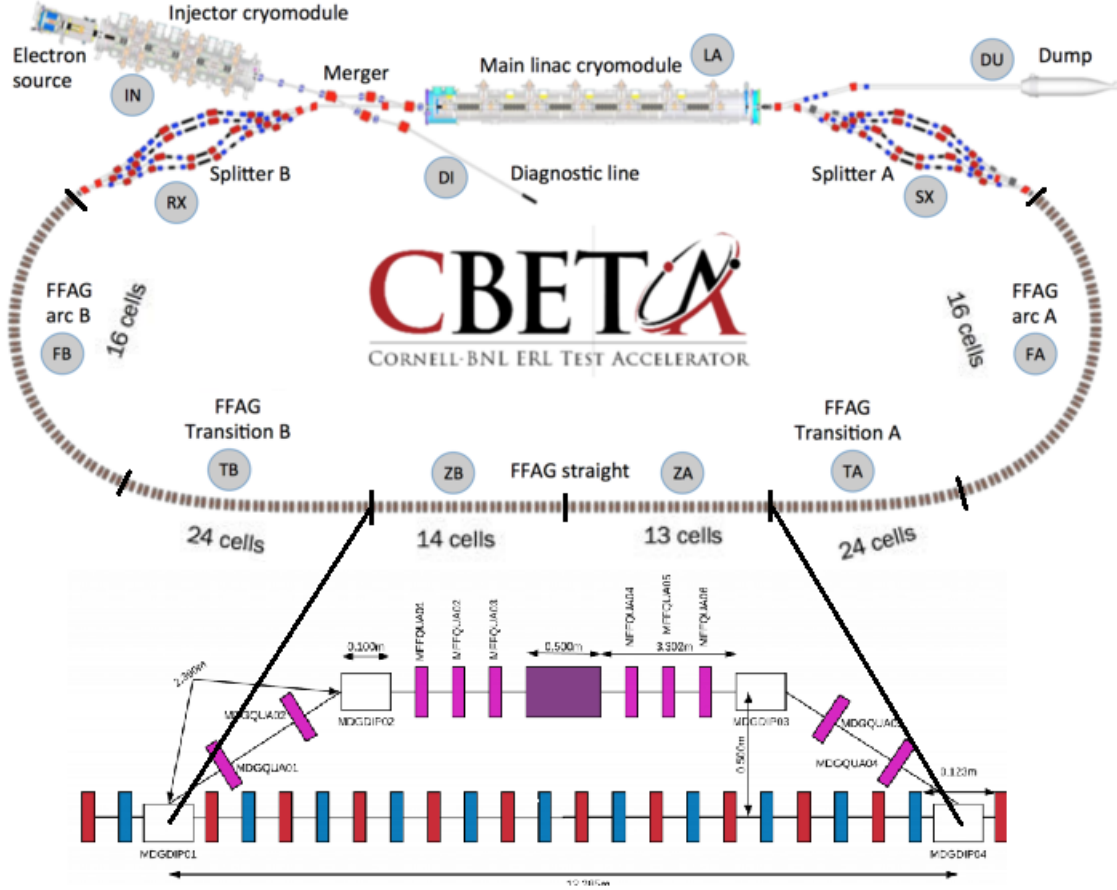


Figure 36: The CBETA ERL showing the various sections of the CBETA FFAG return loop: RX/SX the splitter/recombiner sections, FA/FB the recirculating arcs, TA/TB the transition sections, ZA/ZB the straight sections. These are each made up of a corresponding number of modular cells. The bypass is across the straight FFAG section ZA+ZB, the first and last dipoles of the chicane are at the start of ZA and the end of ZB, implemented where the straight sections meet their respective transition sections TA and TB. The bypass is built 0.5m inward, toward the linac, in order to avoid overlap of magnets. The bypass design (bottom) is shown again in Figure 37 and explained there.

The bypass is designed as a type of chicane, two doglegs are designed to offset the beam transversely 0.5m from the start of the FFAG straight (start of ZA section) and then to return the beam to the current lattice at the end of the straight (end of ZB section). The 12.285m section of straight (start of ZA to end of ZB) is bypassed through the ICS additional beam line. The 0.5m transverse offset from the current position of the FFAG straight is chosen to avoid the overlap of magnets as the CBETA FFAG quadrupoles have a total width of 0.173m (including mountings etc.) and there would now be two parallel rows of these, plus the quadrupoles at angles to the FFAG in the doglegs (MDGQUA01) needs to avoid overlapping the FFAG.

Within the section between the two doglegs a system of focusing magnets will be implemented to achieve the necessary beta function at the interaction point  $\beta^*$ . The position of the inverse Compton scattering interaction point is within the centre of the 0.5m long laser recirculation cavity.

The bypass of the straight section for the inverse Compton interaction beam line consists of a 0.5m laser recirculation cavity, 10 quadrupoles for focusing and the 4 dipoles which make up the chicane. A diagram of the CBETA ICS bypass is shown in Figure 37.



Component	Length (m)	Strength (k1 or g)
Dipoles		
MDGDIP01	0.10	-0.587
MDGDIP02	0.10	0.587
MDGDIP03	0.10	0.587
MDGDIP04	0.10	-0.587
Dogleg Quadrupoles		
MDGQUA01	0.15	-1.524
MDGQUA02	0.15	2.747
MDGQUA03	0.15	3.285
MDGQUA04	0.15	-4.049
Focus Quadrupoles		
MFFQUA01	0.15	-2.061
MFFQUA02	0.15	3.484
MFFQUA03	0.15	-2.723
MFFQUA04	0.15	-2.693
MFFQUA05	0.15	3.619
MFFQUA06	0.15	-2.291

Table 12: A table showing the lengths and normalised strengths of the quadrupole and dipole magnets utilised in the bypass. The magnets are categorised by the magnet code MDG (dogleg magnet) or MFF (focus magnet) to match with the similar convention used in the CBETA Bmad lattice file. The dipoles all have a magnetic flux density of  $B = 1$  T and the quadrupole magnets all have gradient values under 8 T/m. These are within strengths that are possible to construct for normal conducting magnets therefore the bypass system is easy to manufacture with relatively simple, inexpensive magnets.

The bypass design was simulated using Bmad [62] and Tao [63] and optimised to the values seen in Table 12. The floor plan constructed from the Bmad simulation of this bypass lattice is shown in Figure 38 and the graphs of the  $\beta$ ,  $\alpha$  and dispersion functions are shown in Figure 39.

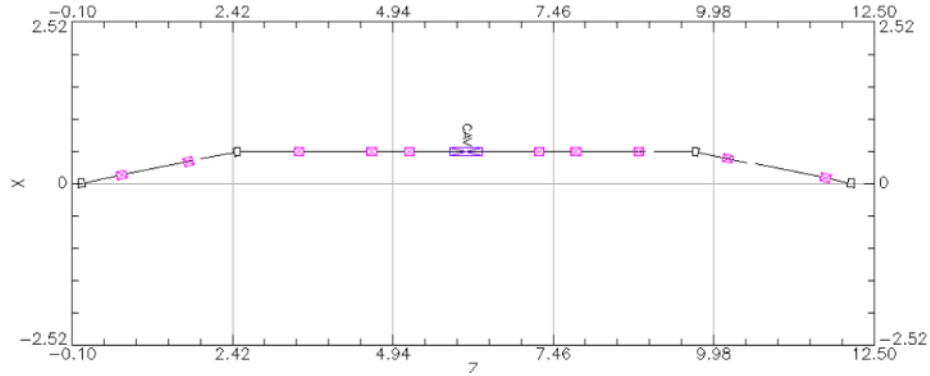


Figure 38: The floor plan of the CBETA ICS bypass showing quadrupoles (pink boxes), dipoles (black boxes) and the ICS cavity (purple box). This shows the cavity is of the correct length 12.225 m in  $Y$ , the length of the FFAG straight, and is stepped inwards by 0.5 m in  $X$ .

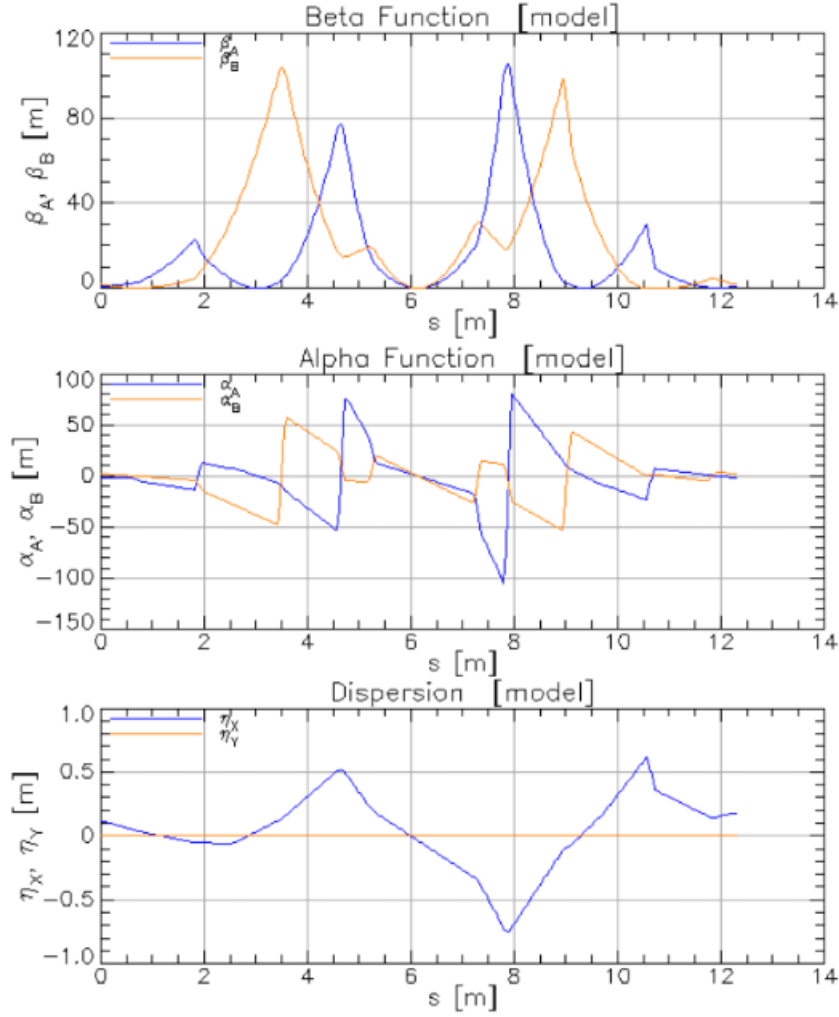


Figure 39: Top: The  $\beta$  functions throughout the bypass lattice. The  $\beta$  function here is focused to  $\beta^*$ , the beta function at the IP, at the centre of the lattice where the ICS interaction point is. The  $\beta$  functions are also constrained to be under 100 m in this region so there is no large blow up of the beam in order to achieve the focus. Middle: The  $\alpha$  functions throughout the bypass lattice. The alpha function, whilst minimised at the interaction point peaks at a large value of  $\alpha = 50$ . Bottom: The dispersion plot throughout the bypass. The dispersion function  $\eta_x$  shows irregular behaviour from 10 m onwards. The dispersion is not well matched at the end of the lattice where it re-enters the FFAG return loops to the previous values at that point. A better scheme may be to use a dispersion suppressor to set  $\eta_x = 0$  throughout the bypass.

The aim of the optimisation of the Twiss functions of the CBETA bypass was to reduce the  $\beta$  functions at the focus to 1 cm whilst retaining the parameters found in CBETA's FFAG straight at the end of the ZB section where the bypass is merged back into the return loop. The Twiss parameters from the simulation of the CBETA 4-pass lattice at the end of the ZB straight section (target parameters) are compared with the Twiss parameters at the end of the simulated bypass (achieved parameters).

The  $\beta^* = 1$  cm value for the interaction point was chosen by Dr Kirsten Deitrick and is shown in [61]. This is just a straw-man parameter for the focus. For the CBETA ICS, as shown in Section 7.1, this would result in a beam spot size  $\sigma_{e,x}$  (22) much smaller than the laser spot size. This parameter is therefore over constrained, therefore the constraint was reduced to 4 cm for this optimisation. The target and achieved values for the optimisation of the bypass lattice are summarised in Table 13.



Optimised Parameter	Target	Achieved
$\beta^*$ (m)	0.01	0.04
$\beta_{x,end}$ (m)	0.7503	0.6878
$\beta_{y,end}$ (m)	1.9000	2.1193
$\alpha_{x,end}$	-1.0049	-0.8838
$\alpha_{y,end}$	2.4302	2.5938
$\eta_{x,end}$ (m)	-0.0508	0.1798
$\eta_{pc,end}$	0.0659	-0.1691

Table 13: The target and achieved parameters for the optimised bypass. The end Twiss parameters that are targeted arise from those in the CBETA 4-pass Bmad lattice at the start of the TB transition section where the beam is merged from the bypass into the return loop. These are taken from the lattice in normal 4-pass operation - the bypass is not used. These are then compared to the parameters at the end of the bypass. The 1 cm  $\beta$  function at the interaction point was set as a straw-man parameter for the source. The  $\beta^*$  parameter achieved is a factor of 4 larger than targeted. The  $\alpha$  and  $\beta$  functions at the end of the lattice differ at maximum 12% from the target value. The dispersion and momentum dispersion functions are very poorly matched. There is also a change of sign for  $\eta_x$  and  $\eta_{px}$ .

The matching between the Twiss functions at the end of the bypass and the start of the TB section is poor. The 12% variation between the target and achieved parameters for the  $\alpha$  and  $\beta$  functions means the trajectory of the beam could then be unstable. The dispersion and momentum dispersion have an even greater variation from those in the standard lattice. Therefore, the dispersion is not correctly matched and this effects the longitudinal dynamics which could result in beam loss.

This optimised bypass lattice was then added into the CBETA 4-pass lattice i.e the ZA and ZB straight section for the 150 MeV pass of the return loop were replaced by the bypass lattice. The simulation used the standard FFAG return loop for the 1st to 3rd pass and then on the 4th pass the return loop bypassing the ZA, ZB straight was used, for the decelerating passes after this the standard FFAG return loop was again used by the simulation. A comparison between the orbit,  $\beta$  functions and dispersion in both the unmodified CBETA lattice and the CBETA lattice using the the bypass on the 4th pass is shown in Figure 40.

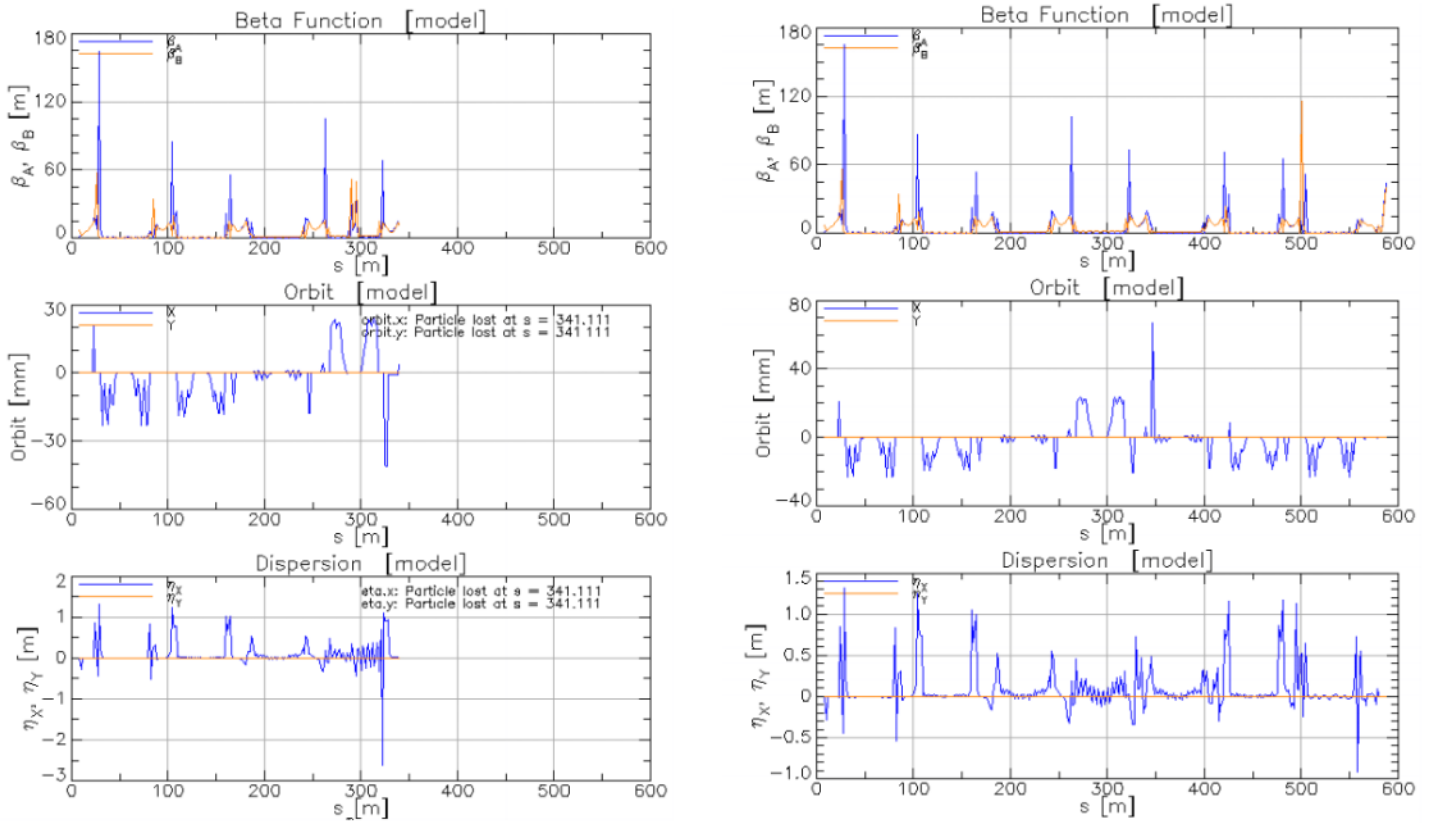


Figure 40: These plots are from simulations of the CBETA 4-pass lattice. The  $\beta$  function plot can be related to the lattice sections at the peaks in this are typically due to the splitter/recombiner sections. From left to right the structure from the  $\beta$  function plot is: S1 (peak), return loop (flat), R1 (peak), linac (flat), S2 (peak) etc. This is explained in more detail in Section 5. Left: The 4-pass lattice with the inclusion of the bypass on the 4th pass. The bypass ends at around 298 m. Top: The  $\beta$  function plots in  $x$ - $y$ . A series of peaks can be seen at around 300 m in the left plot in comparison to the right plot. These peaks are the  $\beta$  functions of the bypass. After the bypass the beam continues to propagate with similar  $\beta$  functions as in the standard 4-pass lattice until it is lost. Middle: The  $x$  and  $y$  orbit plot of the bypass included simulation and the standard CBETA lattice simulation shows that there is a larger orbit excursion at around 320 m in the bypass included simulation. The beam is lost soon after. Bottom: The dispersion plot of the bypass included and regular CBETA lattice 4-pass simulations. The dispersion in the bypass included plot shows a steady uncontrolled increase in the oscillation of the dispersion function up to the point at which the beam is lost.

Figure 40 shows that with the optimised bypass the beam is lost. The position the beam is lost is at the start of the R4 recombiner ( $s = 341.1$  m). This suggests the match was too poor in order to create a stable orbit. From the dispersion plot in Figure 40 it is possible to see that the dispersion function becomes uncontrolled. Therefore this uncontrolled behaviour could possibly be the cause of the loss of the beam.

The design of the bypass for the CBETA ICS is a work in progress. The design is deficient as there are not enough focus quadrupoles and therefore not enough free parameters in the optimisation to satisfy the constraints. The bypass is an over-constrained system. In addition, the bypass would benefit from a design in which the dispersion is suppressed throughout the bypass as zero dispersion is required for the inverse Compton scattering interaction. Consequently, it is unsurprising that the bypass was incapable of producing a stable orbit. Further work in designing the bypass is required.

## 8 DIANA $\gamma$ -ray Inverse Compton Scattering Source

### 8.1 The DIANA ERL

The Daresbury Industrial Accelerator for Nuclear Applications (DIANA) is a proposed 3-pass electron beam energy recovery linac utilising to be built at Daresbury, UK. It is proposed as a racetrack machine design with two SRF linacs, similar to CEBAF although the exact topology is currently undecided. The beam would gain +170 MeV per pass of the linac [5]. A drawing of the proposed DIANA ERL is shown in Figure 41.

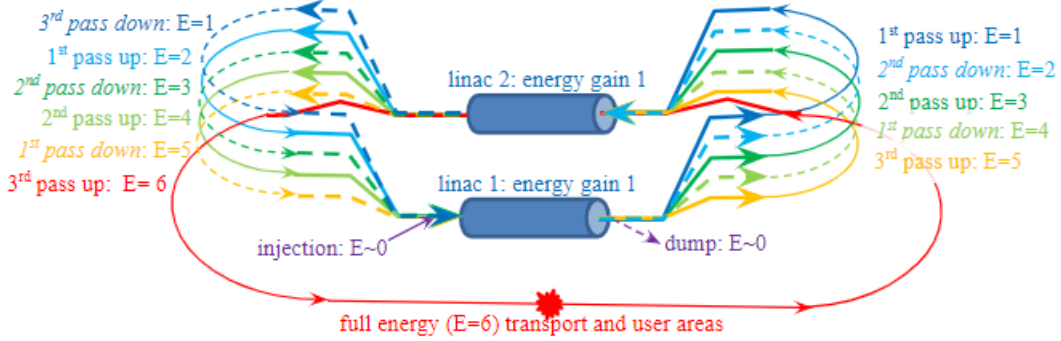


Figure 41: The 3-pass ERL DIANA with a north and south linac and vertically stacked separate transport. The colour co-ordination shows the configuration of each of the 6 passes in these return arcs (3 accelerating, 3 decelerating).

Figure 41 shows just one of the possible topologies, for example a paper clip topology, where a final 6th pass full length recirculating loop (one that doesn't pass the linacs) could be used in order to extend to more user areas. Common transport by the use of FFAG return arcs, as in CBETA, is also being considered for this project. It is at a very early stage in design.

### 8.2 $\gamma$ -ray ICS Design

The DIANA ERL is designed to operate at a maximum beam energy of 1.02 GeV, increasing by +340 MeV per circulation. Therefore an  $\gamma$ -ray inverse Compton scattering source on DIANA would enter the recoil/Compton regime as defined in Section 6.2. The electron beam and laser recirculating cavity and laser system parameters are shown in Table 14 and 15.

Beam Parameters	Value
Beam Energy (MeV)	340, 680, 1020
RF Frequency (MHz)	802
Repetition Rate (MHz)	100
Bunch Charge (pC)	100
Average Beam Current (mA)	10
Normalised transverse Emittance (mm mrad)	0.5
$\beta$ function at the IP $\beta^*$ (m)	0.5
Recoil Parameter X	0.006, 0.012, 0.018

Table 14: The target beam parameters for the DIANA ICS interaction point. These beam parameters are set in [5] by Dr Peter Williams. These are conservative parameters. ERL's have been proposed with parameters that far exceed those of DIANA for example, 40 mA average beam current in CBETA [17] and 12 GeV beam energy for CEBAF [46].

<b>Nd:YAG Laser Parameters</b>	<b>Value</b>
Wavelength (nm)	1064
Repetition Rate (MHz)	100
Pulse Energy ( $\mu\text{J}$ )	100
Average Stored Power in Cavity (kW)	10
Spot Size at IP ( $\mu\text{m}$ )	25
Stored Pulse Width (ps)	5.7
Field Strength of the Normalised Laser Vector Potential $a_0$	$6.05 \times 10^{-4}$

Table 15: Initial parameters for the CBETA ICS laser recirculation cavity and laser system. Again, these parameters are based on the cavity used in the cERL ICS [6] which also uses an Nd:YAG laser. The cavity parameters have been adjusted by the reduction of the repetition rate and increased pulse energy. However, the average power stored in the laser recirculation cavity as shown by T. Akagi et al [6] is maintained.

The laser parameters have been set based on what was believed to be the limiting factors on the cavity, as explained in Section 7.1. This includes the path length of the cavity and the power incident on the mirrors. Therefore, the choice repetition rate was first motivated by the need to keep the cavity a realistic size. By equation (40), at 100 MHz the cavity path length is 3 m which is a plausible total cavity path length ( $\approx 3/4$  m longitudinal size). Then since we know the power stored in the the cERL ICS cavity is 10 kW [6] and that this is a tolerable power for cavity mirrors, we adjust our laser pulse energy to store 10 kW in the cavity through equation (41) which achieves 100  $\mu\text{J}$ . This is an achievable pulse energy with a commercial system and therefore this value is chosen.

The choice of an Nd:YAG laser is because this laser is routinely used within accelerators and ICS, therefore it is a mature laser technology that could be easily incorporated into a laser recirculation cavity system. The laser gives the right trade-offs between photon energy, pulse energy and pulse length that is favourable in inverse Compton scattering sources. In addition, there are a range of Nd:YAG commercial laser systems available. Other options for a laser system would be the Ti:Sa laser or Nd:YLF laser.

For this system the spot size was chosen as 25  $\mu\text{m}$ , this is as it is of similar value to the laser spot size achieved by T. Akagi et al [6]. With the emittance value for the beam and the fact that the flux is based on a convolution of the laser pulse transverse size and beam pulse transverse size (21) it is not beneficial for the flux (24) of the source to reduce this further.

### 8.3 Output Spectra

The defining parameters of the output spectra of the DIANA ICS can be calculated using the equations from Section 6.5. These calculations use the straw-man laser system and electron beam parameters set for the DIANA inverse Compton source in Section 8.2. Again, as for the CBETA ICS some parameters are quoted in a 0.1% bandwidth as this is useful for light source comparison. The output spectral parameters of the DIANA  $\gamma$ -ray source are shown in Table 16.

<b>Parameter</b>	<b>340 MeV</b>	<b>680 MeV</b>	<b>1020 MeV</b>
$\gamma$ -ray Peak Energy (MeV)	2.05	8.17	18.27
Flux per Shot (ph)	4076	4750	5027
Flux (ph/s)	$4.08 \times 10^{11}$	$4.75 \times 10^{11}$	$5.03 \times 10^{11}$
Average Brilliance (ph/s mm <sup>2</sup> -mrad <sup>2</sup> 0.1% bw)	$2.75 \times 10^{13}$	$1.27 \times 10^{14}$	$3.04 \times 10^{14}$
Peak Brilliance (ph/s mm <sup>2</sup> -mrad <sup>2</sup> 0.1% bw)	$4.79 \times 10^{16}$	$2.24 \times 10^{17}$	$2.67 \times 10^{17}$
Bandwidth	0.15%	0.27%	0.41%
Spectral Energy Density (ph/s eV)	$5.24 \times 10^7$	$8.47 \times 10^6$	$2.62 \times 10^6$

Table 16: The calculated spectral output parameters for the DIANA  $\gamma$ -ray ICS. Values are given within a 0.1% bandwidth for the purpose of light source comparison. For the bandwidth the laser wavelength spread is given as  $\Delta\lambda = 0.7$  nm from discussions with Dr Laura Corner and the beam energy spread  $\frac{\Delta E_e}{E_e}$  is  $10^{-4}$ .

This is a high flux  $\gamma$ -ray ICS producing  $10^{11}$  ph/s, the average brilliance of the source is very high - on the order of  $10^{14}$  ph/s mm<sup>2</sup>-mrad<sup>2</sup> - therefore, this is a very high quality source of radiation.

It has also been stipulated that the output radiation of the DIANA ICS should have an energy deviation  $\Delta E_x$  of no more than 100 keV. This was driven by the precision required for applications such as nuclear resonance fluorescence. Therefore, 100 keV is the maximum energy spread tolerable in the output radiation. Consequently, this can be used to set the maximum allowed bandwidth for each of the 3 passes of DIANA, these are given as

$$\frac{\Delta E_x}{E_x^{1020 \text{ MeV}}} = \frac{0.1 \text{ MeV}}{18.27 \text{ MeV}} = 0.55\%, \quad (44)$$

$$\frac{\Delta E_x}{E_x^{680 \text{ MeV}}} = \frac{0.1 \text{ MeV}}{8.17 \text{ MeV}} = 1.22\%, \quad (45)$$

$$\frac{\Delta E_x}{E_x^{340 \text{ MeV}}} = \frac{0.1 \text{ MeV}}{2.05 \text{ MeV}} = 4.88\%. \quad (46)$$

The bandwidths calculated for DIANA in Table 16 all have bandwidths below this limit. Therefore an ICS based on each pass of DIANA with current laser and electron beam parameters could have a radiation energy spread less than 100 keV ( $\Delta E_x < 100 \text{ keV}$ ).

## 8.4 ELI-NP Comparison

Currently, there have been no inverse Compton  $\gamma$ -ray sources proposed in any detail on energy recovery linacs. The only proposal was a version of the ELI-NP [7] proposal as an ERL. However, this proposal was never completed in detail. Therefore, the DIANA inverse Compton source will be compared to the ELI-NP conventional linac  $\gamma$ -ray ICS as specified in the EurogammaS technical report [78]. Further  $\gamma$ -ray sources are explored within Section 9.2. Here a more in-depth comparison is made where the electron beam and laser parameters, as shown in Tables 18 and 17 as well as the output spectral parameters in Table 19.

ELI-NP Laser Parameter	Value
Wavelength (nm)	515
Pulse Energy (J)	0.4
Repetition Rate (Hz)	100
Spot Size at the IP ( $\sigma_L$ ) ( $\mu\text{m}$ )	28
Stored Pulse Width (ps)	3.5
Crossing Angle ( $^\circ$ )	7.5

Table 17: Parameters of the ELI-NP laser recirculation cavity and laser system [78]. This produces a high energy laser pulse that is interacted with 32 micro-bunches individually in the laser recirculation cavity before being replaced. The pulse energy of the laser is much higher than in DIANA however the repetition rate is much smaller than in DIANA since it is a linac based ICS.

ELI-NP Beam Parameter	Value
Beam Energy (MeV)	80-720
RF Frequency (GHz)	2.856
Repetition Rate (Hz)	100
rms Beam Spot Size ( $\mu\text{m}$ )	> 15
Normalised transverse rms Emittance ( $\varepsilon_n$ ) (mm-mrad)	0.2-0.6
rms Bunch Length ( $\mu\text{m}$ )	100-400
Bunch charge (pC)	25-400

Table 18: The beam parameters of the ELI-NP linac at the inverse Compton interaction point [78]. DIANA and ELI-NP have similar specifications for the beam parameters and quality of the beam. Both typically operate with 100's pC bunches at 100's MeV with normalised transverse emittance that is on the order of 0.5.

From the Tables 18 and 17 it is evident that both ELI-NP and DIANA aim to have similar quality beams with similar parameters from both a linac and an ERL. The main difference between the sources here is that

ELI-NP has a more powerful, higher-energy laser system with a low 100 Hz repetition rate whereas DIANA has a high repetition rate 100 MHz low energy laser recirculation system. ELI-NP also uses the 2nd harmonic of a Yb:YAG laser allowing access to higher peak energy  $\gamma$ -rays. The specification of the  $\gamma$ -ray beam output for ELI-NP is shown below in Table 19.

$\gamma$ -ray Energy (MeV)	0.2-19.5
Flux per shot (ph)	$8.3 \times 10^6$
Flux (ph/s)	$8.3 \times 10^8$
Average Brilliance (ph/s mm <sup>2</sup> -mrad <sup>2</sup> 0.1% bw)	-
Peak Brilliance (ph/s mm <sup>2</sup> -mrad <sup>2</sup> 0.1% bw)	$10^{20} - 10^{23}$
Bandwidth	$\leq 0.5\%$
Spectral Energy Density	$0.8-4 \times 10^4$

Table 19: The spectral output parameters for the ELI-NP  $\gamma$ -ray inverse Compton source [78]. The parameters here show a high quality  $\gamma$ -ray source focused on producing a narrow-band source of  $\gamma$ -rays. The ELI-NP source has a high peak brilliance, ( $10^3 - 10^6$ ) larger than DIANA. However, the ELI-NP flux is a factor of  $10^3$  smaller than DIANA.

When comparing the ELI-NP and DIANA output spectral parameters in Table 19 and 16, it is clear to see the main difference is in the flux of the sources and the peak brilliance. The flux of the DIANA source is on the order of  $10^3$  larger than that of ELI-NP, this is purely because of the high repetition rate (DIANA  $10^8$  Hz  $\gg$  100 Hz ELI-NP) of the inverse Compton interaction in DIANA due to the recirculating design of both the beam and laser cavity. However, the flux per shot i.e the number of photons produced in a single interaction is much higher in ELI-NP ( $8.3 \times 10^6$  ph) than in DIANA (4076-5027 ph). This shows that the ELI-NP produces photons at a much higher rate per interaction than in DIANA. As well as this, when comparing the peak brilliance (DIANA  $2.67 \times 10^{17}$  ph/s mm<sup>2</sup>-mrad<sup>2</sup>  $< 10^{23}$  ph/s mm<sup>2</sup>-mrad<sup>2</sup> ELI-NP) it becomes apparent that ELI-NP is focused on producing a large amount of high-quality  $\gamma$ -rays in a single pulse whereas DIANA aims to produce more high quality  $\gamma$ -rays but over a longer time-scale. The spectral energy density of ELI-NP is also lower than that of DIANA which is a consequence of recirculation. In conclusion, ELI-NP is a machine focused on peak  $\gamma$ -ray radiation output whereas DIANA is focused on average radiation output.

## 8.5 Nuclear Resonance Fluorescence

One of the main applications of the DIANA ICS that has been investigated so far is nuclear resonance fluorescence. This is an application which typically requires a narrow-band ( $< 1\%$ ) source of 1-3 MeV  $\gamma$ -rays. Therefore the 340 MeV beam energy first pass of DIANA with a peak energy of 2.05 MeV is close to the correct peak energy required for NRF studies.

Resonance fluorescence refers to the resonant excitation of an excited state by the absorption of electromagnetic radiation and the subsequent decay of this level by emission of radiation [79]. The emitted radiation from NRF is characteristic of the energy level separation of nuclei, because of this isotopes can be distinguished through this mechanism. For this mechanism, which is typically used in high Z nuclides, the requirement for excitation is generally a few MeV and therefore  $\gamma$ -rays are required. This application is particularly useful in the detection of clandestine nuclear material and identification of legacy nuclear wastes. Figure 42 illustrates the process of NRF.

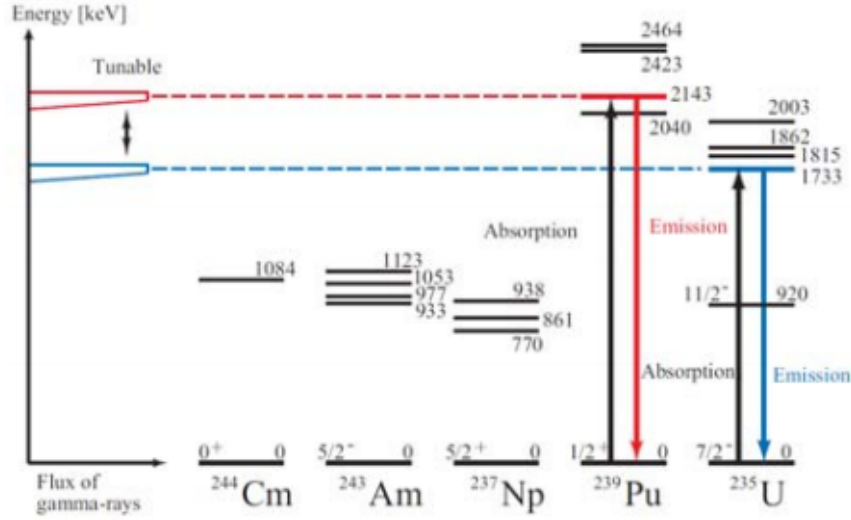


Figure 42: This diagram shows the process of NRF [80]. The diagram shows the energy level diagrams of two isotopes of interest Uranium 235 and Plutonium 239 and those of some common nuclides also found in reactor waste: 243 Americium, 244 Curium and 237 Neptunium. The red line illustrates how a 2.143 MeV  $\gamma$ -ray could be used to resonantly excite 239 Plutonium and subsequently cause emission of a photon. The characteristic emitted photons can be detected which then indicates the presence and abundance of the isotope of interest. Similarly the blue line shows this for 235 Uranium with a 1.733 MeV  $\gamma$ -ray. This is illustrating that a tune-able source of  $\gamma$ -rays could be used to image isotopes of interest in a mixture of isotopes such as nuclear waste.

An inverse Compton scattering source on the first pass of DIANA would, when properly tuned, be able to precisely and accurately image the two isotopes of interest  $^{235}\text{U}$  and  $^{239}\text{Pu}$ . These require  $\gamma$  rays at the characteristic energies of  $E_{239\text{Pu}} = 2.143 \text{ MeV}$  and  $E_{235\text{U}} = 1.733 \text{ MeV}$ . The  $\gamma$  ray energy in the DIANA ICS must be able to be tuned to these values.

The peak energy equation shows us the possible methods of tuning the  $\gamma$ -ray ray energy, as shown in (9) it is given by

$$E_{\gamma} = \frac{4\gamma^2 E_L}{1 + (\gamma\theta)^2 + X}, \quad (47)$$

where the symbols have the same meaning as explained in the original instance of this equation in Section 6.1. This shows either the observation angle  $\theta$  can be manipulated to reduce the energy of the  $\gamma$ -ray observed or the beam energy, which in turn alters the Lorentz factor  $\gamma$ , can be increased or decreased to vary the  $\gamma$ -ray energy.

By changing the observation angle  $\theta$  the  $\gamma$ -ray energy is reduced. This could be used, for example, to achieve the characteristic energy of 235 U at 1.733 MeV where an observation angle of  $\theta = 0.66 \text{ mrad}$  is required. This is calculated through a rearrangement of the peak energy equation (47) for  $\theta$  using the DIANA parameters in Tables 14 and 15.

The tuning method of changing the observation angle requires no alteration of the laser recirculation cavity or the electron beam, the collimation system would just have to be adjusted. However, the downside of this method is that the flux from the source is dependent upon this observation angle. As can be seen from the spectra produced in CAIN in Figure 35 for the CBETA ICS, the number of counts is dependent upon angle. The flux in a collimation angle  $\Psi = \gamma\theta$ , where  $\theta$  is the observation angle, is governed by equation (27) by L. Serafini et al, as shown in Section 6.5

$$F_{\Psi} = 6.25 \times 10^8 \frac{E_{\text{pulse}}[J]Q[\text{pC}]f[\text{Hz}]}{E_L[\text{eV}]\sigma_x[\mu\text{m}]\sigma_y[\mu\text{m}]} \times \frac{(1 + \sqrt[3]{X}\Psi^2/3)\Psi^2}{[1 + (1 + X/2)\Psi^2](1 + \Psi^2)} = F \times \frac{(1 + \sqrt[3]{X}\Psi^2/3)\Psi^2}{[1 + (1 + X/2)\Psi^2](1 + \Psi^2)}, \quad (48)$$

where  $E_{\text{pulse}}$  is the laser pulse energy  $Q$  is the bunch charge,  $F$  is the repetition rate,  $E_L$  is the photon energy of the laser,  $\sigma_{x,y}$  is the convolution of the laser pulse and electron beam spot sizes in the transverse  $x$  and  $y$  planes and  $X$  is the recoil parameter. This equation is based upon the head-on flux (crossing angle  $\phi=0$ ), although by

replacing the  $F$  in (48) by the flux at a crossing angle  $\phi$  as given by (24) this equation could produce the flux at an observation angle in that case as well.

The other tuning method to adapt the output  $\gamma$ -ray energy to the NRF energy required is to increase or decrease the beam energy, thereby varying the Lorentz factor  $\gamma$ . This means that the 2.143 MeV characteristic energy of 239 Plutonium can be probed by the 1st pass of the DIANA ICS. For example, to produce a 2.143 MeV  $\gamma$ -ray the beam energy would need to be increased to 345.8 MeV, a 1.7% increase in beam energy.

The benefit of this method is that the flux doesn't reduce due to the variation of flux with observation angle shown in (48) as the observation angle is unchanged. However, the flux is changed as the beam spot size, as given by (22), is increased with decreasing beam energy or vice versa. Therefore the convolution of laser pulse and electron bunch sizes is altered and consequently the flux. However, for small variations in the beam energy ( $< 10\%$ ), this effect will be negligible. For example, a change in the beam energy  $\Delta E_{beam} \approx \pm 10\%$  gives a maximal change in the flux of  $\approx 1.7\%$ , which occurs for the condition that the beam size is much greater than the laser spot size ( $\sigma_e \gg \sigma_L$ ). Therefore, in a realistic situation such as the 239 Plutonium tuning, which would cause a flux increase of 1.14%, this effect is minimal. The condition ( $\sigma_e \gg \sigma_L$ ) is not usually satisfied as the beam spot size is typically a similar size to the laser spot size or smaller ( $\sigma_e \approx \sigma_L$ ). Because of this the effect of changing the beam energy on the flux is usually smaller, the condition ( $\sigma_e \gg \sigma_L$ ) is for the worst case scenario.

Another caveat is that the energy acceptance of the transport line to the interaction point must be large enough to handle this tuning value. The interaction point position for the inverse Compton scattering interaction must change as the trajectory will vary with energy or vice-versa. In order to be able to use this method of tuning, significant modification of the ICS or lattice may be required.

## 9 Comparison of Inverse Compton Sources on ERLs, Storage Rings and Conventional Linacs

### 9.1 X-ray Inverse Compton Scattering Sources

Within this section examples of X-ray inverse Compton sources on ERLs, storage rings and conventional linacs are considered and compared using a single case study for each. The motivation for the comparison of ICS on different forms of accelerator is due to the differing repetition rate and beam quality achievable on these accelerator types, which in turn effect the output parameters of the inverse Compton sources which utilise them. For example, the nature of a storage ring would allow a large repetition rate of the beam. However, the equilibration of the beam in a storage ring can increase the emittance which can negatively effect the source in terms of flux and bandwidth as the equations in Section 6.5 show. Therefore, differing accelerator types can have strengths and weaknesses as drivers of inverse Compton scattering sources. This is the start of an investigation into the question of which accelerator is the appropriate driver in which case.

For the investigation into X-ray ICS the case studies of the SPARC conventional linac ICS [81], the Lyncean Technologies Compact Light Source (Lyncean CLS) [60] storage ring ICS and the cERL ICS [6]. The output spectral parameters of all of these sources plus an additional example of an ICS on each type of accelerator are shown in Table 20.



<i>Linac ICS Spectral Parameters</i>		
Parameter	SPARC Lab (2016) [82]	MIT ICS (2009) [83]
X-ray Energy (keV)	20-22	3-30
Bandwidth	1%	10-20%
Photons/sec (ph/s)	$3 \times 10^{14}$	$10^{10}$
Peak Brilliance (ph/s mm <sup>2</sup> -mrad <sup>2</sup> 0.1% bw)	$2.18 \times 10^{19}$	$6 \times 10^{19}$
<i>Storage Ring ICS Parameters</i>		
Parameter	Lyncean CLS (2018) [60]	ThomX (2014) [84]
X-ray Energy (keV)	8-40	46-90
Bandwidth	3-9%	1-10%
Photons/sec (ph/s)	$3 \times 10^{11}$	$10^{11} - 10^{13}$
Peak Brilliance (ph/s mm <sup>2</sup> -mrad <sup>2</sup> 0.1% bw)	-	$1.7 \times 10^{15}$
<i>ERL ICS Parameters</i>		
Parameter	ALICE (2010) [58]	cERL (2016) [6]
X-ray Energy (keV)	21.5	6.95
Bandwidth	< 1%	0.41%
Photons/sec (ph/s)	$9 \times 10^7$	$2.6 \times 10^7$
Peak Brilliance (ph/s mm <sup>2</sup> -mrad <sup>2</sup> 0.1% bw)	$1.28 \times 10^{17}$	$1.85 \times 10^{10}$

Table 20: Output spectral parameters of a series of design proposals (red) of inverse Compton sources and operated (blue) ICS sources based on different forms of accelerator: conventional linac, storage ring and ERL. The years in which the design parameters were proposed are shown for the proposed sources. Alternatively, for the operated sources these are the years of the experimental results. The typical output parameters presented for X-ray sources are shown here, the given (black) values are shown alongside calculated (green) values for certain sources in which this information was not provided. Where there is a lack of information provided to calculate a parameter a - symbol is used.

The SPARC Thomson source uses a 30-150 MeV electron beam, a similar range to that from the CBETA ERL, with a 100-800 pC bunch charge and 1-3 mm-mrad normalised transverse emittance [85]. Therefore, this is a high quality electron beam as it has a low emittance whilst retaining a high bunch charge. Figure 43 shows the SPARC lab ICS.

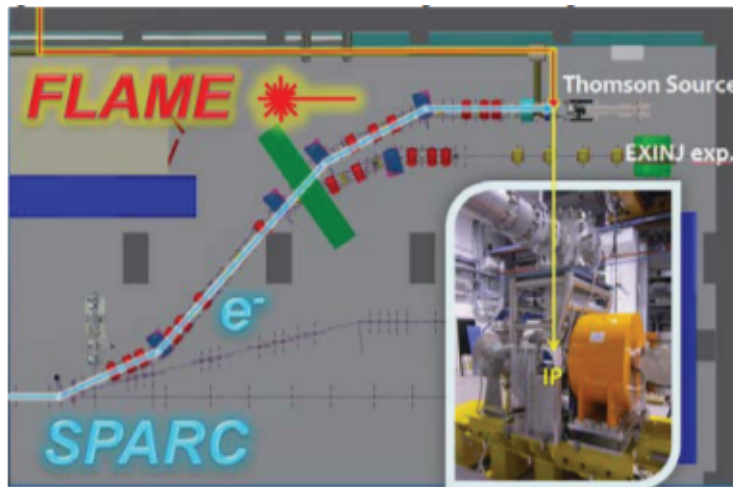


Figure 43: The SPARC Lab Thomson source [85]. In this machine the electron beam from the high brightness SPARC photo-injector is collided in a head-on configuration with the FLAME Ti:Sa  $\lambda = 800$  nm wavelength 300 TW laser. The inverse Compton interaction produces a large number ( $3 \times 10^{13}$  ph/s) of X-ray photons.

This source uses a high peak power 300 TW Ti:Sa ( $\lambda = 800$  nm) laser named FLAME which has a repetition

rate of 10 Hz and a pulse energy of 5 J [85]. This repetition rate is the limiting factor on the repetition rate of the SPARC Lab ICS. Due to the very large laser pulse energy, high bunch charge and low repetition rate the source produces a very high number of photons per shot  $3 \times 10^{13}$  ph/s [82] however this does not improve considerably over the duration of a second. The SPARC Lab linac source is exemplary of linac ICS, this produces high quality output spectra, small bandwidth ( $\leq 1\%$ ), high flux ( $3 \times 10^{13}$  ph/s), but the photons are produced in a very short duration (100's fs), almost like a discrete source. This form of source is therefore well suited to pump-probe experiments. However, in order to achieve this a high powered laser was required.

An example of the commercialisation of inverse Compton scattering sources is the Lyncean Technologies CLS. This is a storage ring designed and now operated as a compact monochromatic source of X-rays. This source uses a 45 MeV electron beam to provide 8-40 keV X-rays at a flux of  $3 \times 10^{11}$  ph/s with a bandwidth between 3-9% [60]. This source has been used for Computed Tomography (CT) measurements in a comparison of the Lyncean CLS and traditional rotating anode sources [86].

Details such as the bunch charge, emittance and parameters of the laser are omitted from the information provided on the Lyncean CLS [60] as this is a commercial source protected by intellectual property. However, in order to achieve the 40 keV peak energy a laser wavelength  $\lambda \approx 800$  nm is required therefore some form of Ti:Sa laser can be assumed. A diagram of the Lyncean Technologies CLS is shown in Figure 44.

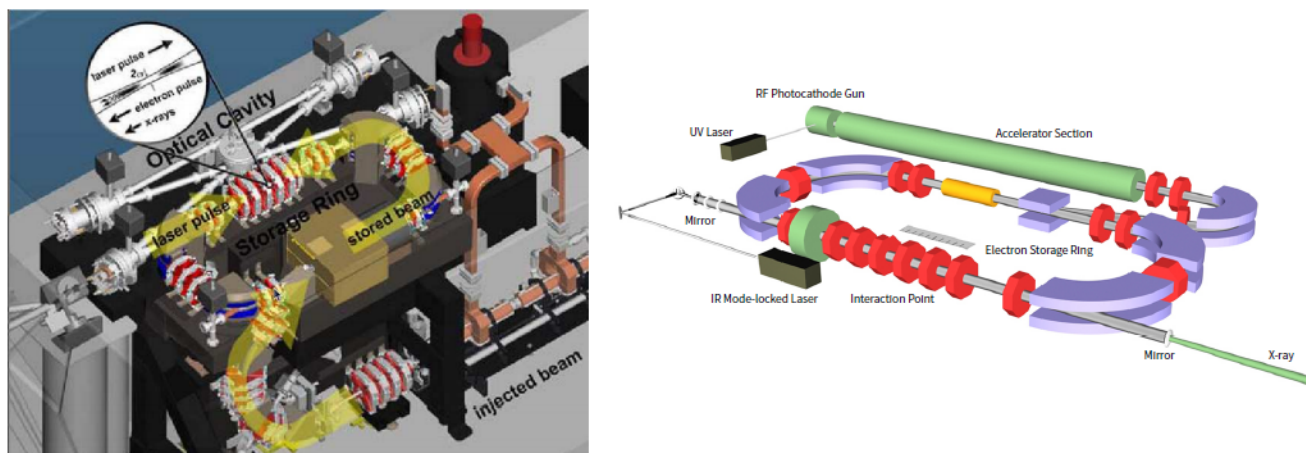


Figure 44: Left: A schematic of the interaction point of the Lyncean CLS [72]. Here a bow-tie style optical recirculation cavity can be seen creating an interaction point with the electron beam in a racetrack storage ring. Right: A diagram of the full Lyncean CLS [60]. This shows a racetrack storage ring into which the beam is injected by a linac section. As is seen from the left schematic this is actually positioned under the storage ring in order to create a compact light source.

The final ICS here is the cERL ICS which is constructed upon the cERL energy recovery linac at KEK, Japan. This source has already been covered in considerable detail in Sections 7.4 and 4, therefore is not shown in detail here. This source produces 6.95 keV soft X-rays at a flux of  $2.6 \times 10^6$  ph/s [6]. The laser and beam are recirculated to give an inverse Compton scattering interaction repetition rate of 162.5 MHz. However, the flux is severely limited by the 0.355 pC bunch charge from this demonstration.

One of the main differences distinguishable in Table 20 is that the conventional linac and ERL sources provide very narrow-band sources of X-rays, with the MIT ICS as the exception. This is as linac based ICS have an emittance governed only by the injector whereas in storage rings, since the beam is recirculated many times (typically  $> 10^5$ ) the beam equilibrates. Consequently, the emittance in the cERL ICS is 0.32 mm-mrad compared to 4.4 mm-mrad in the ThomX storage ring [84]. It follows that the emittance term of the bandwidth (34) is much larger and therefore the bandwidth is emittance dominated and much larger, from  $\frac{\Delta E_x}{E_x} < 1\%$  to  $\frac{\Delta E_x}{E_x} < 10\%$ .

However, conventional linac based ICS also has the disadvantage of a low repetition rate, generally in the 1 kHz to 10 Hz range. This means the source is reliant upon high bunch charge and laser pulse energy in order to get a high flux. This involves designing a much more complicated and expensive high power laser system in order to achieve a similar flux to recirculated sources. For example, in Table 20 ThomX and SPARC lab have similar flux however, the laser pulse energy of ThomX is 28 mJ [84] in comparison to the 5 J laser pulse energy at SPARC Lab [85].

An ERL has the potential to avoid both of these problems. It is capable of providing a beam quality consistent with that of a conventional linac whilst also enabling recirculation. Therefore, an ERL could provide a high-flux

narrow-band X-ray source. However, the two demonstrated ERL ICS are both clearly early demonstrations of this.

## 9.2 $\gamma$ -ray Inverse Compton Scattering Sources

This section explores  $\gamma$ -ray inverse Compton scattering sources, these have only been built upon conventional linacs and storage rings to this date. An ERL with a  $\gamma$ -ray producing inverse Compton source has not yet been demonstrated or proposed in detail. The two case studies explored in greater detail here are the ELI-NP conventional linac ICS [7], and the NewSUBARU storage ring [87]. The output spectral parameters for these two sources plus a range of other  $\gamma$ -ray ICS projects are shown in Table 21.

<i>ELI-NP Linac ICS Spectral Parameters</i>			
Parameter	ELI-NP (2011) [7]	ELI-NP (2014) [78]	ELI-NP (2018) [88]
$\gamma$ -ray Energy (MeV)	1-13	0.2-19.5	0.2-19.5
Spectral Energy Density (ph/seV)	$10^6$	$0.8 - 4.0 \times 10^4$	$> 0.5 \times 10^4$
Bandwidth	$\approx 0.1\%$	$\leq 0.5\%$	$\leq 0.5\%$
Photons/pulse (ph)	$8 \times 10^8$	$8.3 \times 10^6$	$1.5 \times 10^6$
Photons/sec (ph/s)	$8 \times 10^{10}$	$8.3 \times 10^8$	$1.5 \times 10^8$
Peak Brilliance (ph/s mm <sup>2</sup> -mrad <sup>2</sup> 0.1% bw)	$> 1.5 \times 10^{21}$	$10^{20} - 10^{23}$	$> 10^{19}$
<i>Other Linac ICS Spectral Parameters</i>			
Parameter	FAST (2017) [89]	FAST (2017) [90]	MEGa-ray (2011) [7]
$\gamma$ -ray Energy (MeV)	$< 1.5$	$< 1.2$	0.5-2.3
Spectral Energy Density (ph/seV)	$2.65 \times 10^4$	$2 \times 10^5$	$10^6$
Bandwidth	0.71%	0.8%	0.1%
Photons/pulse (ph)	$2.05 \times 10^7$	$1.9 \times 10^7$	$8.0 \times 10^7$
Photons/sec (ph/s)	$3.08 \times 10^9$	$2.85 \times 10^9$	$9.6 \times 10^9$
Peak Brilliance (ph/s mm <sup>2</sup> -mrad <sup>2</sup> 0.1% bw)	$1.53 \times 10^{22}$	$1.5 \times 10^{23}$	$1.5 \times 10^{20}$
<i>Storage Ring ICS Spectral Parameters</i>			
Parameter	NewSUBARU (2009) [87] [91]	HiGS (2013) [92]	HiGS (2009) [93]
$\gamma$ -ray Energy (MeV)	0.5-73	1-100	1-100
Spectral Energy Density (ph/seV)	$< 9.72$	$> 1 \times 10^3$	-
Bandwidth	1.2-1.6%	-	0.8 - 10%
Photons/pulse (ph)	-	-	-
Photons/sec (ph/s)	$3 \times 10^5 - 5.8 \times 10^6$	$\times 10^7 - 2 \times 10^{10}$	$10^6 - 3 \times 10^9$
Peak Brilliance (ph/s mm <sup>2</sup> -mrad <sup>2</sup> 0.1% bw)	-	-	-
<i>ERL ICS Spectral Parameters</i>			
Parameter	ELI-NP ERL (2011) [7]	DIANA (2019)	
$\gamma$ -ray Energy (MeV)	0.2-19.5	2.05-18.3	
Spectral Energy Density (ph/seV)	$0.5 - 4 \times 10^6$	$2.62 \times 10^6 - 5.24 \times 10^7$	
Bandwidth	$\leq 0.5\%$	$\leq 0.41\%$	
Photons/pulse (ph)	$8.3 \times 10^6$	4076-5027	
Photons/sec (ph/s)	$8.3 \times 10^{10}$	$4.08 - 5.03 \times 10^{11}$	
Peak Brilliance (ph/s mm <sup>2</sup> -mrad <sup>2</sup> 0.1% bw)	$10^{25}$	$4.79 \times 10^{16} - 2.67 \times 10^{17}$	

Table 21: Output spectral parameters for a series of proposed and designed (red) inverse Compton scattering sources and operated ICS (blue). These are based upon both storage ring and conventional linac driven ICS however, some provisional parameters for ELI-NP as an ERL are also included which was proposed but never designed in detail. The year of design or operation is shown for each source. Some values are calculated parameters (green) based on the values provided in the respective papers which are shown alongside the given (black) parameters. A - is used to denote parameters with insufficient detail to be calculated.

NewSUBARU is a storage ring ICS that operates with a high average electron beam current of 500 mA with a high power CO<sub>2</sub> laser to achieve 1.7-3.9 MeV  $\gamma$ -rays with a flux of  $5.8 \times 10^6$  ph/s [87]. The NewSUBARU storage ring has subsequently been operated as a  $\gamma$ -ray ICS with a range of lasers, for example the 2nd harmonic of the Nd:YAG laser which produced 73 MeV  $\gamma$ -rays [91]. The NewSUBARU ICS is capable of performing with three nominal beam energies:  $E_e = 974, 1220$  and  $1460$  MeV, which when interacted with a range of lasers gives a large variation in the  $\gamma$ -ray energies it can produce, as seen in Table 21. However, the flux of  $\gamma$ -rays at each of these

energies is relatively constant due to the high beam current. This allows a range of experiments to be performed at NewSUBARU. Figure 45 shows a schematic of the inverse Compton scattering source on NewSUBARU.

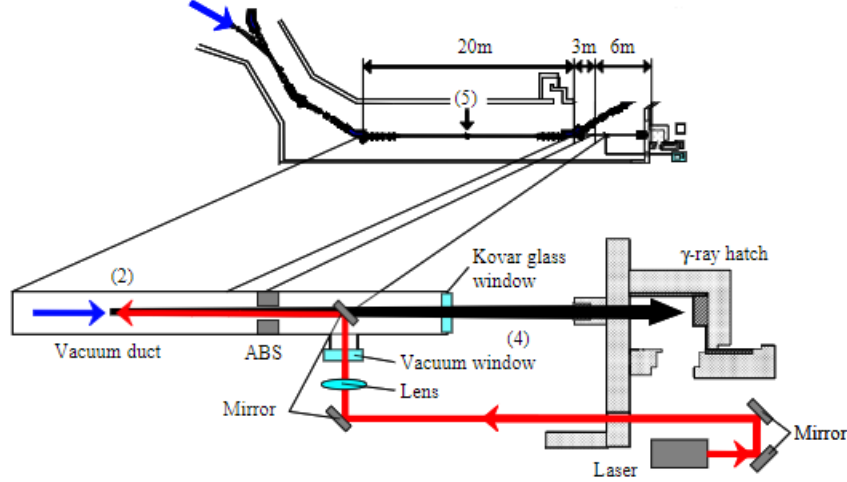


Figure 45: A schematic of the NewSUBARU inverse Compton scattering interaction point [94]. After the bunch has been extracted from the storage ring it is focused and then interacted in a head-on geometry with a laser pulse to produce backscattered  $\gamma$ -rays. This has been designed to be able to interact electron beam from 974-1460 MeV and can also utilise multiple different laser systems.

The  $\gamma$ -rays at NewSUBARU are produced in a head-on interaction as shown in Figure 27. However, this  $\gamma$ -ray ICS essentially operates like those on a linac since there is no recirculation here of the laser. In NewSUBARU the laser repetition rate still defines the repetition rate of the ICS i.e the interaction can only occur at the rate the laser pulses can be created. Therefore, the NewSUBARU experiments are flux limited by the electron beam current and laser pulse energy.

An example, already mentioned in some detail in Section 8.4, of a conventional linac ICS is the ELI-NP  $\gamma$ -ray ICS. This is designed to produce 0.2-19.5 MeV  $\gamma$ -rays at a flux of  $1.5 \times 10^8$  inside a 0.5% narrow bandwidth [88]. However, these parameters vary from author to author and have developed over time as shown in Table 21. The full parameters of the electron beam and laser system for ELI-NP are shown in Tables 18 and 17 in Section 8.4.

The ELI-NP source uses a very complicated 'dragon'-shaped laser recirculation cavity to interact with the electron bunch. This is as the electron bunch is microbunched into 32 smaller electron bunches which are all interacted individually with the laser pulse. The purpose of microbunching is to minimise the bunch length of the interacted electrons, and therefore the  $\sigma_z$  term (the convolution of bunch length and laser pulse length) which is typically dominated by the bunch length. As can be seen from (24) this increases the flux as the repetition rate can be seen to increase by a factor of 32 whilst the bunch length is decreased. The number of electrons in the macrobunch is obviously divided between the 32 microbunches here too.

The 'dragon'-shaped laser recirculation cavity is composed of two on-axis parabolic mirrors set in a confocal arrangement, 31 mirror pair systems (MPS) each mounted on a piezo-electric rotation stage, a fixed pair of injection mirrors and a fixed pair of ejection mirrors [95]. The purpose of the MPS on the piezo electric rotation stage is to be able to slightly alter the position of the mirrors and therefore the path length of the laser concurrently adapting the inverse Compton interaction time for a specific microbunch. Figure 46 shows a schematic of this 'dragon'-shape recirculation cavity with the MPS system.

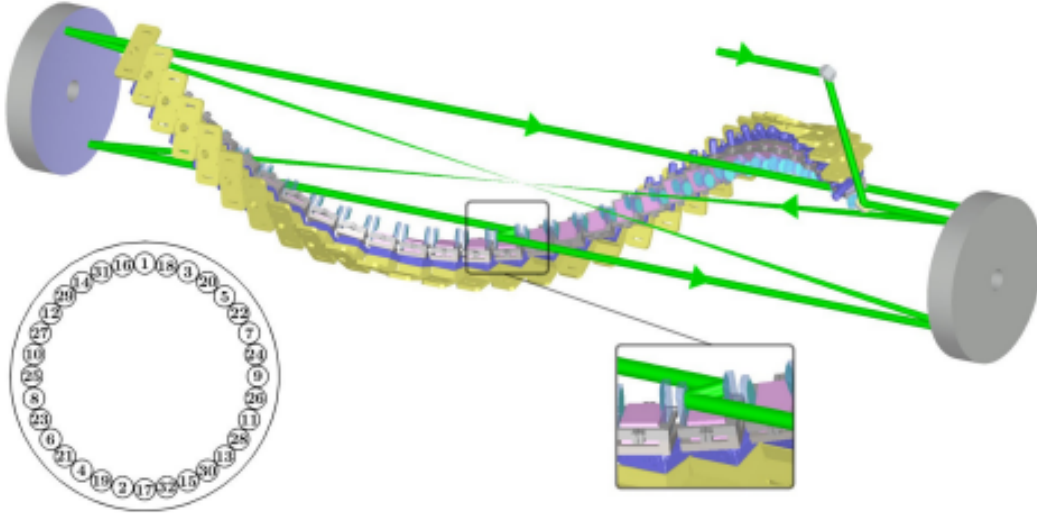


Figure 46: The ELI-NP laser recirculation system [96]. The main top plot here shows the laser recirculation system in full, this consists of the MPS mirrors arranged in a 'dragon'-shape which are bookended by the confocal mirrors. The path length and laser trajectory is adjusted by the MPS system however the microbunches are consistently interacted at the focus of the confocal mirrors. An exploded view of an MPS is shown which aims to show that these two flat mirrors are adjusted in position to create fine laser path length and positional adjustments. To the left of the main schematic the position of the MPS, which controls the fine adjustment for each microbunch (1-32), is shown on a longitudinal projection.

The laser recirculation cavity for ELI-NP is a complex optical setup. The repetition rate is also only 100 Hz for ELI-NP [97] whilst operating this cavity. This is a very low repetition rate and therefore ELI-NP is a  $\gamma$ -ray source with very high quality peak spectral output ( $8.3 \times 10^6$  ph per pulse, 0.5% bandwidth) however, the flux per second  $8.3 \times 10^8$  ph/s and the spectral energy density is modest in the context of Table 21. Therefore, the performance of ELI-NP as a continuous rather than peak source of  $\gamma$ -rays is limited by the repetition rate.

The  $\gamma$ -ray ICS sources presented in this section produce MeV level  $\gamma$ -rays which have applications for nuclear science, nuclear proliferation, medical applications and stellar astrophysics [5]. However, the  $\gamma$ -ray sources as shown in Table 21 all are of low-flux,  $F < 10^{10}$  ph/s consistently, especially in comparison to the X-ray inverse Compton scattering sources in Table 20. In the same comparison, the bandwidth for  $\gamma$ -ray sources are typically smaller i.e narrower-band across the board. Recirculating inverse Compton scattering systems could offer a potential solution to the low flux seen in  $\gamma$ -ray ICS. For example, an ERL system with a simpler laser recirculator could achieve similar or exceed the parameters of ELI-NP. The flux would be increased due to the increase in the interaction repetition rate  $f$  through a recirculating design, whilst the linac quality beam from an ERL means the source remains narrow-band. This is the motivation for the DIANA ICS design in Section 8.2. Ultimately, an ERL  $\gamma$ -ray ICS has not been demonstrated or been the subject of a comprehensive design study.

## 10 Further Work

The further work to be undertaken within this PhD project is centred around the topics of CBETA and inverse Compton scattering. This will involve a long term attachment (LTA) at Cornell University to participate in the commissioning of the 4-pass configuration of CBETA. Commissioning aims to demonstrate 4-pass energy recovery of the beam in the CBETA ERL. Work towards commissioning will involve simulations through CBETA-V, which is a custom version of Tao [63] including extra commands to allow access to the Experimental Physics and Industrial Control System (EPICS). EPICS is a control system which is commonly used for controlling particle accelerators and is used to control accelerator components such as RF cavities and magnets through a single integrated system. The CBETA Virtual Machine is another tool widely used by the CBETA collaboration. The CBETA virtual machine creates a virtual EPICS record which mimics EPICS records in the real machine (controls and diagnostics), starts an instance of CBETA-V then monitors for changes in EPICS which are then simulated in CBETA-V to simulate the new diagnostics. The virtual machine is also used for CBETA operator training, therefore knowledge of CBETA-V and the virtual machine is necessary for participation in



commissioning. Participation within the CBETA collaboration will also involve some data analysis of the results from commissioning and operation of the accelerator. Knowledge of CBETA-V and the CBETA virtual machine will be useful in data analysis as this allows simulation of expected data from the real machine.

The CBETA ICS which is outlined in Section 7.1 will continue to be designed. The laser recirculation system will be elaborated upon and improved so that it is designed as a feasible scheme. This will include further design and specification of the recirculation cavity and a reduction in the repetition rate as this is currently unfeasibly high. Further work will involve improving the bypass design presented in Section 7.5, this design is deficient in that the dispersion at the inverse Compton scattering interaction is not zero ( $\eta_x \neq 0$ ). The bypass is also not sufficiently well matched when it is merged back into the return loop at the TB section. Therefore modifications of the design such as adding an extra quadrupole, implementing a dispersion suppressor and re-optimising the bypass lattice are required. The CBETA ICS will be the subject of a conference poster presentation at ERL 19.

Another focus of future work will be a more general insight into inverse Compton scattering sources. There has been no comprehensive discussion of lasers systems or laser recirculation systems in this report. This discussion has been omitted as these are topics which, whilst are reasonably well understood, have not yet been sufficiently well researched. Further work will investigate suitable lasers for ICS and schemes of laser recirculation cavities. As well as this an investigation into ICS simulation codes such as CAIN [4], a MonteCarlo code, and ICCS, an analytical code based on scaling laws by G.A. Krafft et al [70] will be conducted. Further design work is foreseen for the DIANA ICS, which will involve refining the inverse Compton source scattering design and simulating this source. A study into ICS on storage rings will also be undertaken as low emittance storage rings, which have a high repetition rate due to frequent recirculation intrinsic to storage rings, could be beneficial in creating a high flux ICS and modified such that the beam quality is still sufficient i.e reduction of intrabeam scattering and equilibrium effects. This is inspired by the design of non-equilibrium storage rings [19] and the results of Z. Pan et al [98] for a low emittance storage ring ICS. This exploration will contribute to the discussion of the best accelerator types for recirculating ICS. Finally, an investigation furthering the work in Section 6.6 will involve looking at methods of including a full treatment of non-linear and recoil regime effects into a bandwidth calculation.

## 10.1 Gantt Chart

The Gantt chart presented here is created to outline the future work within the PhD project. This is centred around a long term attachment (LTA) of 6 months in order to participate in CBETA commissioning. This is intended to show the rough schedule of work and present some of the topics that will be focused on. The Gantt chart is shown below in Figure 47.

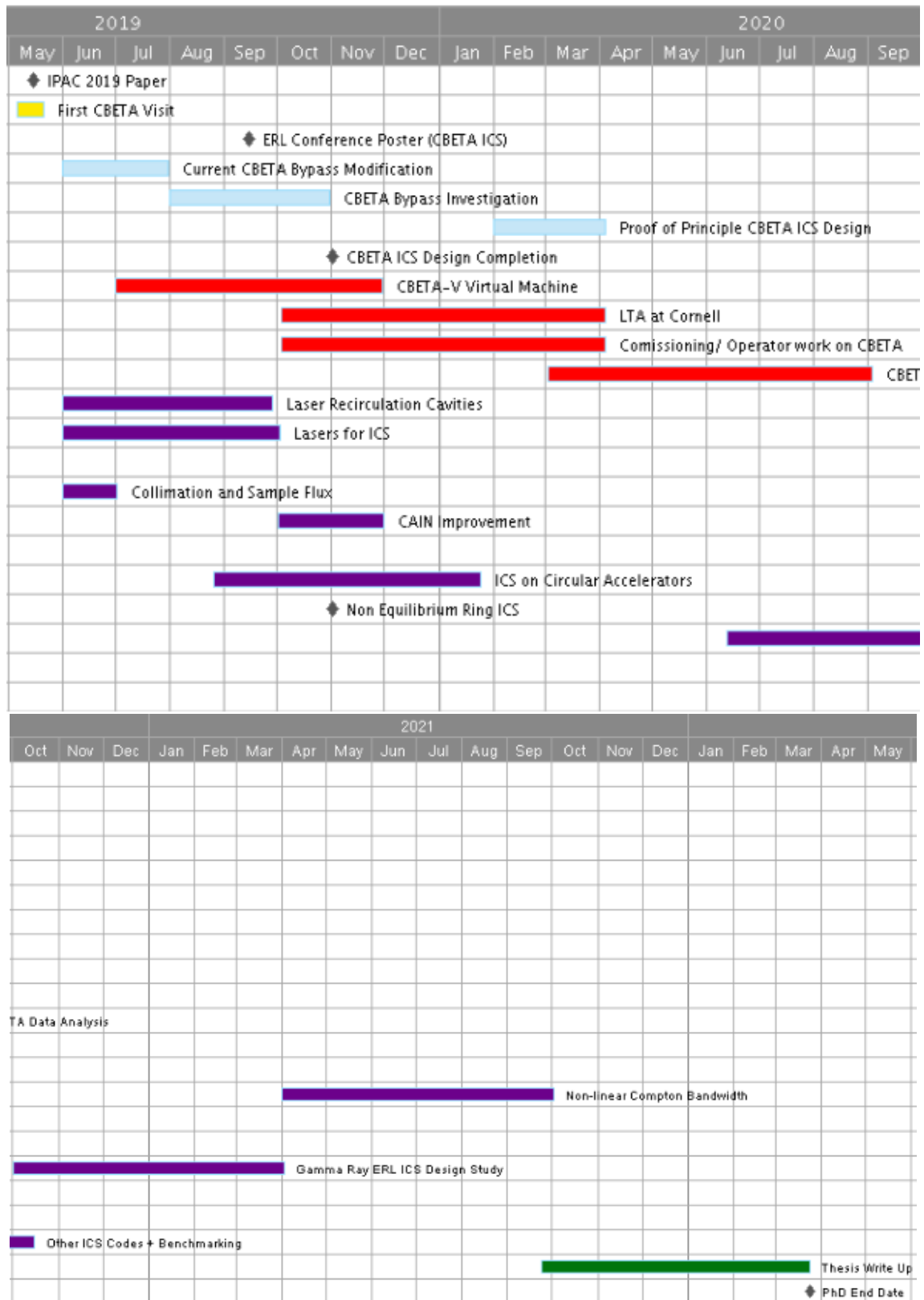


Figure 47: A brief indicative Gantt chart showing the rough time line of the PhD project. Within the work included on this chart some is fixed like the LTA and CBETA commissioning participation (red). The CBETA ICS (blue) and general ICS (purple) sections are more fluid. Planned papers and conference posters (grey diamond) are also included.

## 10.2 Thesis Chapter Titles

A short list of potential thesis chapters are shown below. These show the focus of the project work to come. Investigating inverse Compton scattering sources and the form of accelerator they are driven by has increasingly become a focus of this project. A series of provisional thesis chapter titles are shown below.

- Introduction
- Theory of Inverse Compton Scattering Photon Production
- Non-Equilibrium Ring Inverse Compton Source Design
- ERL Based inverse Compton Source Design
- Multi-pass CBETA Commissioning
- Conclusions



## References

- [1] G.H. Hoffstaetter et al. CBETA, The 4-turn ERL with SRF and Single Return Loop. *Proceedings of the 9th International Particle Accelerator Conference, Vancouver, Canada*, (2018).
- [2] D. Trbojevic et al. CBETA, Cornell University Brookhaven National Laboratory Electron Energy Recovery Test Accelerator. *Proceedings of the 8th International Particle Accelerator Conference, Copenhagen, Denmark*, (2017).
- [3] E.C. Aschenauer et al. eRHIC Design Study: An Electron-Ion Collider at BNL. *Brookhaven National Laboratory, Design Report, arXiv:1409:1633*, (2014).
- [4] P. Chen et al. Conglomerat d'ABEL et d'Interactions Non-Lineaires. *Nuclear Instruments and Methods in Physics Research A*, 355, (1994).
- [5] P. H. Williams. DIANA: Daresbury Industrial Accelerator for Nuclear Applications. *Darmstadt, Available at: <https://ikpcloud.ikp.physik.tu-darmstadt.de/index.php/s/PaKivWSt3ZyDkgq>*, (2019).
- [6] T. Akagi et al. Narrow-band Photon Beam via Laser Compton Scattering in an Eenergy Recovery Linac. *Physical Review Accelerators and Beams*, 19, 114701, (2016).
- [7] ELI-NP Collaboration. The White Book of ELI Nuclear Physics. *Bucharest-Magurele, Romania. Available at: <https://www.eli-np.ro/documents/ELI-NP-Whitebook.pdf>*, (2011).
- [8] M. Arnold et al. First ERL Operation of S-DALINAC and Commissioning of a Path Length Adjustment System. *Proceedings of the 9th International Particle Accelerator Conference, Vancouver, Canada*, (2018).
- [9] L. Merminga et al. High-Current Energy-Recovering Linacs. *Annual Review of Nuclear and Particle Science*, 53, 1, (2003).
- [10] A. Bocagz et al. CEBAF Energy Recovery Experiment. *Proceedings of the 20th Particle Accelerator Conference, Portland, Oregon*, (2003).
- [11] M. Arnold et al. Construction and Status of the Thrice Recirculating S-DALINAC. *Proceedings of the 8th International Particle Accelerator Conference, Copenhagen, Denmark*, (2017).
- [12] C.L. Bohn. Recirculating Accelerator Driver for a High-Power Free Electron Laser. *Proceedings of the 17th Particle Accelerator Conference*, (1997).
- [13] T.H. Walcher. The Mainz Microtron Facility MAMI. *Progress in Particle and Nuclear Physics*, 24, (1990).
- [14] H. Euteneuer. The 4.9GHz Accelerating Structure for MAMI C. *Proceedings of the 7th European Particle Accelerator Conference, Vienna, Austria*, (2000).
- [15] A. Jankowiak. Energy Recovery Linacs. *Cern Accelerator School, Egham, UK. Available at: <https://cas.web.cern.ch/sites/cas.web.cern.ch/files/lectures/egham-2017/2017-09-07-cas17-erl-andreasjankowiak.pdf>*, (2017).
- [16] G. H. Hoffstaetter and I. Bazarov. Beam-Breakup Instability Theory for Energy Recovery Linacs. *Physical Review Special Topics - Accelerators and Beams*, 7, 054401, (2004).
- [17] G.H. Hoffstaetter et al. Cbeta Design Report. *Technical Report, CBETA-015, CLASSE and BNL*, (2017).
- [18] W. P. Swanson. Improved Calculation of Photoneutron Yields Released by Incident Electrons. *Health Physics*, 37, 3, (1979).
- [19] H.L. Owen et al. Non-Equilibrium Electron Rings for Synchrotron Radiation Production. *Physical Review Letters*, 110, 179903, (2013).
- [20] K. R. Symon. The FFAG Synchrotron - Mark I. *Midwestern Universities Research Association, Technical Note, MURA-KRS-6*, (1954).
- [21] J. Rossbach. Basic Course on Accelerator Optics. *CERN Accelerator School, Jyväskylä, Finland*, (1992).
- [22] J.B. Adams. The CERN Proton Synchrotron. *Nature*, 185, (1960).
- [23] E.D. Courant and H.S. Snyder. Theory of the Alternating-Gradient Synchrotron. *Annals of Physics*, 3, 1, (1958).
- [24] S. Machida. Fixed-Field Alternating Gradient. *Pre-Print, arXiv: 1302.2026*, (2013).
- [25] K.R. Symon et al. Fixed-Field Alternating Gradient Particle Accelerators. *Physical Review*, 103, 6, (1956).
- [26] S.L. Sheehy. Fixed-Field Alternating Gradient Accelerators. *CERN Specialised Accelerator School on Medical Accelerators, arXiv: 1604:05221*, (2015).
- [27] M.K. Craddock. FFAG Optics. *International Workshop on FFAG Accelerators, Daresbury, UK*, (2011).

- [28] J. Scott Berg. The EMMA Main Ring Lattice. *Nuclear Instruments and Methods in Physics Research A*, 596, (2008).
- [29] M. Aiba. Development of a FFAG Proton Synchrotron. *Proceedings of the 3rd European Particle Accelerator Conference, Vienna, Austria*, (2000).
- [30] S. Smith. EMMA, The World's First Non-Scaling FFAG Accelerator. *Proceedings of the 23rd Particle Accelerator Conference, Vancouver, Canada*, (2009).
- [31] S. Machida et al. Acceleration in the Linear Non-Scaling Fixed-Field Alternating-Gradient Accelerator EMMA. *Nature Physics*, 8, (2012).
- [32] S. Machida and R. Fenning. Beam Transport Line with Scaling Fixed Field Alternating Gradient Type Magnets. *Physical Review Special Topics - Accelerators and Beams*, 13, 084001, (2010).
- [33] D. Trbojevic et al. Large Momentum Acceptance Superconducting ns-FFAG Gantry for Carbon Cancer Therapy. *Proceedings of the 27th Particle Accelerator Conference, Pasadena CA, USA*, (2013).
- [34] M. Tigner. A Possible Apparatus for Electron Clashing-Beam Experiments. *Il Nuovo Cimento*, 37, 3, (1965).
- [35] T. I. Smith et al. Development of the SCA/FEL for use in Biomedical and Materials Science Experiments. *Nuclear Instruments and Methods in Physics Research A*, 259, (1987).
- [36] N. A. Vinokurov et al. Novosibirsk Four-Orbit ERL with Three FELs. *Proceedings of the 8th International Particle Accelerator Conference, Copenhagen, Denmark*, (2017).
- [37] N. A. Vinokurov et al. Novosibirsk Free Electron Laser Facility: Two-Orbit ERL with Two FELs. *Proceedings of the 31st Free Electron Laser Conference, Liverpool, UK*, (2009).
- [38] O. A. Shevchenko et al. The Novosibirsk Free-Electron Laser - Unique Source of Terahertz and Infrared Coherent Radiation. *Physics Procedia*, 84, (2016).
- [39] O. A. Shevchenko et al. The Novosibirsk Free Electron Laser Facility. *Bulletin of the Russian Academy of Sciences: Physics*, 83, 2, (2019).
- [40] N. A. Vinokurov et al. Novosibirsk ERL Facility. *Proceedings of the 59th Energy Recovery Linac Conference, Geneva, Switzerland*, (2017).
- [41] V. N. Volkov et al. New RF Gun for Novosibirsk ERL FEL. *Physics Procedia*, 84, (2016).
- [42] R. Legg. Operating Experience at CEBAF. *Technical Note, CEBAF-PR-96-013, Southeastern Universities Research Association, Newport News, Virginia*, (1996).
- [43] H. A. Grunder. CEBAF Commissioning and Future Plans. *Proceedings of the 16th Particle Accelerator Conference, Dallas, Texas*, (1995).
- [44] Y. Chao et al. CEBAF Accelerator Achievements. *Journal of Physics: Conference Series*, 299, 1, (2011).
- [45] C. Leemann et al. The Continuous Electron Beam Accelerator Facility: CEBAF at the Jefferson Laboratory. *Annual Review of Nuclear and Particle Science*, 51, 1, (2001).
- [46] F. Meot et al. ER@CEBAF - A High Energy, Multiple Pass Energy Recovery Experiment at CEBAF. *Proceedings of the 7th International Particle Accelerator Conference, Busan, Korea*, (2016).
- [47] Y. Nosochkov et al. Update on the JLEIC Electron Collider Ring Design. *Proceedings of the 8th International Particle Accelerator Conference, Copenhagen, Denmark*, (2017).
- [48] G. I. Budker et al. Experimental Studies of Electron Cooling. *Particle Accelerators*, 7, (1976).
- [49] M. Bai. Introduction to Electron Cooling. *BND School, FZ Juelich*, Available at: <https://indico.cern.ch/event/357886/contributions/849347/attachments/1148562/1647628/EC.pdf>, (2015).
- [50] M. Steck et al. Electron Cooling Experiments at the ESR. *Nuclear Instruments and Methods in Physics Research A*, 532, (2004).
- [51] H. Poth. Electron Cooling: Theory, Experiment, Application. *Physics Reports*, 196, (1990).
- [52] M. Arnold et al. Construction and Status of the Thrice recirculating S-DALINAC. *The 8th International Particle Accelerator Conference, Copenhagen, Denmark*, (2017).
- [53] M. Arnold et al. First ERL Operation of S-DALINAC and Commissioning of a Path Length Adjustment System. *Proceedings of the 9th International Particle Accelerator Conference, Vancouver, Canada*, (2018).
- [54] M. Arnold et al. ERL Mode of S-DALINAC: Design and Status. *Proceedings of the 59th Energy Recovery Linac Conference, Geneva, Switzerland*, (2017).
- [55] H.L. Owen and P. H. Williams. A Modular Path Length Corrector for Energy Recovery Linacs. *Nuclear Instruments and Methods in Physics Research A*, 662, (2012).

- [56] Y. M. Saveliev. ALICE: Status, Developments and Scientific Program. *Proceedings of the 3rd International Particle Accelerator Conference, New Orleans, USA*, (2012).
- [57] M. W. Poole and E. A. Seddon. 4GLS and the Prototype Energy Recovery Linac Project at Daresbury. *Proceedings of the 9th European Particle Accelerator Conference, Lucerne, Switzerland*, (2008).
- [58] G. Priebe et al. First Results of the Daresbury Compton Backscattering X-ray Source (COBALD). *Hard X-ray, Gamma-ray, and Neutron Detector Physics XII, 7805, International Society for Photonics and Optics*, (2010).
- [59] D. Laundry et al. Results from the Daresbury Compton Backscattering X-ray Source. *Nuclear Instruments and Methods in Physics Research A*, 689, (2012).
- [60] K. Achterhold et al. The Lyncean Technologies Compact Light Source. *Lyncean Technologies, White Paper, Available at: [https://www.lynceantech.com/cls\\_whitepaper\\_1/](https://www.lynceantech.com/cls_whitepaper_1/)*, (2018).
- [61] K. Deitrick et al. A Hard X-ray Compact Compton Source at CBETA. *Proceedings of the 10th International Particle Accelerator Conference*, (2019).
- [62] D. Sagan. The Bmad Manual. *Available at: <https://www.classe.cornell.edu/bmad/manual.html>*, (2019).
- [63] D. Sagan. The Tao Manual. *Available at: <https://www.classe.cornell.edu/bmad/tao.html>*, (2019).
- [64] J.S. Berg. Summary of April 10, 2017 Lattice. *Technical Report, CBETA-014, CLASSE and BNL*, (2017).
- [65] D. Trbojevic et al. Hallbach Magnets for CBETA. *CBETA Technical Note 008, Cornell University and BNL, Available at: [https://www.classe.cornell.edu/CBETA\\_PM/notes/CBETA008.pdf](https://www.classe.cornell.edu/CBETA_PM/notes/CBETA008.pdf)*, (2017).
- [66] M. Vretenar. Linear Accelerators. *Proceedings of the CAS-CERN Accelerator School: Advanced Accelerator Physics, Trondheim, Norway*, (2014).
- [67] C. Gulliford et al. CBETA Beam Commissioning Results. *The 10th International Particle Accelerator Conference, Melbourne, Australia*, (2019).
- [68] G. A. Krafft et al. Laser Pulsing in Linear Compton Scattering. *Physical Review Accelerators and Beams*, 19, 121302, (2016).
- [69] L. Serafini et al. Analytical Description of Photon Beam Phase Spaces in Inverse Compton Scattering Sources. *Physical Review Accelerators and Beams*, 20, 080701, (2017).
- [70] G. A. Krafft et al. Combining Harmonic Generation and Laser Chirping to Achieve High Spectral Density in Compton Sources. *Physical Review Accelerators and Beams*, 19, 044403, (2016).
- [71] V. Petrillo et al. Compensation of Non-Linear Bandwidth Broadening by Laser Chirping in Thomson Sources. *Journal of Applied Physics*, 124, 063105, (2018).
- [72] G. A. Krafft and G. Priebe. Compton Sources of Electromagnetic Radiation. *Reviews of Accelerator Science and Technology*, 1, (2008).
- [73] G. A. Krafft et al. Simulation of Inverse Compton Scattering and its Implications on the Scattered Linewidth. *Physical Review Accelerators and Beams*, 21, 030701, (2018).
- [74] L. Serafini et al. Photon Flux and Spectrum of  $\gamma$ -rays Compton Sources. *Nuclear Instruments and Methods in Physics Research A*, 693, (2012).
- [75] F. Zomer. Description of the New ATF Four-Mirror Cavity. *KEK Physics Seminar, Available at: [https://www2.kek.jp/physics-seminar/files2010/20100816\\_zomer.pdf](https://www2.kek.jp/physics-seminar/files2010/20100816_zomer.pdf)*, (2010).
- [76] K. Yokoya et al. Users Manual of CAIN. *Available at: <https://ilc.kek.jp/yokoya/CAIN/cain235/CainMan235.pdf>*, (2003).
- [77] A. M. Kellerer. Electron Spectra and the RBE of X-rays. *Radiation Research*, 1, 158, (2002).
- [78] L. Serafini et al. Technical Design Report: EuroGammaS Proposal for the ELI-NP Gamma Beam System. *Technical Design Report, ELI-NP-GBS, Magurele-Bucharest, Romania, arXiv: 1407:3669*, (2014).
- [79] U. Kneissl et al. Investigation of Nuclear Structure by Resonance Fluorescence Scattering. *Progress in Particle and Nuclear Physics*, 37, (1996).
- [80] R. Hajima et al. Design of a Multi Turn ERL for Hybrid K-Edge Densitometer. *Proceedings of the 32nd Free Electron Laser Conference, Malmo, Sweden*, (2010).
- [81] A. Bacci et al. Status of the Thomson Source at SPARC/PLASMONX. *Nuclear Instruments and Methods in Physics Research A*, 608, (2009).
- [82] C. Vaccarezza et al. The SPARC Lab Thomson Source. *Nuclear Instruments and Methods in Physics Research A*, 829, (2016).

- [83] W. S. Graves et al. MIT Inverse Compton Source Concept. *Nuclear Instruments and Methods in Physics Research A*, 608, (2009).
- [84] A. Variola et al. ThomX Technical Design Report. *Saclay, France, Available at: [http://hal.in2p3.fr/file/index/docid/971281/filename/TDR\\_ThomX.pdf](http://hal.in2p3.fr/file/index/docid/971281/filename/TDR_ThomX.pdf)*, (2014).
- [85] C. Vaccarezza et al. The SPARC Lab Thomson Source Commissioning. *Proceedings of the 5th International Particle Accelerator Conference, Dresden, Germany*, (2014).
- [86] K. Achterhold et al. Monochromatic Computed Tomography with a Compact Laser-Driven X-ray Source. *Nature Scientific Reports*, 3, 1313, (2013).
- [87] S. Amano et al. Several MeV  $\gamma$ -ray Generation at NewSUBARU by Laser Compton Backscattering. *Nuclear Instruments and Methods in Physics Research A*, 602, (2009).
- [88] S. Gales et al. The Extreme Light Infrastructure-Nuclear Physics (ELI-NP) Facility: New Horizons in Physics with 10 PW Ultra-Intense Lasers and 20 MeV Brilliant Gamma Beams. *Reports on Progress in Physics*, 81, 094301, (2018).
- [89] D. Mihalcea et al. High Brightness Gamma-ray Production at Fermilab Accelerator Science and Technology (FAST) Facility. *AIP Conference Proceedings*, 1812, 100002, (2017).
- [90] D. Mihalcea et al. High Spectral Density Compton Back-Scattered Gamma-ray Sources at Fermilab. *Proceedings of the 38th Free Electron Laser Conference, Santa Fe, New Mexico*, (2017).
- [91] H. Utsunomiya. The  $\gamma$ -ray Beam-Line at NewSUBARU. *Nuclear Physics News*, 25, 3, (2015).
- [92] Y. K. Wu. Overview of High Intensity Gamma-ray Source Capabilities and Future Upgrades. *International Workshop on Polarized Sources, Targets and Polarimetry, University of Virginia. Available at: [http://faculty.virginia.edu/PSTP2013/Talks/HIGSCapabilities\\_PSTP2013\\_v2.pdf](http://faculty.virginia.edu/PSTP2013/Talks/HIGSCapabilities_PSTP2013_v2.pdf)*, (2013).
- [93] H. R. Weller et al. Research Opportunities at the Upgraded HI $\gamma$ S Facility. *Progress in Particle and Nuclear Physics*, 62, (2009).
- [94] K. Horikawa et al. Measurements for the Energy and Flux of Laser Compton Scattering  $\gamma$ -ray Photons Generated in an Electron Storage Ring. *Nuclear Instruments and Methods in Physics Research A*, 618, (2010).
- [95] C.F. Ndiaye et al. Low Power Source Commissioning of an Innovative Laser Beam Circulator for Inverse Compton Scattering  $\gamma$ -ray Source. *Pre-Print arXiv: 1901.05521v1*, (2019).
- [96] I. Drebot et al. Expected Gamma Spectra at ELI-NP-GBS. *Proceedings of the 7th International Particle Accelerator Conference, Busan, Korea*, (2016).
- [97] C. A. Ur et al. The ELI-NP Facility for Nuclear Physics. *Nuclear Instruments and Methods in Physics Research B*, 355, (2015).
- [98] Z. Pan et al. Design and Dynamic Studies for a Compact Storage Ring to Generate Gamma-ray Light Source Based on Compton Backscattering Technique. *Physical Review Accelerators and Beams*, 22, 040702.